2007-07-20

Development of a Multiple Microphone Probe Calibrator

Jonathan Reed Oldham
Brigham Young University - Provo

BYU ScholarsArchive Citation

Oldham, Jonathan Reed, "Development of a Multiple Microphone Probe Calibrator" (2007). *All Theses and Dissertations*. 1151.
https://scholarsarchive.byu.edu/etd/1151

DEVELOPMENT OF A MULTIPLE MICROPHONE PROBE CALIBRATOR

by

Jonathan Reed Oldham

A thesis submitted to the faculty of

Brigham Young University

Master of Science

Department of Mechanical Engineering

Brigham Young University

August 2007

BRIGHAM YOUNG UNIVERSITY

GRADUATE COMMITTEE APPROVAL

of a thesis submitted by

Jonathan Reed Oldham

This thesis has been read by each member of the following graduate committee and by majority vote has been found to be satisfactory.

Date	Jonathan D. Blotter, Chair
Date	Scott D. Sommerfeldt
Date	Scott L. Thomson
Date	Kent L. Gee

BRIGHAM YOUNG UNIVERSITY

As chair of the candidates graduate committee, I have read the thesis of Jonathan Reed Oldham in its final form and have found that (1) its format, citations, and bibliographical style are consistent and acceptable and fulfill university and department style requirements; (2) its illustrative materials including figures, tables, and charts are in place; and (3) the final manuscript is satisfactory to the graduate committee and is ready for submission to the university library.

Date	Jonathan D. Blotter Chair, Graduate Committee

Accepted for the Department

Matthew R. Jones
Graduate Coordinator

Accepted for the College

Alan R. Parkinson
Dean, Ira A. Fulton College of
Engineering and Technology

ABSTRACT

DEVELOPMENT OF MULTIPLE MICROPHONE PROBE CALIBRATOR

Jonathan R. Oldham

Department of Mechanical Engineering

Master of Science

This paper presents the theory, design, and validation of a microphone calibrator used to calibrate multiple microphones simultaneously. This work was done in conjunction with the development of an acoustic energy density probe, which was used to validate the calibrator. The probe uses multiple microphones to acquire the data needed to compute the acoustic energy density. The probe microphones are 0.006 m diameter electret microphones which typically do not have an ideal "flat" response over a wide range of frequencies as compared to precision condenser microphones. The probe microphone characteristics prompted the need for simultaneous, multi-microphone magnitude calibration. The idea behind the calibration process was to simultaneously subject each microphone on the probe to the same known acoustic pressure over the frequency range of the probe (0–2 kHz). This is done using equal-length small-diameter tubes connected

to a single source at each microphone. The calibrator was modeled using and equivalent circuit model. The model results are presented and compared to measured results. The calibrator was validated to result in the same pressure along individual paths to each microphone simultaneously. Test results show that the calibrator can calibrate each probe microphone within ± 0.5 dB up to 2000 Hz, and within ± 1 dB up to 4900 Hz with a confidence level of 95%. Directivity tests were performed to further characterized. Using a correction factor the probe is shown to be directionally independent.

ACKNOWLEDGMENTS

I would first like to thank my advising professor and thesis committee chair, Dr. Jonathan Blotter. The ultimate project outcome was a direct result of his foresight and vision. I would also like to thank my other thesis committee members, Dr. Scott Sommerfeldt, Dr. Scott Thomson, and Dr. Kent Gee, whose insight, counsel, and understanding aided through several difficult concepts, and over numerous research hurdles. I would further like to acknowledge the assistance of Dr. Tim Leishman as an invaluable contribution to my thesis.

In addition, I acknowledge help from my lab mates, both past and present, for the hours of help with an idea or concept. I would be derelict if I did not thank the sponsor of my research, NASA, for their support. I wish to thank the BYU acoustics research group and all of those who helped me with the research related to this thesis work.

I acknowledge the support of all my family and friends. I specifically avow the influence of my parents by instilling in me a desire to pursue academic achievement at a very early age.

My gratitude would be deficient with out explicit expression of thanks to my wife Annie. She made great sacrifices in supporting me. Her positive encouragement never paused. Finally, with reverence, I recognize the quiet moments of inspiration that led to this achievement by focusing my thanks toward heaven.

TABLE OF CONTENTS

LIST OF TABLES

LIST OF FIGURES

1 INTRODUCTION

The focus of this research was to design, build, and validate a multiple microphone calibrator. Multiple microphone probes are used to calculate acoustic intensity and energy density. This chapter introduces and provides a brief overview of the project. This chapter also outlines the remaining chapters.

1.1 OVERVIEW

The objective of this research was to simultaneously calibrate the magnitude of each microphone on a probe within ± 0.5 dB re 20 μPa over the operational frequencies of the probe (0–2000 Hz). Intensity and energy density are calculated using pressure and velocity. The intensity calculation is similar to the energy density calculation. A published calibration standard for intensity probes exists. A class 1 intensity probe must be calibrated within ± 0.7 dB, and a class 2 intensity probe must be calibrated within ±1 dB[1]. Some applications require slightly smaller tolerances. For example, Liu showed that the error needed to be within ± 0.5 dB to adequately measure absorption coefficients[2]. No such published standard exists for an acoustic energy density sensor. Given the calculation similarities between energy density and intensity, the calibration standards for an intensity probe will be applied to the energy density probe for this research.

Pressure measurements made by microphones are the most common sound field measurement. Pressure measurements can be used to calculate many other acoustic properties. Individual precision condenser microphones are calibrated prior to use to ensure accurate measurements. Several multi-microphone probes exist and can be used to measure pressure and calculate other desired acoustic quantities[3]. Such quantities include acoustic intensity, acoustic energy density, and particle velocity. In this work "particle" refers to a group of air molecules moving in the same direction at the same speed and not the individual molecules of the medium. The particle velocity is produced by the sound not Brownian motion[4].

The calibrator was designed using waveguides with circular cross-sections. A concept was conceived that would propagate the pressure from a source and channel it along identical acoustic paths to different destinations, resulting in the same pressure at each sensor. In this concept the microphones are placed at the end of the different paths. If the pressure is propagated equally along each path, the pressure will be equal at the end of each path. A photograph of the probe in the calibrator is shown in Figure 1–1.

The calibrator is discussed in this paragraph as it appears from left to right in Figure 1–1. The driver is connected to the driver tube by the coupler and excites the calibrator. The driver tube guides the sound to the splitter. The splitter divides the volume velocity of the sound into five equal paths, and the receiver tubes channel the sound to the inserts. The inserts channel the sound to the microphones. The calibrator clamp surrounds the probe, and aligns the inserts to the probe microphones. The bolts constrain the inserts in the calibrator clamp. Three latches are used to hold the calibrator clamp together. The calibrator and each of the components are described in detail in Chapter 5.

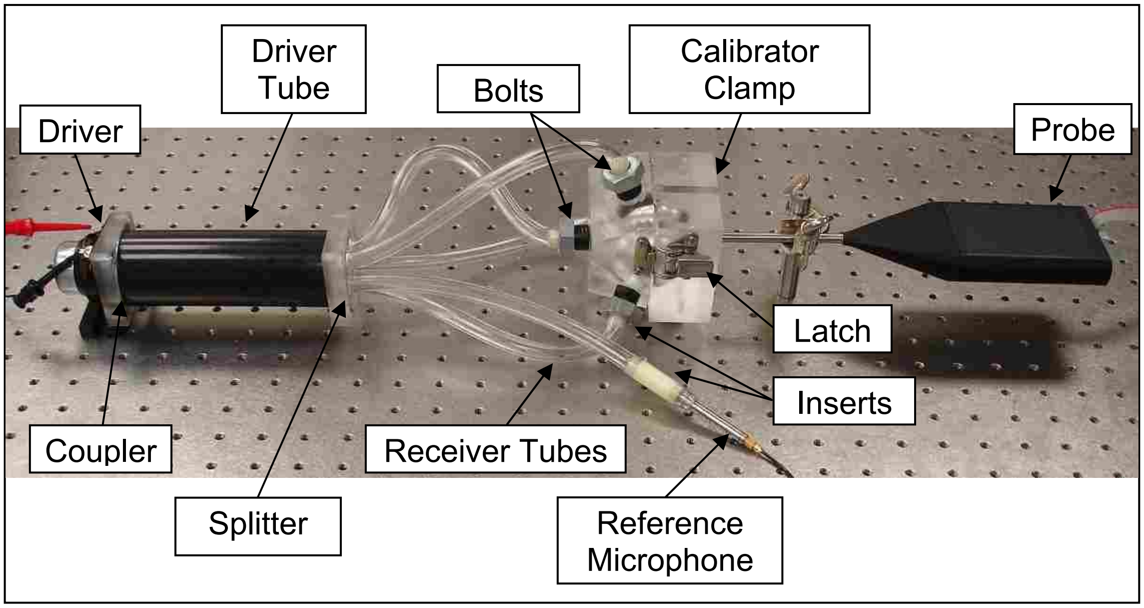

Figure 1–1: Entire calibrator

The calibrator was thought of as having three main stages. The first stage was the splitter stage. In this stage the sound field volume velocity is divided equally into the different paths. The second stage was the receiver tubes stage. In this stage each path must propagate the pressure identically. The third stage was the full calibrator stage. In this stage the sound field volume velocity that was divided equally and channeled identically must be the same as measured by each microphone on the probe and the reference microphone. Experiments were performed at the three different stages to validate the calibrator. All three stages were validated at discrete frequencies, and the final stage was further validated over a continuous range of frequencies.

The calibrator was developed in connection with a multi-microphone probe shown in Figure 1–2 and described further in Section 2.3.3. The probe is intended to calculate acoustic energy density up to 2000 Hz. This limit is discussed further in Chapter

2. The probe is equipped with four microphones that are mounted in a solid aluminum sphere. The sphere is separated from the digital signal processing (DSP) housing by the probe shaft. The axis that runs through the center of the shaft and down the length of the probe is defined as the z-axis.

To further develop the probe, directivity tests were conducted to ensure that it was directionally independent. The directional characteristics of the probe and the methods used to test the directional independence of the probe are further discussed in Chapter 7.

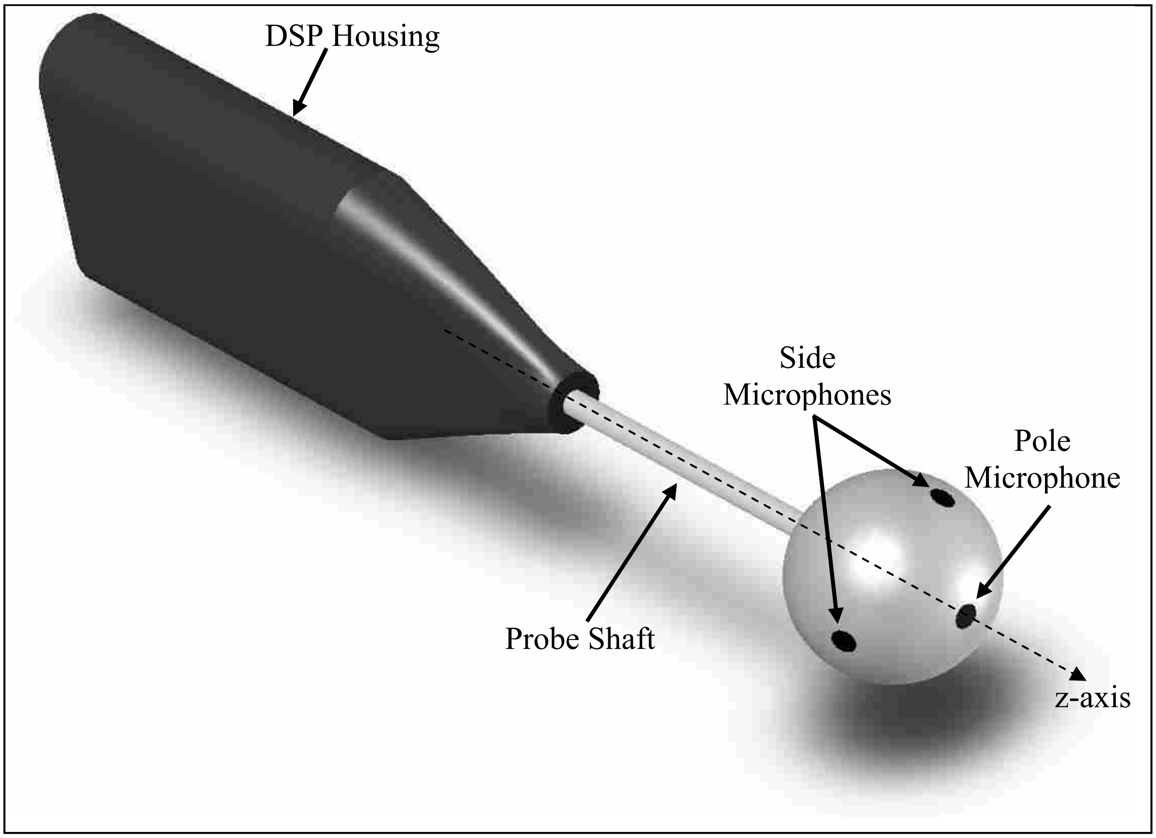

Figure 1–2: Acoustic energy density probe

1.2 THESIS OUTLINE

The remainder of this thesis describes the development of the calibrator in detail along with the validations performed. Chapter 2 presents the concept of calibration, other necessary background information, and a literature review. The methods of calibration relevant to this work are outlined and presented in detail. The method used to calculate acoustic energy density is shown. Two types of multiple transducer probes are discussed. The probe used to validate the calibrator is described. Several methods used to calibrate other multiple acoustic sensor probes are discussed. Chapter 3 presents the theory behind the calibrator design, and an in depth look at waves in waveguides. Chapter 4 discusses an equivalent circuit modeling technique useful in modeling waveguides. The calibrator is modeled using this technique and the model results are presented. Chapter 5 discusses the calibrator hardware. Detailed drawings are used to describe each component and the interactions between the different components. Chapter 6 presents the methods used to validate the calibrator along with the results obtained from the validations. Chapter 7 discusses the directional characteristics of the probe used to validate the calibrator. The probe is tested to determine the probe's performance based on orientation. The results of these tests are presented and discussed. Conclusions made based on the work of this thesis are presented in Chapter 8 along with recommendations for future work. Chapter 9 provides a list of references. The Appendices provide vital information needed to reproduce the measured and modeled results presented in this thesis.

2 BACKGROUND AND LITERATURE REVIEW

This chapter discusses the background of calibration, and the different calibration techniques that are relevant to this work. This chapter also discusses calibration techniques for several types of probes that measure pressure to calculate velocity and other acoustic quantities. These types of probes will be referred to as pressure probes. This chapter also discusses a sensor that measures pressure and velocity to calculate other acoustic quantities. These types will be referred to as pressure-velocity probes. Pressure probes are useful in such fields as active noise control[5,6,7]. Nearfield acoustical holography is another area where pressure may be used to calculate velocity and energy density[8,9]. Other areas include room acoustics, where room qualifying measurements can be made with fewer measurement positions, and be more uniform throughout the room when multiple microphone probes are used[10].

2.1 CALIBRATION

Calibration is the process of comparing the output value produced by a measuring device to a known or desired output. Typically the device being calibrated is subject to a known input value or measurement standard. This comparison will yield a correction or calibration factor that when applied to the output results, scales the results to match the known output, allowing for calibrated measurements[11].

A pressure transducer converts acoustic pressure to electrical voltage. The ratio at which the conversion takes place is known as the transducer sensitivity. Microphone sensitivities are usually given in units of mV/Pa (mille volts/Pascal). These sensitivities usually depend on frequency and are determined by a calibration technique.

Calibration techniques are categorized in two main groups, absolute calibration and relative calibration as shown in Figure 2–1. Absolute calibration is a process that determines the transducer sensitivity by indirect derivation or directly measuring a fundamental unit. Relative calibration is a process that determines the transducer sensitivity by comparing its response to the response of a transducer with a known sensitivity. The known sensitivity transducer in the relative calibration process is known as the reference transducer[12,13,14]. There are several methods to calibrate using both absolute and relative techniques. Two such methods pertaining to this research are presented.

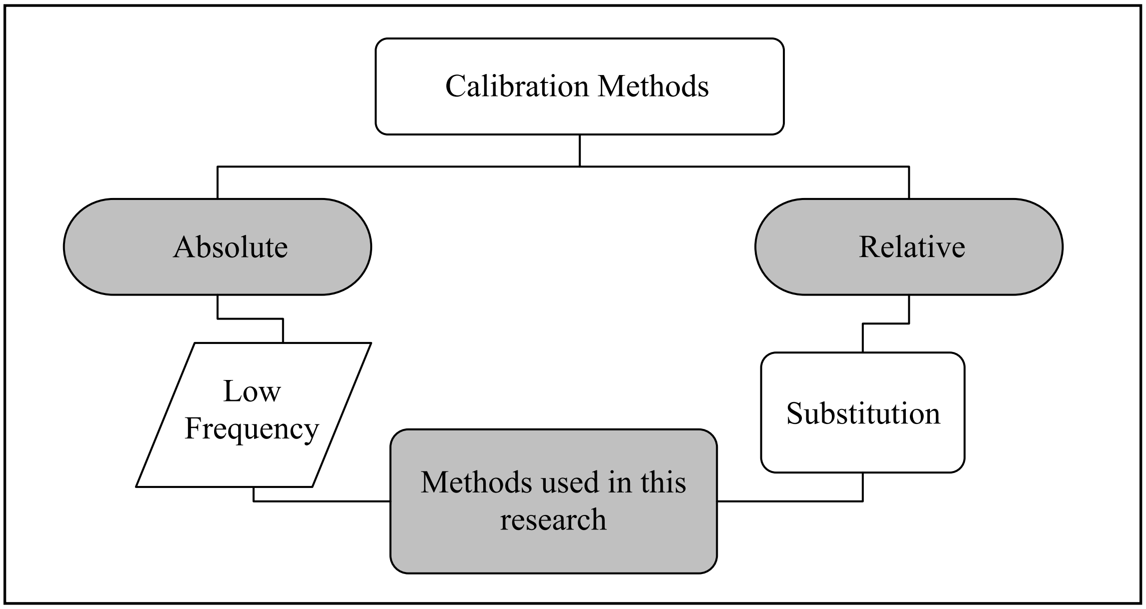

Figure 2–1: Calibration methods

The calibration methods used in this research are illustrated in Figure 2–1. The two main groups of calibration are relative calibration and absolute calibration. The two methods used in this research are the low frequency method and the substitution method. These two techniques are discussed in detail in the next two sections.

2.1.1 Absolute Calibration

The most direct way to absolutely calibrate a transducer is to subject it to a known physical quantity and measure the transducer output[14]. This method is known as the low frequency method[14]. Precision condenser microphones are typically calibrated using this method with a commercially available calibrator similar to those shown in Figure 2–2. The calibrators usually operate at one of two levels, (90 dB or 114 dB) and one of two frequencies 250 Hz or 1000 Hz. The disadvantages of this technique are that the calibration can only be performed at one or two frequencies, and the resulting sensitivity is based on the actual pressure at the microphone face and not the pressure that exists before the microphone disturbs the sound field. The latter disadvantage is neglected when the dimensions of the receiver are small compared to the wavelength of the calibration frequency. This method is popular because of simplicity and convenience.[12]

Figure 2–2: Larson Davis precision microphone calibrators

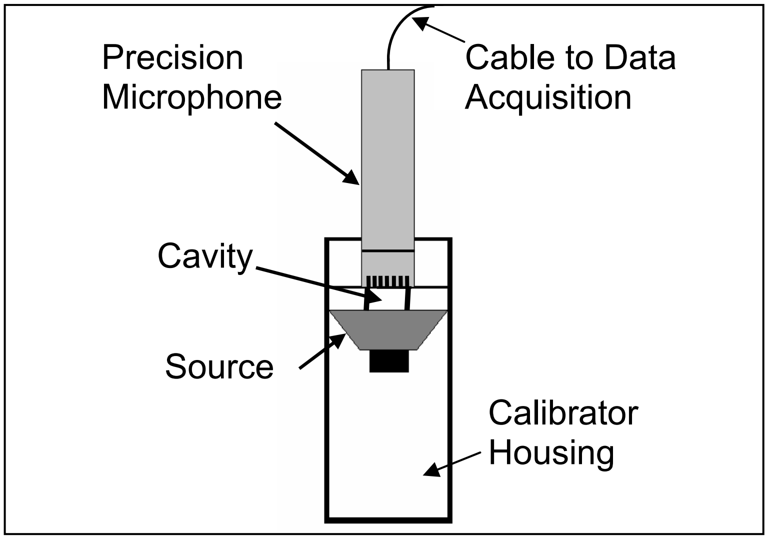

Figure 2–3: Precision microphone inside a calibrator

2.1.2 Relative Calibration

When an acoustic pressure transducer does not fall into the category mentioned above and absolute calibration is not feasible or practical, the transducer can be calibrated relative to a reference transducer. This relative calibration technique is useful when, for reasons such as cost, it is desired to use a lower quality transducer. Relative calibration allows the measurements made using the uncalibrated transducer to replicate measurements made with the reference transducer. If the reference transducer is a precision transducer and calibrated to an absolute reference like in the absolute calibration process described above, the uncalibrated transducer will yield precision measurements.

Certain acoustic applications require the use of multiple pressure transducers. These microphones can be relatively calibrated to a single precision microphone. All of the microphones being calibrated will produce quality results, making the application result valid.

A common relative calibration method for a microphone is known as direct comparison or the substitution technique[12,14–15]. This is accomplished by first creating a sound field with a linear source. The reference microphone with a known sensitivity is placed in the sound field, and the microphone frequency-dependent output is recorded. Next, the uncalibrated microphone is placed at the same location and orientation in the sound field, and the frequency-dependent output is again recorded. Figure 2–4 illustrates this method. The sensitivity of the uncalibrated microphone is obtained by using the sensitivity of the reference microphone to scale the ratio of the frequency-dependent outputs as given by Eq. (2.1)[12,14].

$$m_2 = m_1 \frac{V_U(f)}{V_R(f)} \tag{2.1}$$

In Eq. (2.1), m_1 is the sensitivity of the reference microphone and m_2 is the sensitivity of the uncalibrated microphone. $V_R(f)$ is the frequency-dependent output of the reference microphone, and $V_U(f)$ is the frequency-dependent output of the uncalibrated microphone.

2.2 CALCULATIONS USING MULTIPLE PRESSURE MEASUREMENTS

Two sound field quantities, acoustic pressure and the acoustic particle velocity, are needed to calculate total acoustic energy density (AED), acoustic intensity, and acoustic impedance. The pressure at a specific point is calculated either by using pressure measurements made with the several microphones or by direct measurements made by a microphone at the specific location. The particle velocity can also be measured or it can be calculated from the pressure measurements of two or more of the microphones

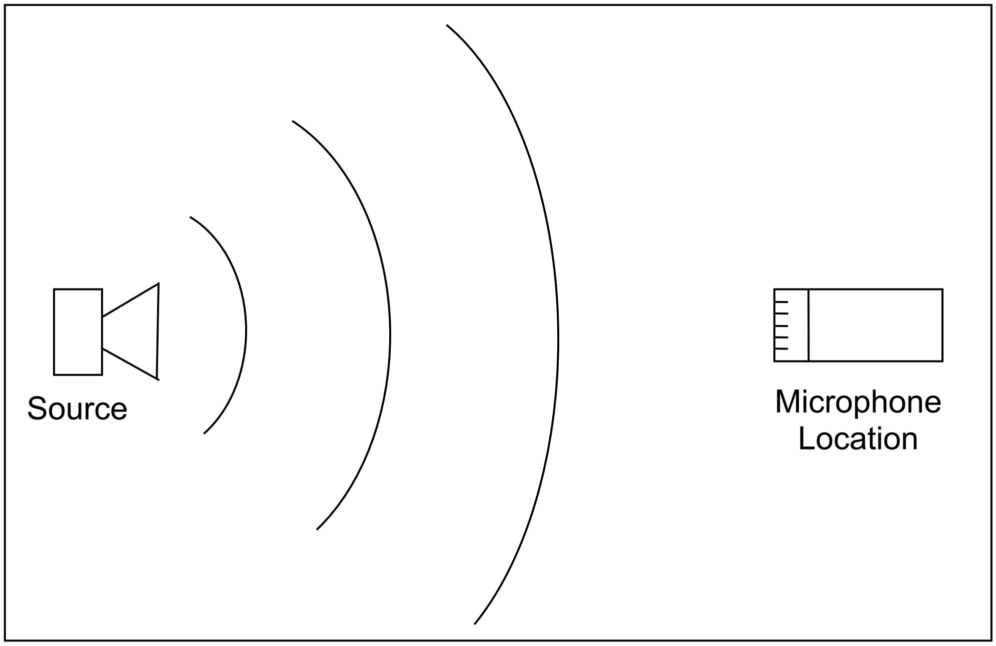

Figure 2–4: Substitution calibration setup

2.2.1 Calculating energy density

Total acoustic energy density is the sum of the acoustic potential energy density and the acoustic kinetic energy density as shown in Eq. (2.2).

$$w_{Total} = w_p + w_k \tag{2.2}$$

In Eq. (2.2), w_{Total} is the total AED, w_p is the acoustic potential energy density, and w_k is the acoustic kinetic energy density. The probes relevant to this research compute AED using pressure transducers. Other types of probes exist that use different methods to compute AED[3,16]. The potential energy density is calculated directly from the pressure measurements produced by the transducers as shown by Eq. (2.3)[12].

$$w_p = \frac{1}{2\rho_o c^2} p^2 \tag{2.3}$$

In Eq. (2.3), ρ_o is the ambient fluid density, c is the acoustic phase speed, and p is the acoustic pressure. The acoustic kinetic energy density is calculated using the particle velocity as shown in Eq. (2.4).

$$w_k = \frac{\rho_o}{2} u^2 \tag{2.4}$$

The particle velocity is calculated using the pressure difference between two of the microphones. This technique is referred to as the two-microphone technique and can be expressed as shown by Eq. (2.5)[12,14,17,18].

$$u \approx \frac{p_1 - p_2}{j\omega\rho_o \Delta x} \tag{2.5}$$

In Eq. (2.5), u is the acoustic particle velocity, p_1 and p_2 are the pressures at the two microphones, ω is the frequency of oscillation, Δx is the effective distance between the two microphones[19,20], and j is $\sqrt{-1}$. Since the particle velocity of the sound is directional, the two microphones used to get this pressure difference are used to obtain the component of particle velocity along the axis of the two microphones. Both the kinetic energy density and the potential energy density rely on the pressure measurements of the microphones. This dependence produces a need for accurate microphone measurements.

2.3 TYPES OF PROBES

Two types of probes are discussed in this section pressure-velocity probes, and pressure probes. Pressure-Velocity probes measure the particle velocity, and pressure probes calculate the velocity using pressure measurements. Both measure or calculate the pressure using pressure measurements.

2.3.1 Pressure-Velocity Probes

The Microflown USP is a pressure-velocity probe[21]. This sensor measures the velocity in each direction using two closely spaced wires that are heated with an electrical current. As the sound field flows past the two wires, the temperature around the wires changes. The sensor uses this change to determine the velocity perpendicular to the two wires[16,21]. Three sets of these wires are used to obtain the three orthogonal velocity measurements. Figure 2–5 a) shows the USP sensing head and Figure 2–5 b) is a scanning electron microscope image illustrating the spacing of the two wires.

The three velocity sensing sets of wires can be seen in Figure 2–5 a) oriented in three orthogonal directions. The pressure microphone is visible in the tip of the probe. Since there is only one microphone, the probe measures the acoustic quantity at that microphone. This probe uses two drastically different transducers to calculate a single acoustic quantity. The effects of using different transducers in this manner will be discussed later.

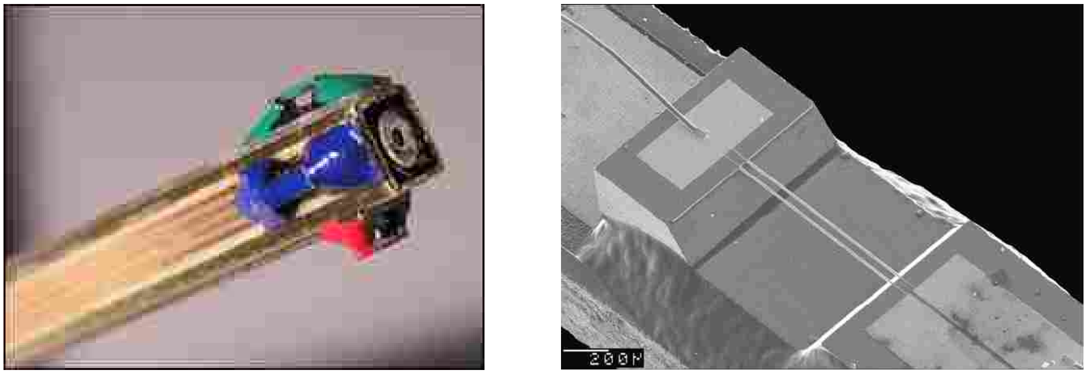

a) b)

Figure 2–5: a) Microflown USP b) SEM of USP velocity sensor

2.3.2 Pressure Probes

The particle velocity can be calculated using commercially available probes intended to measure intensity using microphones to calculate the velocity. This is possible because both AED and intensity as mentioned above are calculated using the acoustic pressure and three orthogonal velocity measurements. Cazzolato[3] discussed using two types of pressure probes that are commercially available as intensity sensors to measure AED. These two types use four microphones and six microphones. Figure 2–6 shows the Ono Sokki tetra-phone MI 6420, a four microphone intensity sensor. Figure 2–7 a) shows the B&K type 5356, and Figure 2–7 b) shows the GRAS vector intensity probe. Both use six microphones to calculate the particle velocity. These three probes have microphones mounted in an *open configuration* meaning the space between each microphone is open to the sound field[3].

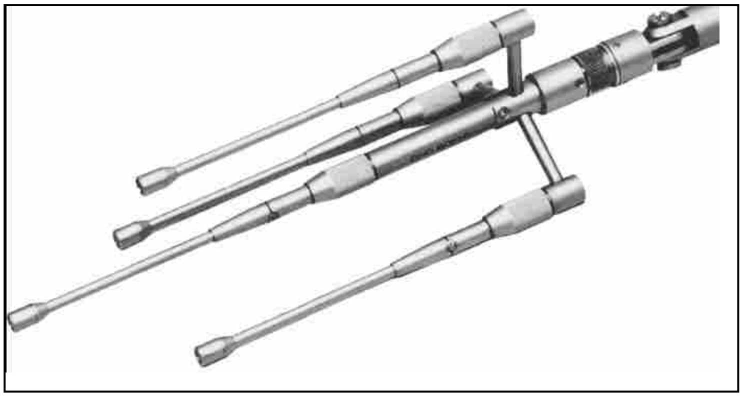

Figure 2–6: Ono Sokki Tetra-phone MI 6420

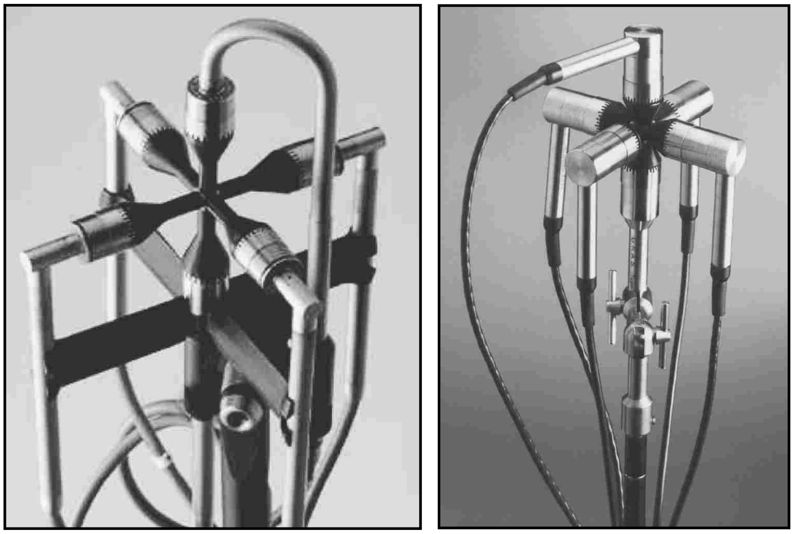

a) b)

Figure 2–7: a) B&K Type 5356 b) GRAS vector intensity probe

Elko[22] developed the idea of mounting the microphones in a hard sphere for a sensor used in active noise control. Parkins[18] furthered this and found for accurate AED calculations, the separation distance of the microphones needed to be scaled by a factor of 3/2 when mounted in the sphere compared to being freely mounted in an open configuration. Parkins et al.[18] also found that the spherical sensor errors were similar to the open sensors for both AED and intensity. Parkins[18] listed two advantages of mounting the microphones in a sphere over the open configuration. The first advantage is the sphere provides an easy way to locate and orient the microphones. The microphones were inexpensive electret microphones and need an external structure for positioning and protection. The second advantage is the sphere can be 2/3 the size of a sensor in the open configuration and not sacrifice accuracy. Figure 2–8 shows Parkins[18] sensor that he was able to build relatively inexpensively. The sensor performed properly only when the microphone's sensitivity and phase were matched.

Locey[20] compared three types of spherical pressure probes. These three probes are called the orthogonal, tetrahedron, and six-microphone probes. The orthogonal probe and a tetrahedron probe both use four microphones, and the six-microphone probe uses six microphones to calculate the AED measurement. Figure 2–9 shows the three probes from left to right as listed above. As can be seen from Figure 2–9 the microphones are located in different positions on the three spheres. The three are similar in function and appearance with the difference being the locations where the microphones are mounted in the sphere. These three probes were manufactured for the specific purpose of measuring AED. The probes consist of relatively inexpensive components and were designed to be a robust practical alternative to expensive sensors.

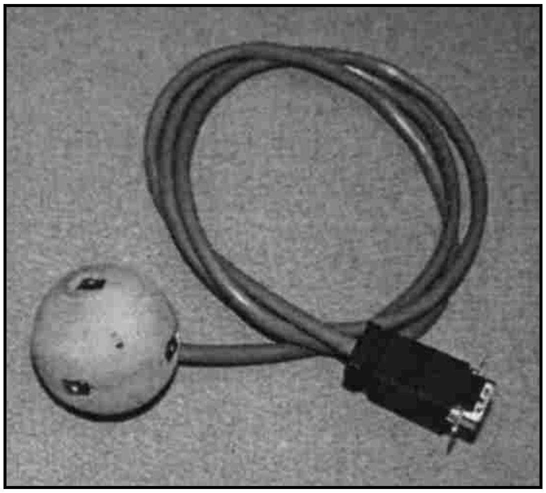

Figure 2–8: Parkins spherical AED sensor

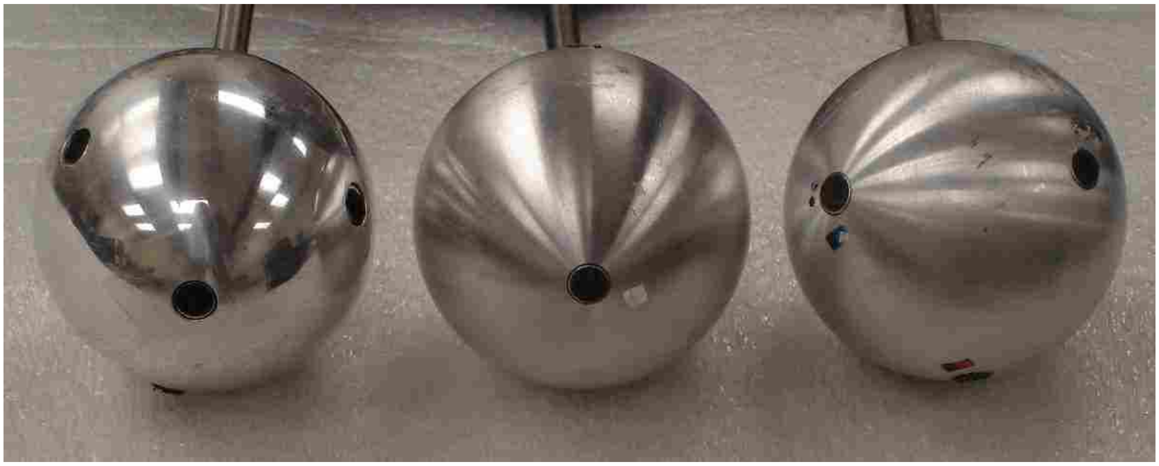

Figure 2–9: From left to right orthogonal, tetrahedron and six-microphone AED probes

2.3.3 The Orthogonal Acoustic Energy Density Probe

The probe of interest for this research was developed at Brigham Young University in connection with a NASA Small Business Innovation Research (SBIR) grant. Locey[20] referred to this probe as the orthogonal probe, and suggested, based on numerical results, that the orthogonal configuration produced the best results of the three probes compared. The probe was designed to operate between the frequencies of 0–2000 Hz.

The probe is spherically shaped as shown in Figure 2–9, with four pressure transducers mounted in the sphere. The sphere is 0.0508 m (2 inches) in diameter and made of solid aluminum. A hollow shaft is used to connect the sphere to the digital signal processor (DSP) housing. Wires pass through the shaft to connect the microphones to the DSP. The z-axis or the axis that runs down the length of the shaft is considered the natural axis of the sphere. One sensor microphone is mounted on the sphere opposite the shaft, and shares the same z-axis as the shaft. This microphone is known as the pole microphone. Figure 1–2 shows a computer aided drawing (CAD) model of the probe, and illustrates the probe DSP housing, the probe shaft, the pole microphone, two of the three side microphones, and the z-axis. The CAD model was generated in SolidWorks 2004.

The other three transducers known as the side microphones are located 68.75˚ off the z-axis as measured from the pole microphone. These three side microphones are spaced equally around the sphere at 120˚ increments. Figure 2–10 shows the probe sphere in two different orientations. The left orientation is a side view of the probe sphere showing the angle between the side microphones and the pole microphone. The right orientation is a top view of the probe that shows the angle between the three side microphones. The microphones used in this probe are Primo EM123 electret microphones. The four microphones were selected from a group of similar microphones based on the phase response. All four microphones are matched within 1 degree of phase. The phase of electret microphones does not change; therefore it was practical for the microphones to be phase matched. The amplitude response of the electret microphones does drift or change over time, and is not flat over frequency. These two characteristics require the probe to be calibrated over the entire frequency range of use, in order to obtain accurate measurements at those frequencies.

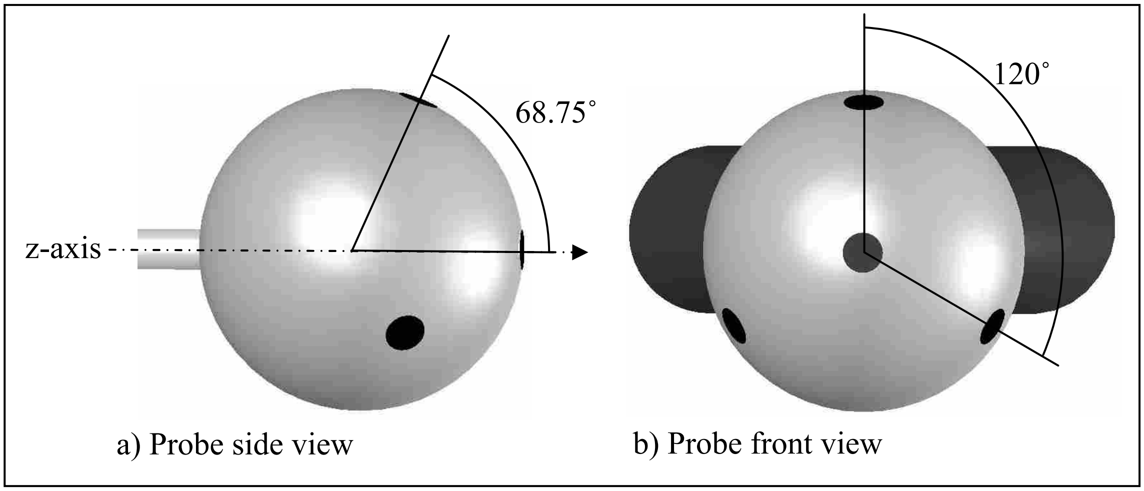

a) Probe side view b) Probe front view

Figure 2–10: Microphone locations

2.4 PROBE CALIBRATION

The pressure-velocity probes can be calibrated in several different ways. Raangs et al.[23] compared the Microflown calibration results when the probe was calibrated in a standing wave tube to the results when the probe was calibrated using laser Doppler anemometry. The standing wave tube is driven at $x = 0$ with a piston, and rigidly terminated at $x = l$. A reference microphone is used at $x = l$ in connection with the pressure microphone on the Microflown probe to obtain the particle velocity at the probe position x. Laser Doppler anemometry uses the Doppler shift to calculate the velocity of a particulate-laced air flow. The particles are small enough to follow the flow, yet large enough to measure with a laser. The optically measured velocity is then compared to the Microflown measurement and the sensitivity is obtained. These methods resulted in measurements with discrepancy of < 1dB for the frequency range of 250 Hz–4 kHz[23].

Jacobsen et al.[24] lists three additional methods to calibrate the Microflown probe. The first one is to use a simple source in a free field environment, and measure the pressure with a reference microphone. The simple source was simulated using a rigid hollow sphere with a loudspeaker inside. A small hole in the sphere allowed the sound to propagate as a point source. The second method is similar to the first except it was performed in a regular room instead of an anechoic chamber. The third method was done using a planar baffle to create the simple source instead of the sphere in a regular room. The best results were obtained using the spherically baffled source in the anechoic chamber. All three methods use a calibrated reference microphone to extract the probe sensitivity.

The pressure measuring intensity probes with the open microphone configurations can be easily calibrated using the absolute calibration described above. This is made possible by the open configuration, making the microphones accessible to commercially available calibrators like those shown in Figure 2–2.

Parkins[25] built a calibrator to calibrate the spherical sensor in Figure 2–8. This calibrator operated much like the absolute calibrator in Figure 2–3 and relied on the calibration cavity to be small compared to the wavelength of the frequency being used to calibrate. Parkins[25] considered the calibrator chamber to behave as a lumped capacitance.

This approach is referred to as a lumped parameter model. A lumped parameter model is valid as long as $ka << 1$, where a is the largest chamber dimension and k is the acoustic wave number. This means the largest chamber dimension needs to be less than 1/10th the size of the acoustic wavelength of the frequency used to calibrate[26].

If the lumped parameter model is valid, the acoustic pressure in the chamber is uniform. Unlike the calibrator in Figure 2–3 the pressure produced by the source was not known. The pressure was measured with a reference microphone. The calibrator was equipped with a hole that was lined with a gasket. The probe was placed over this hole with one of its microphones oriented inside the cavity. The gasket was designed to seal around the probe.

The reference microphone would measure the pressure produced by the source near the probe microphone. The reference microphone was calibrated previously using the absolute technique discussed in 2.1.1. The probe was then calibrated using the relative calibration technique described in Section 2.1.2. Figure 2–11 is a schematic of this calibrator. The calibrator produced valid results in the frequency range of 20–400 Hz. Due to the low frequency nature of active noise control this frequency range was adequate for the sensor application.

Locey[20] used a similar method to calibrate the three probes in Figure 2–9. These probes had a higher frequency limit (2000 Hz) than the probe developed by Parkins[25]. Locey[20] questioned the accuracy of the calibration method for this higher frequency limit and the repeatability of the seal provided by the gasket from one probe microphone to the next. Both Parkins[25] and Locey[20] indicate that leaking occurred in the respective calibrator cavities. The leaking could also lead to inconsistencies in the calibration. In theory, this method would be more reliable if the entire probe was placed inside the cavity. This would allow all four microphones to be calibrated simultaneously, and eliminate the variance in seal. The theory is not physically realizable, because when the chamber is made large enough to enclose the probe the lumped parameter assumption is no longer valid.

The lumped parameter assumption would be valid at the probes upper frequency limit if the largest calibrator cavity dimension were 0.017m. It is not feasible for a 0.017 m cavity to enclose a probe with a diameter of 0.0508 m. If the cavity is made larger it could enclose the probe, but this would limit the calibrator frequency range, and limit the frequencies at which the probe can measure accurately.

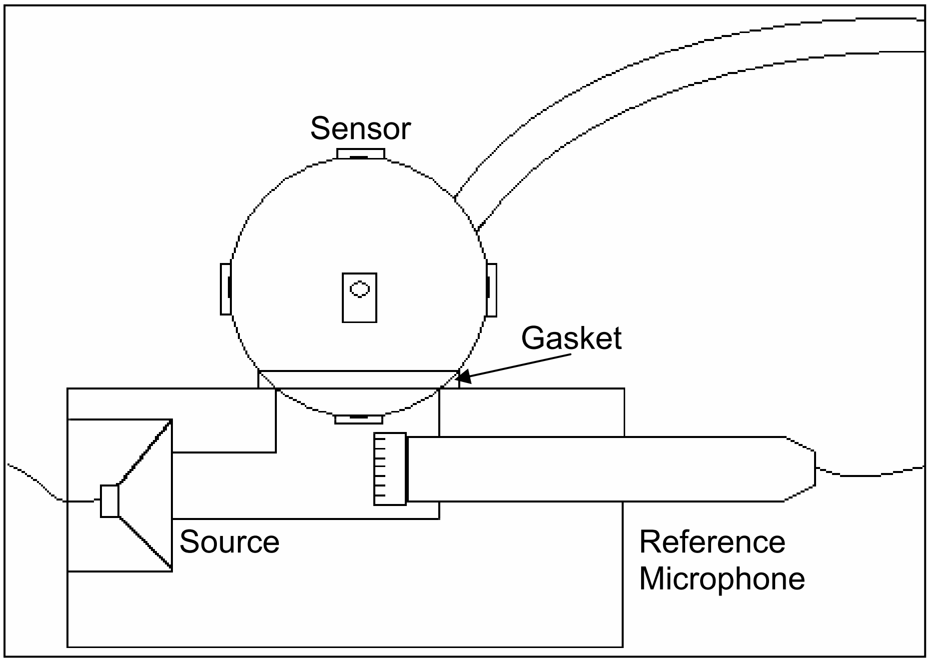

Figure 2–11: Parkins' calibrator

3 THEORY

This chapter presents the new calibrator concept, and discusses the theory behind the new calibrator design. In this chapter, waveguides are introduced. The fundamentals of acoustic waves in waveguides with circular cross-sections are presented. The cutoff frequencies for the first three higher order modes are given. The pressure distribution and node lines of the first three higher order modes in a circular waveguide are shown.

3.1 NEW CALIBRATOR PATH CONCEPT

A concept with individual identical paths to each microphone was developed. The theory behind the concept was derived from the circuit shown in Figure 3–1. In Figure 3–1, U is a volume velocity (m^3/sec) source, and Z_A is the acoustic impedance (Newtons-sec/m^5) for the paths[27]. This circuit is simplified to visualize the concept. This path concept provided a sound path for each of the probe microphones. In theory, if each of these paths is identical from source to termination, as shown in Figure 3–1, then the acoustic pressure would be identical at every point along the path and most importantly at the end where the probe microphones measure. This concept can be physically realized if the pressure from a source can be the same at the entrance to all of the paths, and if all of the paths can be created acoustically identical.

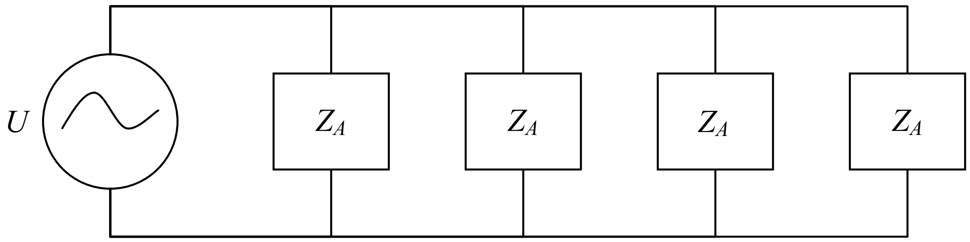

Figure 3–1: Calibrator path concept circuit

3.2 WAVEGUIDE

It was hypothesized that the path concept could be physically realized using acoustically rigid walled uniform circular waveguides, or tubes. Uniform waveguides can have a cross-section of any shape as long as the cross-section is constant along the length of the waveguide. A waveguide that is excited by a source will potentially contain both a fundamental and higher order modes.

3.2.1 Modes

The fundamental mode is called the plane wave mode. The characteristic property of a plane wave is that each acoustic quantity has constant amplitude and phase on any plane perpendicular to the direction of propagation[12]. Since the pressure is uniform over the cross-section of the waveguide, the plane wave mode only propagates along the axis of the waveguide. The higher order modes, called cross-modes are modes that propagate in the transverse and axial directions of the waveguide. Figure 3–2 a) is a two dimensional view of plane waves propagating in a waveguide, and Figure 3–2 b) is a two dimensional view of the direction of propagation of an arbitrary higher order mode in a waveguide. The arrows indicate the direction of propagation of the plane wave and the cross mode in Figure 3–2 a), and Figure 3–2 b) respectively. Figure 3–2 a) further describes the plane wave with lines to illustrate the wave front. The wave front is not shown for the cross-mode in Figure 3–2 b). The wave front for the cross-mode is not uniform over the cross-section of the waveguide, but would be perpendicular to the direction of propagation.

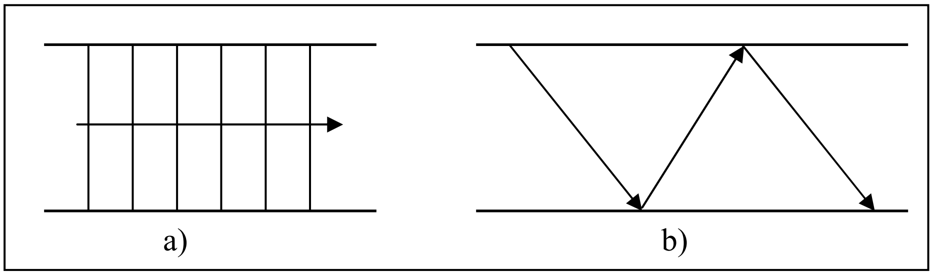

Figure 3–2: 2-D illustration of a) a plane wave and b) a cross mode inside a waveguide

3.3 WAVES IN A WAVEGUIDE

Consider an acoustically rigid walled waveguide with circular cross-section like the one shown in Figure 3–3. In Figure 3–3, the cross-section is defined in the *x-y* plane where r is the radius and ϕ is the angle as shown. For the time-harmonic condition, the acoustic pressure $\hat{p}$ in the waveguide satisfies the homogeneous Helmholtz[26] equation,

$$\nabla^2 \hat{p} + k^2 \hat{p} = 0 \tag{3.1}$$

where $k = \omega/c$ is the acoustic wave number, with ω and c being the frequency in rad/sec and the phase speed of sound in air respectively, and ∇^2 is the Laplacian[26] operator defined as

$$\nabla^2 = \frac{\partial^2}{\partial r^2} + \frac{1}{r^2}\frac{\partial^2}{\partial \phi^2} + \frac{\partial^2}{\partial z^2} \tag{3.2}$$

The acoustic pressure can be expressed as

$$\hat{p}(r,\phi,z) = R(r)\Phi(\phi)Z(z) = \Psi(r,\phi)Z(z) \tag{3.3}$$

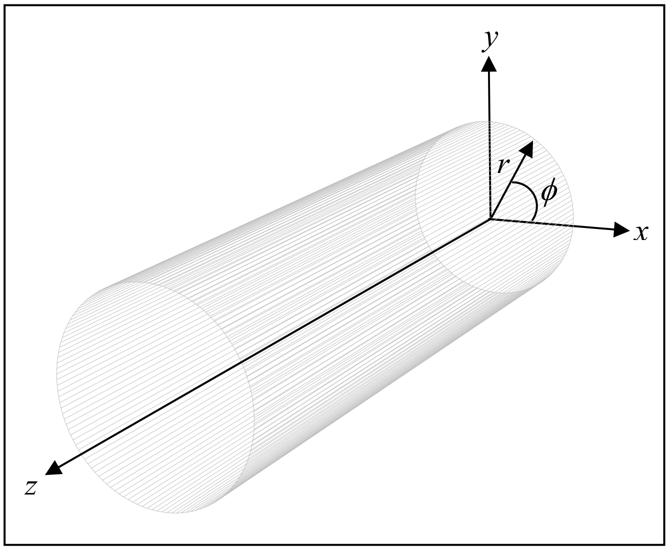

Figure 3–3: Rigid-walled waveguide with circular cross-section

In Eq. (3.3), Ψ represents the pressure over the cross-section and Z represents the pressure along the length of the waveguide. Substituting Eq. (3.3) into Eq. (3.1) and dividing through by ΨZ leads to

$$\frac{1}{\Psi}\nabla_{cs}^2\Psi + \frac{1}{Z}\frac{d^2Z}{dZ^2} + k^2 = 0 \tag{3.4}$$

where ∇_{cs}^2 is the two-dimensional Laplacian operator for the cross-section. Letting

$$k^2 = k_{cs}^2 + k_z^2 \tag{3.5}$$

where k_z is the wave number along the length of the tube, and k_{cs} is defined below allows Eq. (3.4) to be separtated into two equations

$$\nabla_{cs}^2\Psi + k_{cs}^2\Psi = 0 \tag{3.6}$$

$$\frac{d^2Z}{dZ^2} + k_z^2 Z = 0 \tag{3.7}$$

For Eq. (3.6), there are several particular solutions (denoted n = 0, 1, 2, 3, . . .) where the eigenfunction Ψ_n satisfies Eq. (3.1) and the eigenvalue $k_{cs,n}^2$ is one of a discrete series of real positive numbers for which a nontrivial solution of the closed region boundary-value problem exists[26].

For Eq. (3.7) the solution exists such that

$$Z(z) = A_z \sin k_z z + B_z \cos k_z z = C_z e^{-jk_z z} + D_z e^{+jk_z z} \tag{3.8}$$

and

$$k_z = \pm\sqrt{k^2 - k_{cs,n}^2} \tag{3.9}$$

Thus from Eq. (3.3) the modal pressure in the waveguide is represented as

$$\hat{p}_n = \Psi_n (C_z e^{-jk_z z} + D_z e^{+jk_z z}) \tag{3.10}$$

For waves traveling in the positive *z* direction, the pressure becomes

$$\hat{p}_n = C_z \Psi_n e^{-jk_z z} = C_z \Psi_n e^{-j\sqrt{k^2 - k_{cs,n}^2}\, z} \tag{3.11}$$

From Eq. (3.11) there exist three possible outcomes depending on the mode. In the first outcome, the mode will propagate along the axis of the waveguide. In the second outcome, the mode will decay along the axis of the waveguide. In the third outcome, the cutoff frequency will result.

3.3.1 Propagating Modes

The first outcome occurs when the mode propagates along the axis of the waveguide. For a given mode *n* if $k^2 > k_{cs,n}^2$ then the mode propagates along the length of the waveguide. This means the pressure is moving in the positive *z* direction since Eq. (3.10) is defined in the positive *z* direction. As shown in Figure 3–2 a) and b) both the plane wave mode and the higher order modes propagate along the length of the waveguide.

3.3.2 Evanescent Modes

The second outcome occurs when the mode decays along the axis of the waveguide. If for a given mode *n,* $k^2 < k_{cs,n}^2$, the only possible solution for physical reasons is the decaying solution therefore

$$\hat{p}_n = C_z \Psi_n e^{-\sqrt{k_{cs,n}^2 - k^2}\, z} \tag{3.12}$$

With increasing *z,* the pressure decays exponentially. This type of mode is known as an evanescent mode[26]. In this case the axial particle velocity ($\hat{u}_z$) is found using Euler's equation Eq.(3.13)[12]. Euler's equation relates the pressure to the velocity as shown. If the particle velocity is compared to the pressure $\hat{p}_z$ there is a phase shift of 90˚. This means for an evanescent mode the intensity $I = 0$, therefore no net transport of energy will take place along the length of the waveguide[26].

$$\rho_o \frac{\partial \vec{u}}{\partial t} = -\nabla p \tag{3.13}$$

If a higher order mode is decaying along the axis of the waveguide, it is possible to predict the attenuation of the mode as a function of position z. The attenuation between points z_1 and z_2 in dB can be calculated using Eq. (3.14)[14].

$$Attenuation = 20\log\left|\frac{\hat{p}_n(z_2)}{\hat{p}_n(z_1)}\right| \tag{3.14}$$

In Eq. (3.14) the pressure $\hat{p}_n$ is calculated using Eq. (3.12), and z_1 and z_2 are the starting and ending positions respectively.

3.3.3 Cutoff Frequency

The third outcome for a given n occurs when $k^2 = k_{cs,n}^2$ this means $k_z = 0$ which means the mode is not propagating along the length of the waveguide. The mode not propagating implies a cutoff frequency for that mode[14]. The cutoff frequency of a mode in a waveguide is the frequency above which the cross mode propagates, and below which the mode evanesces. The cutoff frequency for the *n*th mode in a waveguide with a circular cross-section is defined as

$$\omega_n = ck_{cs,n} \tag{3.15}$$

in radians per second and

$$f_n = \frac{ck_{cs,n}}{2\pi} \tag{3.16}$$

in Hz. The eigenvalues $k_{cs,n}$ for an acoustically rigid-walled waveguide with a circular cross-section are the roots of the modified Bessel function of the first kind divided by the radius. For *n* = 1–3, the first three higher order modes correspond to $k_{cs,1}$ = 1.84/a, $k_{cs,2}$ = 3.05/a, and $k_{cs,3}$ = 3.83/a. For *n* = 0, $k_{cs,0}$ = 0, and from Eq. (3.6), Ψ_0 is constant. Figure 3–4 shows pressure distribution and node lines of the fundamental mode and the first three higher order modes of a circular waveguide. In Figure 3–4 the dashed lines represent the node lines where the pressure is zero, and the plus and minus signs show where the relative pressure magnitude is positive and negative respectively. As shown in Figure 3–4 the first three higher order modes are the first two circumferential modes and the first radial mode.

The cutoff frequency for the plane wave mode is f_0 = 0 Hz, and the cutoff frequency of the first three cross modes shown in Figure 3–4 is $f_1 = 1.84c/2\pi a$,

$f_2 = 3.05c/2\pi a$, and $f_3 = 3.83c/2\pi a$ respectively[14]. Figure 3–5 illustrates the modes that propagate along the length of the waveguide as a function of frequency. In Figure 3–5 f_1, f_2, and f_3 represent the cutoff frequencies of higher order modes 1, 2, and 3 respectively. The plane wave mode always propagates and since Ψ_0 is constant does not vary over the cross-section as shown in Figure 3–2 a) and Figure 3–4.

If a waveguide is driven below the cutoff frequency of the first higher order mode f_1, the source will excite all of the higher modes, but they will evanesce along the axis of the waveguide as the distance from the source increases. The attenuation of decaying higher order modes excited by the driver is described in Eq. (3.14). For most practical applications the attenuation is calculated from the source at $z_1 = 0$. If $z_1 = 0$ Eq. (3.14) becomes

$$Attenuation = 20\log\left(e^{-kz_2\sqrt{\left(\frac{f_n}{f}\right)^2 - 1}} \right) \tag{3.17}$$

In Eq. (3.17), f_n is the cutoff frequency of the mode that is attenuating along the length of the waveguide, k is the acoustic wave number, z_2 is the distance from the source, and f is the frequency of excitation. For a tube with a circular cross section in air, f_1 is approximately equal to $100/a$, where a is the radius of the tube [12].

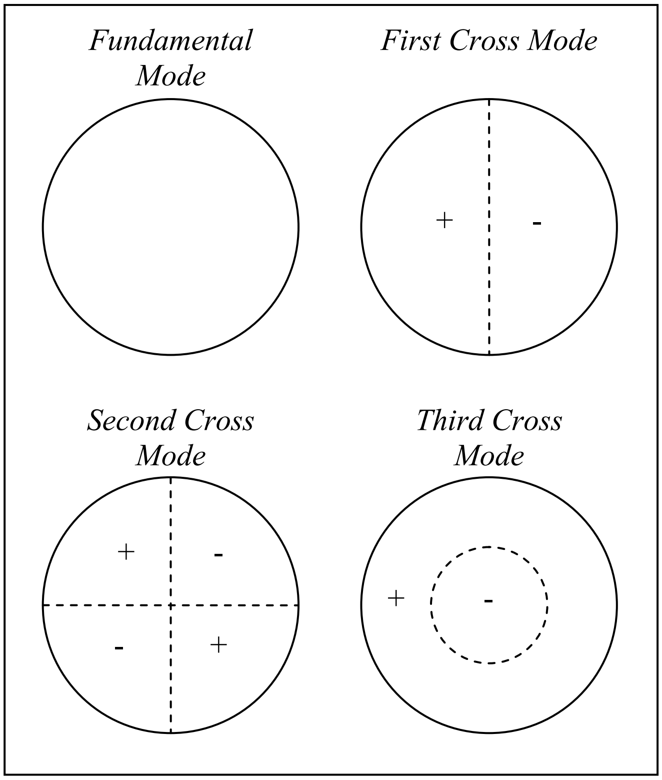

Figure 3–4: Pressure distribution and node lines in a circular waveguide

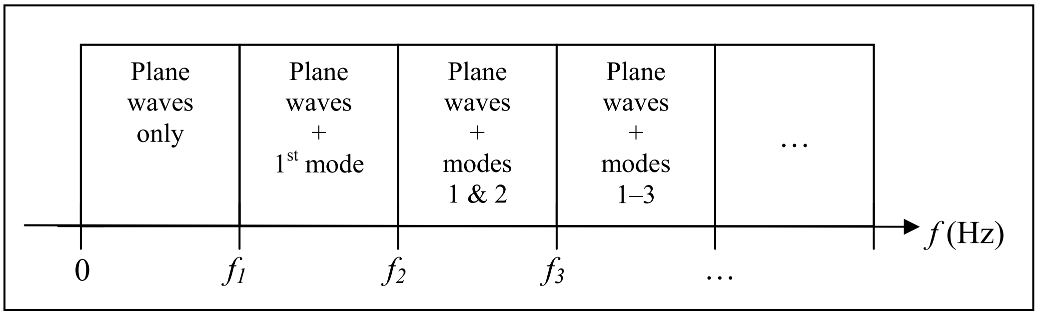

Figure 3–5: The modes propagating in a waveguide as a function of frequency

4 EQUIVALENT CIRCUIT MODEL

This chapter discusses the method of modeling acoustic waveguides using equivalent circuits. An acoustic impedance circuit for a one-dimensional finite-length waveguide is presented. The calibrator model is shown in three progressive stages. The first stage is the ideal case, the second stage accounts for thermoviscous losses in the tubes, and the third stage includes the actual driver parameters. The third stage requires the development of an equivalent circuit model for the calibrator driver. The results from the three model stages are presented and discussed.

4.1 ACOUSTIC IMPEDANCE OF A WAVEGUIDE

Waveguides can be modeled below the cutoff frequency of the first cross mode (f_1) using acoustic equivalent circuits. Figure 4–1 shows an acoustic impedance circuit for a finite-length one-dimensional waveguide with an arbitrary source at one end and an arbitrary termination at the other[28]. The source can be the impedance of another waveguide connected in series or a driver. The termination can be a rigid wall or another waveguide connected in series. In Figure 4–1, U_1 and U_2 are the volume velocities, and $\hat{P}_{(0)}$ and $\hat{P}_{(l)}$ are the acoustic pressures at the source and the termination respectively. Z_{A1} and Z_{A2} are the acoustic impedances of the waveguide and are defined in Eq. (4.1) and Eq. (4.2) respectively. In Eq. (4.1) and Eq. (4.2), S is the cross-sectional area of the waveguide

(m^2), k is the acoustic wave number defined as ω / c (rad m^{-1}), and l is the length of the waveguide (m). The three impedances shown in Figure 4–1 are combined to calculate the total acoustic impedance of a waveguide.

$$Z_{A1} = j\frac{\rho_o c}{S}\tan(kl/2) \tag{4.1}$$

$$Z_{A2} = -j\frac{\rho_o c}{S}\csc(kl) \tag{4.2}$$

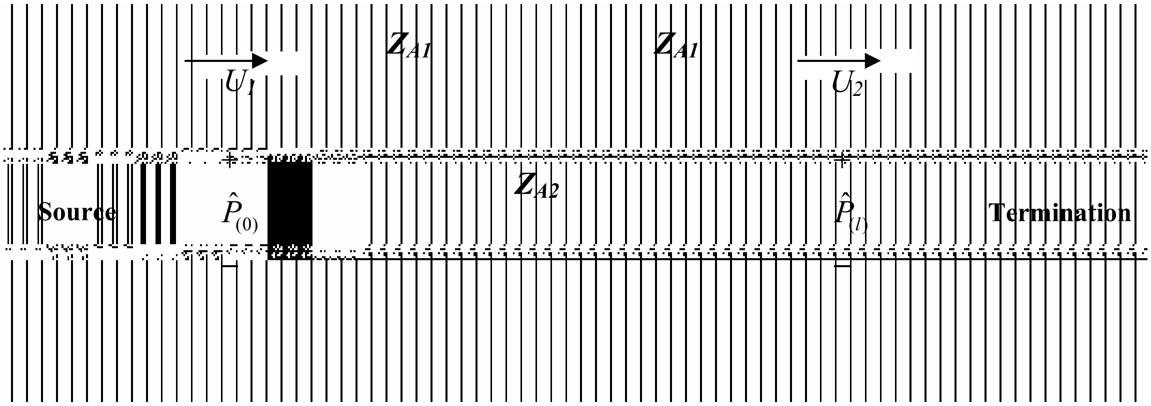

Figure 4–1: An acoustic impedance circuit for a finite-length one-dimensional waveguide

4.2 CALIBRATOR MODEL

The circuit in Figure 4–1 was used to create an acoustic impedance model of the entire calibrator. The calibrator was modeled in three progressive stages. In the first stage, two ideal assumptions were used. The source was assumed to be a constant volume velocity source, and the waveguides were assumed to have no losses. The second stage included the waveguide losses to increase the accuracy of the model. The third stage included the actual calibrator driver in the model.

The calibrator uses circular waveguides to channel the sound from the source to the receiver. For the sound to travel from the source to one receiver, it must pass through several acoustic discontinuities, or changes in the waveguide cross-section. The calibrator consists of four different sized waveguides. The sound field is generated at the source and travels through a primary waveguide (the driver tube). Then the sound field is divided into five paths, one path for each of the four probe receivers and the fifth path for a reference microphone.

Once the sound field is split, it travels through three different sized waveguides. Each of these waveguides was included in the model. The circuit shown in Figure 4–1 was used to model all of the calibrator waveguides individually. Figure 4–2 shows the equivalent acoustic impedance circuit for the primary waveguide in series with the five parallel paths. Notice the similarities between Figure 4–2 and Figure 3–1. In Figure 4–2 U is the volume velocity produce by the source, $Z_{A\ prim}$ is the acoustic impedance of the primary waveguide (before the sound field is split), and Z_{A1}-Z_{A5} is the acoustic impedance of the five paths.

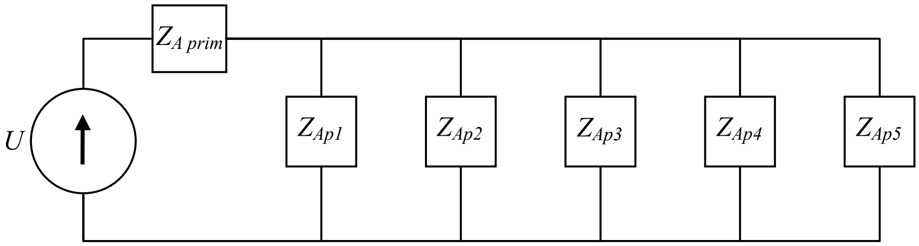

Figure 4–2: Acoustic impedance circuit of the calibrator

In Figure 4–2, $Z_{A\,prim}$ is calculated using the circuit shown in Figure 4–1 with Eq. (4.1), and Eq. (4.2). The equivalent acoustic impedance of the paths Z_{A1} through Z_{A5} are obtained by combining three circuits shown in Figure 4–1 in series. Paths Z_{A1} through Z_{A5} consist of three waveguides combined in series. Figure 4–3 is an equivalent circuit showing the three waveguides in series for a single path. Since each path is the same, the circuit in Figure 4–3 is used to model all five paths.

In Figure 4–3 Z_{AT} is the acoustic impedance of the termination. Z_{A11}, Z_{A21}, and Z_{A31}, are calculated using the length and cross-sectional area of the respective waveguides in the path using Eq. (4.1). Z_{A12}, Z_{A22}, and Z_{A32} are calculated using the length and cross-sectional area of the respective waveguides in the path using Eq. (4.2).

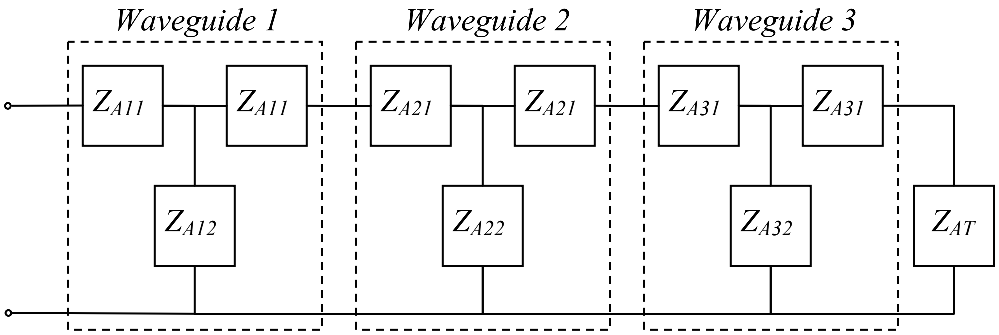

Figure 4–3: Path Acoustic impedance circuit

4.2.1 Effective Acoustic Length Corrections

For all of the waveguides in the path circuit shown in Figure 4–3, the impedances were calculated using the actual cross-sectional area of the waveguide in Eq. (4.1) and Eq. (4.2). The length used in the calculation was longer than the actual length of the waveguide. The added length is a result of diameter changes in the waveguides. These diameter changes are referred to as discontinuities or a diameter step[29]. At a waveguide diameter step the acoustic wave is divided into reflected and transmitted portions[30]. The reflected and transmitted parts of the wave produce an acoustic inductance. The diameter steps can be simulated in an equivalent circuit model as a lumped inductance element called discontinuity inductance[31]. This inductance can be interpreted physically as an increase in the equivalent length of the waveguide.

The primary wave guide was assumed to have a near rigid termination because the five path radii were much smaller than the radius of the primary waveguide. The radius of waveguide 1 in Figure 4–3 is smaller than the primary waveguide and waveguide 2 in Figure 4–3. When a waveguide with a small radius is inserted between two waveguides with larger radii, it forms a constriction inductance[31]. The effective acoustic length L_{eff} of a constriction inductance shown in Eq. (4.3), can be considered as a correction term for the acoustic length of the waveguide[31].

$$L_{eff} = L + \frac{8a}{3\pi}\left(H(\alpha_1) + H(\alpha_2)\right) \tag{4.3}$$

In Eq. (4.3) L is the actual length of the waveguide, a is the radius of the waveguide, and $H(\alpha_1)$ and $H(\alpha_2)$ are the correction factors accounting for the discontinuity on the first and second constriction ends respectively. In Eq. (4.3) α_1 and α_2 are the ratios of the smaller radius to the larger radii of the waveguides. These correction factors are the result of an infinite sum. Karal[31] provides a plot from which these correction factors were approximated for the model.

The diameter step between waveguide 2 and waveguide 3 of the circuit in Figure 4–3 was approximated similar to the constriction, the difference being only one correction factor was used because waveguide 3 is rigidly terminated.

4.2.2 Path Termination Impedance

A microphone in the actual calibrator terminates each path. The termination acoustic impedance Z_{AT} for the model was assumed to be much greater than the acoustic impedance of the waveguides. If Z_{AT} is considered infinite, the circuit in Figure 4–3 is shorted across Z_{AT}. The resulting circuit modeling the three waveguides in each of the five paths becomes the circuit shown in Figure 4–4. The acoustic impedance at the end of the path then becomes Z_{A32} in the circuit in Figure 4–4.

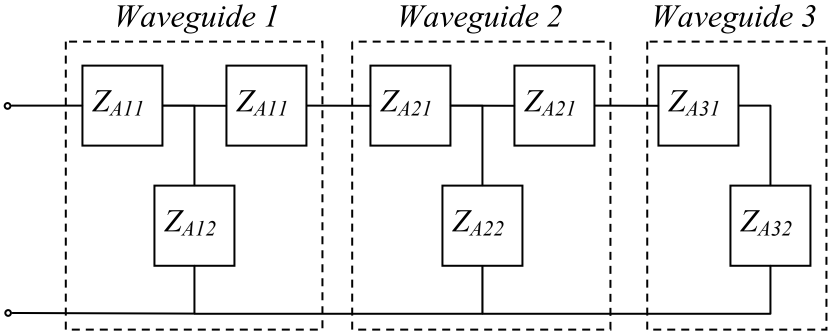

Figure 4–4: Path Acoustic impedance circuit with infinite termination impedance

4.2.3 Idealized Model

The circuits shown in Figure 4–1, Figure 4–2, and Figure 4–4 were used to obtain the Thevenin equivalent impedance of the entire calibrator circuit model[32]. A Thevenin equivalent circuit is a circuit that is reduced down to a minimal number of sources and loads by adding all of the sources and loads to create equivalent sources and loads. In the ideal case the calibrator is driven with a single constant volume velocity source, and there are no losses as the sound field travels through the waveguides. Figure 4–5 shows the Thevenin equivalent circuit where Z_{ATh} is the Thevenin equivalent impedance of all five of the paths combined. In Figure 4–5, the impedance of the primary waveguide $Z_{A\ prim1}$ and $Z_{A\ prim2}$ is determined using Eq. (4.1) and Eq. (4.2) respectively. To obtain the volume velocity where the calibrator splits the sound field into the five paths, mesh current analysis is performed on the circuit in Figure 4–5.

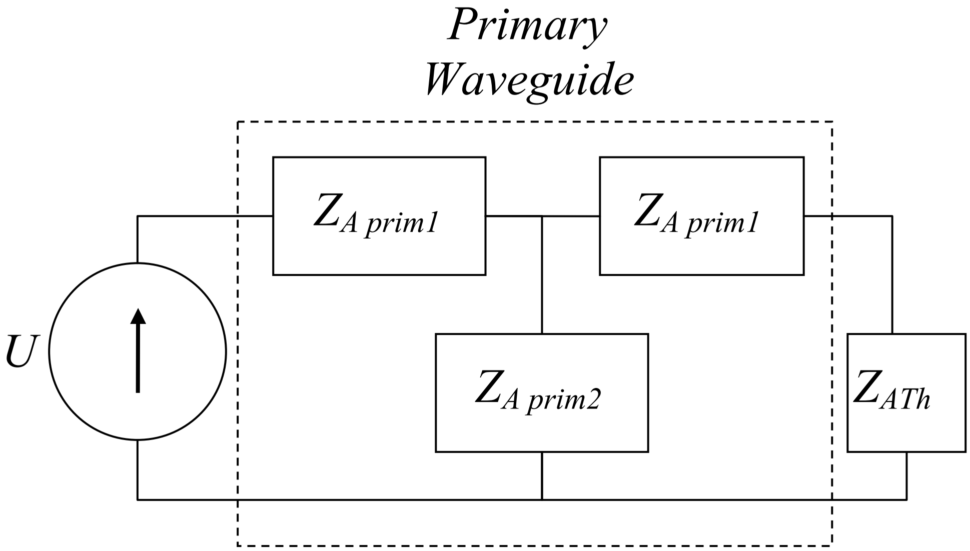

Figure 4–5: Thevenin equivalent calibrator circuit model

Mesh current analysis is performed in four simple steps[32]. The first step is to define each mesh current consistently. Unknown mesh currents are always defined in the clockwise directions. A mesh current is known when a current source is present in the mesh, and is defined in the direction of the current source. The second step is to determine the circuit system of equations. A circuit with n meshes and m current sources will result in $n - m$ independent equations, and the $n - m$ independent variables are the unknown mesh currents. The third step is to apply Kirchhoff's voltage law, or KVL as shown in Eq. (4.4) where the v_n are the individual voltages around the closed circuit. In a circuit that represents an acoustic system, the voltage or potential of the circuit models the acoustic pressure of the system.. KVL is based on the principle that no energy is lost or created in an electric circuit, so that the net voltage around a closed circuit is zero[32]. The fourth step is to solve the linear system of equations for $n - m$ unknowns.

$$\sum_{n-1}^{N} v_n = 0 \tag{4.4}$$

The circuit shown in Figure 4–6 shows the mesh analysis of the circuit shown in Figure 4–5. In the circuit in Figure 4–6, U_1, the volume velocity around the first loop (*Mesh 1*), is defined in the direction of the current source U, and U_2, the volume velocity around the second loop (*Mesh 2*), is defined in the clockwise direction. In the ideal case where a constant volume velocity source is assumed, U_1 is the known volume velocity U produced by the source. The circuit contains two meshes and one current source that results in one independent equation with one independent variable that is the unknown variable. The unknown variable is the mesh 2 current U_2. Equation (4.5) shows the equation used to solve for U_2 in terms of the known volume velocity source U_1, the primary wave guide impedance $Z_{A\ prim1}$ and $Z_{A\ prim2}$, and the Thevenin equivalent impedance of all of the paths Z_{ATh}.

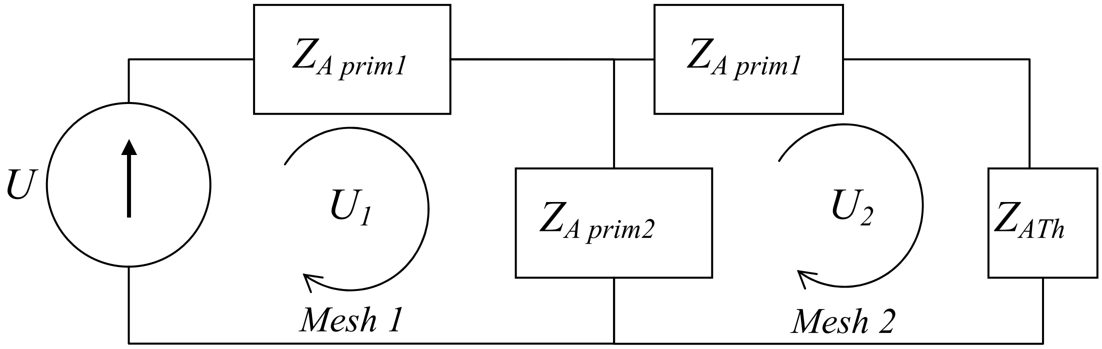

Figure 4–6: Thevenin mesh current analysis circuit

$$U_2 = \frac{Z_{Aprim2} U_1}{Z_{Aprim1} + Z_{ATh} + Z_{Aprim2}} \tag{4.5}$$

The sound field is split into five equal parts for the five paths, therefore U_2 is divided into five parts. The volume velocity that travels down a single path is $U_2/5$. Each path in the circuit in Figure 4–2 has the equal volume velocity of $U_2/5$. With the volume velocity into each path known, the mesh analysis is performed on the circuit shown in Figure 4–4 as illustrated in Figure 4–7. In the circuit $U_{p1} = U_2/5$ is the known volume velocity around the first path loop *Mesh 1*, U_{P2} is the unknown volume velocity around the second path loop *Mesh 2*, and U_{p3} is the unknown volume velocity around the third path loop *Mesh 3*.

In the circuit in Figure 4–7, there are three meshes and two unknown currents resulting in two independent equations with two independent variables. The first equation is derived by performing the mesh current analysis on the second loop of the circuit in Figure 4–7.

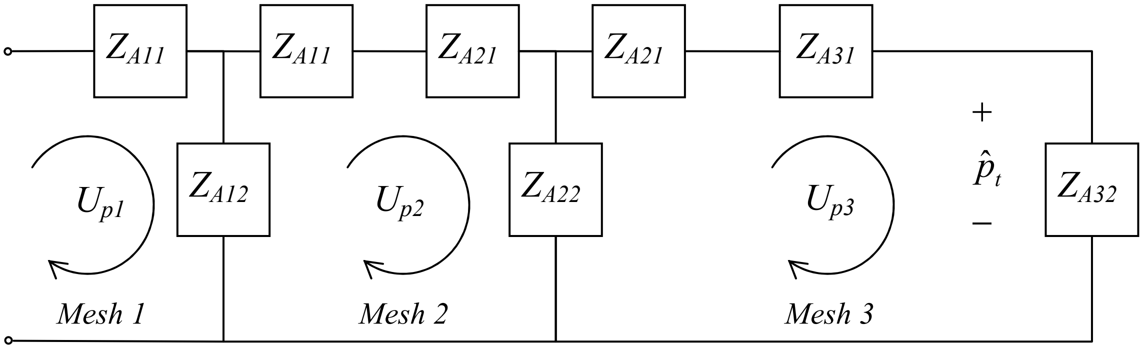

Figure 4–7: Path mesh current analysis circuit

The resulting equation is

$$Z_{A11}U_{p2} + Z_{A21}U_{p2} + Z_{A22}\left(U_{p2} - U_{p3}\right) + Z_{A12}\left(U_{p2} - U_{p1}\right) = 0 \qquad \textbf{(4.6)}$$

The second equation is derived by performing the mesh current analysis on the third loop of the circuit in Figure 4–7. The equation is

$$Z_{A21}U_{p3} + Z_{A31}U_{p3} + Z_{A32}U_{p3} + Z_{A22}\left(U_{p3} - U_{p2}\right) = 0 \qquad \textbf{(4.7)}$$

Eq. (4.6) and Eq. (4.7) are solved simultaneously for the two independent unknown variables U_{p2} and U_{p3}. U_{p3} represents the volume velocity at the end of the path.

The acoustic pressure at the end of the path is calculated by multiplying the impedance at the end of the path Z_{A32} by the volume velocity at that point U_{p3} as shown in Eq. (4.8)[12]. In Eq. (4.8) $\hat{p}$ is the complex pressure. This is the pressure that each of the probe microphones and the reference microphone will measure in the actual calibrator.

$$\hat{p} = Z_{A32} U_{p3} \tag{4.8}$$

4.2.4 Lossy Model

To increase the accuracy of the model, the thermoviscous losses in the waveguides were included. For gases, the absorption associated with heat conduction is less than that for viscous absorption but both are of comparable magnitude. The historical development of the study of absorptive processes in fluids led to the definition of the *classical absorption coefficient*[12]. The classical absorption coefficient accounts for the thermal and viscous losses due to the fluid. Eq. (4.9) shows the classical absorption coefficient, where ω is the angular frequency in *radians/sec*, ρ_o is the fluid density in *kg/m*^{3}, and c is the phase speed in *m/sec*[12].

$$\alpha_c = \frac{\omega^2 \eta}{2\rho_0 c^3}\left(\frac{4}{3} + \frac{(\gamma - 1)}{\Pr}\right) \tag{4.9}$$

In Eq. (4.9) η is the coefficient of shear viscosity in *Pa s*, γ is the ratio of specific heats, and Pr is the Prandtl number[12].

The absorption due to thermal and viscous wall losses are accounted for by using the absorption coefficient for wall losses. The absorption coefficient for wall losses is shown in Eq. (4.10)[12,33]. In Eq. (4.10), *a* is the radius of the waveguide.

$$\alpha_w = \frac{1}{ac}\left(\frac{\eta\omega}{2\rho_o}\right)^{\frac{1}{2}}\left(1+\frac{\gamma-1}{\sqrt{P_r}}\right) \tag{4.10}$$

The total thermoviscous absorption coefficient is the sum of the classical absorption coefficient and the absorption coefficient for wall losses. Eq. (4.11) shows the total thermoviscous absorption coefficient[14].

$$\alpha_p = \alpha_c + \alpha_w \tag{4.11}$$

The lossy acoustic wave number is shown in Eq. (4.12), where *k* is the lossless wave number and *j* is the $\sqrt{-1}$.

$$\widetilde{k} = k - j\alpha_p \tag{4.12}$$

The lossy wave speed is calculated using the lossy wave number as shown in Eq. (4.13). These losses assume that the fluid boundary layer is much smaller than the radius of the waveguide, and the wall of the waveguide is acoustically rigid[12].

$$\tilde{c} = \frac{\omega}{\tilde{k}} \tag{4.13}$$

4.2.5 Full Calibrator Model

To increase the accuracy of the model the actual calibrator driver was modeled and included in the circuit. The driver model was used in place of the constant volume velocity source. The driver model combines the acoustic, electrical and mechanical element of the driver by converting the electrical, and mechanical components into the acoustic impedance domain. Figure 4–8 shows the entire driver circuit model with the driver components in original domains.

In the circuit of Figure 4–8, there are two acoustic elements, four electrical elements, and three mechanical elements. The acoustic elements Z_{rad} and Z_{cal} represent the radiation impedance of the back of the driver, and the acoustic impedance of all of the calibrator waveguides respectively. The electrical circuit models the voice coil's electrical behavior, called motor impedance, as a series resistance (R_e), a series lossless inductance (L_1), and a series lossy inductance ($L_2||R_2$)[34]. The electrical circuit shows a source ($\hat{e}_g$) which is the complex voltage at the loudspeaker leads. The mechanical circuit models the mechanical suspension of the driver. The mechanical circuit consists of three elements, the mechanical resistance of the suspension (R_{ms}), the mechanical compliance of the suspension (C_{ms}), and the actual moving mass of the suspension (M_{ms}). The mechanical resistance of the suspension R_{ms} and the moving mass of the driver diaphragm (M_{md}) are calculated using Eq. (4.14) and Eq. (4.15), respectively.

$$M_{md} = M_{ms} - \frac{8}{3}\rho_o a^3 \tag{4.14}$$

$$R_{ms} = \frac{1}{2\pi F_s C_{ms} Q_{ms}} \tag{4.15}$$

In Eq. (4.14) a is the radius of the driver. In Eq. (4.15) F_s is the “free air” resonance frequency of the driver, and Q_{ms} is the quality factor of the driver at F_s considering mechanical losses of the moving system only[14].

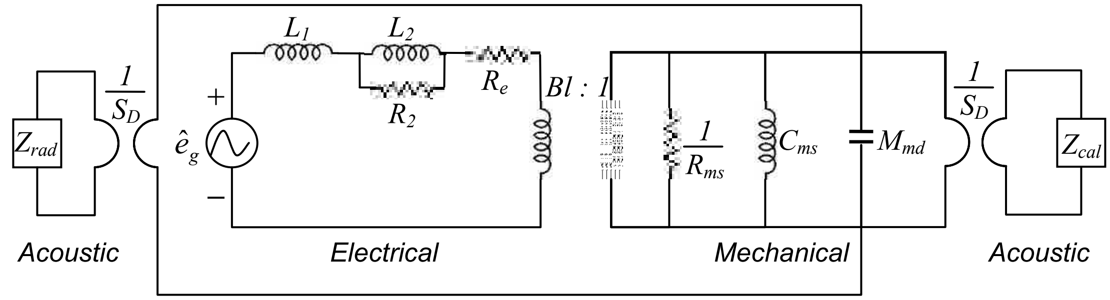

Figure 4–8: Driver circuit model in mechanical, electrical, and acoustic domains

The desired domain is the acoustic impedance domain. In Figure 4–8, a gyrator is used to connect the acoustic domain elements of the circuit to the mechanical domain elements. A transformer is used to connect the electrical domain elements to the mechanical domain elements. The gyration element uses the effective cross-sectional area of the driver diaphragm (S_D), and the transformation element uses the driver's transduction constant (Bl) to make the transformations[14, 34].

The circuit in Figure 4–8 can be simplified by computing an equivalent impedance of the electrical circuit. Equation (4.16) shows the equivalent acoustic impedance of the electrical circuit (Z_E).

$$Z_E = R_e + j\omega L_1 + \frac{j\omega L_2 R_2}{R_2 + j\omega L_2} \tag{4.16}$$

Using Eq. (4.16) and pulling the electrical elements through the transformer, and the acoustic radiation impedance of the driver Z_{rad} through the gyrator the circuit simplifies to the circuit shown in Figure 4–9[27]. The elements on the left side in Figure 4–9 are all in the mechanical domain. The potential source in the electrical circuit in Figure 4–8 is now a current source in the mechanical circuit in Figure 4–9. The final transformation is to pull the mechanical circuit elements in Figure 4–9 through the gyrator. This transformation provides an entire circuit model of the calibrator driver in the acoustic domain.

The results of the transformation are shown in Figure 4–10. The source element is again a potential source in the acoustic domain, and the entire driver model is in the acoustic domain. In the circuit in Figure 4–10 the driver radiation impedance, the driver electrical elements, and the driver mechanical elements all combine to replace the source element in Figure 4–5.

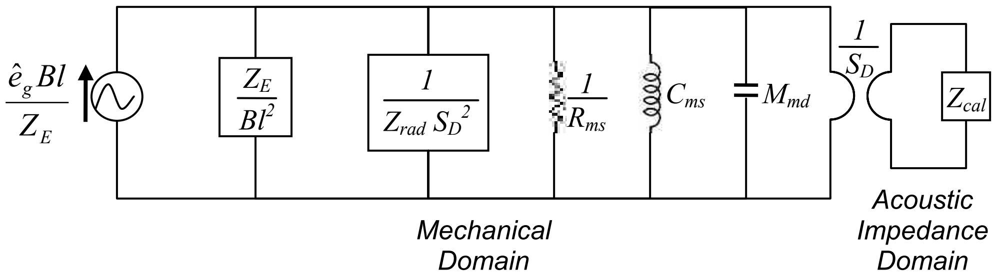

Figure 4–9: Driver circuit model in mechanical and Acoustic domains

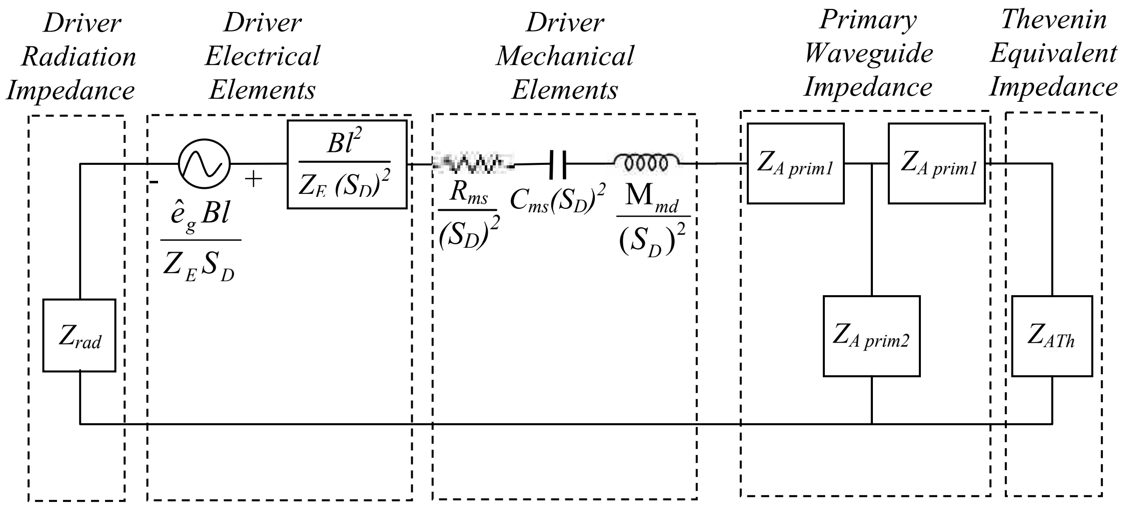

Figure 4–10: The entire calibrator circuit model in the acoustic domain

4.2.6 Measured Driver Parameters

The driver parameters used to model the driver were measured using the actual calibrator driver. The driver was suspended in an anechoic environment. Using a maximum-length sequence system analyzer (MLSSA) with the speaker parameter option (SPO) the driver element values were measured[34]. The MLSSA SPO determines the driver parameters by analyzing the complex impedance of the driver over the frequency range of interest. All of the complex impedance points are used in the analysis of the driver parameters. Driver impedance is complex and can be thought of as a curve in 3D space where the x-axis is the real part of the impedance, the y-axis is the imaginary part and the z-axis is the frequency[34]. The measured parameters are valid to use in the model because the MLSSA accounts for the real, imaginary, and frequency dependence of each driver parameter.

The parameters were measured ten different times and the average of all ten runs for each parameter was used in the model. The added-mass method was used to measure the parameters[34]. The first five parameter measurements were made using an added mass of 1 gram and the second five were made using 2 grams. The averaged results of all of the parameters used in the model are shown in Table 4–1.

Table 4–1: Measured loudspeaker parameters used in circuit model

Parameter	Mean	Stdev	Units
Effective Driver Diameter (Sd)	1.30E-03	N/A	m2
Free-Air Resonance (Fs)	268.034	1.066325	Hz
Qms	6.5686	0.057918	
Mechanical Mass (Mms)	0.0021454	6.15E-05	kg
Mechanical Compliance (Cms)	0.0001645	5.64E-06	m/N
Bl	2.7247	0.041639	Tesla-m
Electrical Resistance (Re)	6.2489	0.002025	Ohms
L1	0.0000892	4.22E-07	Henry
L2	0.00013	1.71E-12	Henry
R2	7.4425	0.019851	Ohms

4.2.7 Radiation Impedance

To evaluate the circuit shown in Figure 4–10 the radiation impedance of the driver must be determined. In the model, the radiation impedance is the acoustic radiation impedance of the backside of the driver. For simplicity, the backside of the driver was assumed to have the same radiation impedance as a baffled piston open to the atmosphere. The acoustic radiation impedance of a circular piston in an infinite baffle is[26]

$$Z_{rad} = \frac{\rho_o c}{S}\left[R_1(2ka) - jX_1(2ka)\right] \qquad \textbf{(4.17)}$$

Where

$$R_1(2ka) = 1 - \frac{2J_1(2ka)}{2ka} \qquad \textbf{(4.18)}$$

and

$$X_1(2ka) = \frac{2\mathrm{H}_1(2ka)}{2ka} \qquad \textbf{(4.19)}$$

In Eqs. (4.17) – (4.19) a is the driver radius, ρ_o is the density of air, c is the wave speed, k is the wave number ω/c, S is the cross-sectional area of the driver, J_1 is the Bessel function of the first kind, and H_1 is the Struve function of the first kind[35]. The Bessel function was calculated using the built in function in MATLAB. No such function exists for the Struve function. The Struve Function was approximated using Eq. (4.20)[35].

In Eq. (4.20) J_0 is the Bessel function of order zero, and η is the argument of the function. In the case of the baffled piston $\eta = 2ka$. The approximation in Eq. (4.20) is valid for all values of *ka*. Another approximation valid for $ka \ll 1$ is shown in Eq. (4.21), and the asymptotic expression valid for $ka \gg 1$ or as $\eta \to \infty$ is shown in Eq. (4.22) can be also used[26,35].

$$\mathrm{H}_1(\eta) \approx \frac{2}{\pi} - J_0(\eta) + \left(\frac{16}{\pi} - 5\right)\frac{\sin(\eta)}{\eta} + \left(12 - \frac{36}{\pi}\right)\frac{1-\cos(\eta)}{\eta^2} \qquad \textbf{(4.20)}$$

$$\mathrm{H}_1(\eta) = \frac{2}{\pi}\left(\frac{\eta^2}{1^2 3} - \frac{\eta^4}{1^2 3^2 5} + \frac{\eta^6}{1^2 3^2 5^2 7} - \cdots\right) \qquad \textbf{(4.21)}$$

$$\mathrm{H}_1(\eta) \to \frac{2}{\pi} + \sqrt{\frac{2}{\pi\eta}}\sin\left(\eta - \frac{3\pi}{4}\right) \qquad \textbf{(4.22)}$$

The approximations in Eq. (4.21) and Eq. (4.22) present an undesired discontinuity when $ka \approx 1$. This discontinuity occurs for this driver at about 1330 Hz. The approximation in Eq. (4.20) was used in the model.

The three approximations were plotted to illustrate the continuity of the approximation shown in Eq. (4.20) compared to the discontinuities in the approximations in Eq. (4.21) and Eq. (4.22). Figure 4–11 compares the approximation valid for all *ka* calculated using Eq. (4.20) to the small and large *ka* approximations calculated in Eq. (4.21) and Eq. (4.22) respectively.

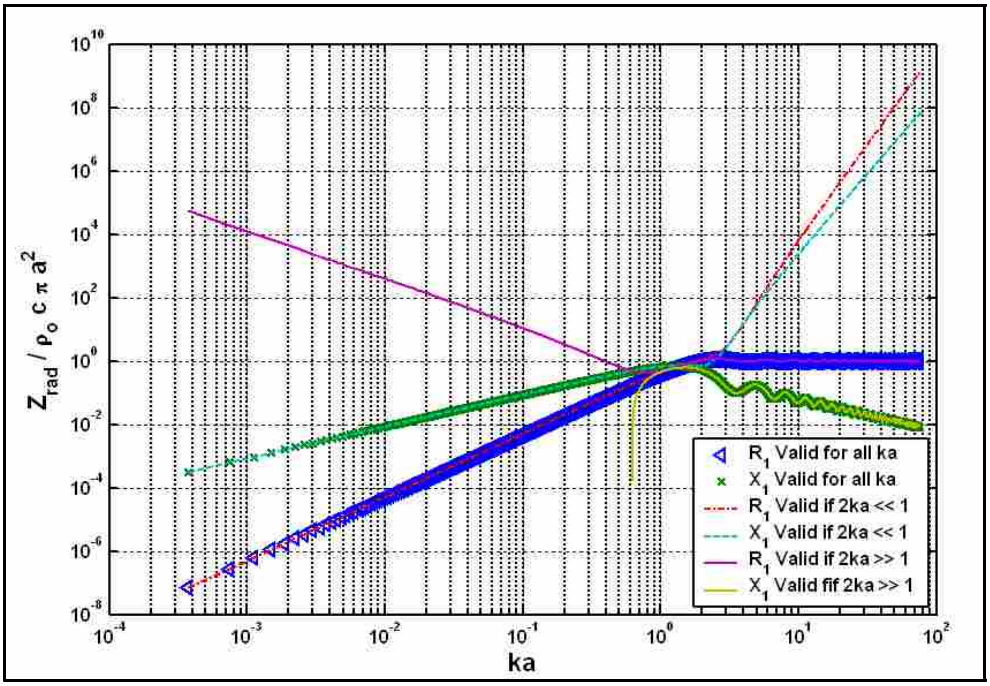

Figure 4–11: Struve function approximations

4.3 MODEL RESULTS

The three model stages were evaluated numerically using MATLAB. All three stages used the assumption that the microphone terminations provided infinite acoustic impedance. The waveguide walls were assumed acoustically rigid. The model results of each stage were compared to actual measured results.

4.3.1 Idealized Model Results

The idealized model assumed the source to be a constant volume velocity source and the tubes to be lossless. The idealized model results and the measured results are shown in Figure 4–12. The model accurately predicts the frequency of the calibrator resonances. As expected the amplitude of the model resonances are high. These large resonances spikes are a result of the lossless assumption used in the ideal model.

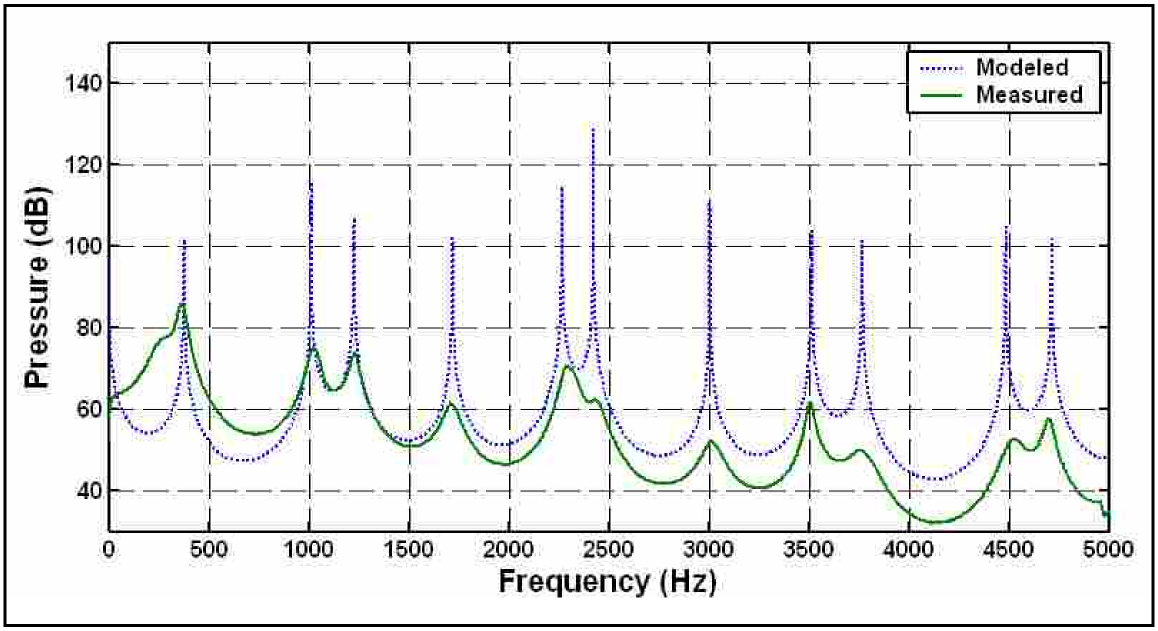

Figure 4–12: Ideal model results compared to actual measured results

4.3.2 Lossy Model Results

The model was reevaluated using the lossy wave number of Eq. (4.12) and the lossy wave speed of Eq. (4.13) in the waveguide impedances of Eq. (4.1) and Eq. (4.2) for all of the calibrator waveguides. The results of the lossy model were compared to the measured results and are shown in Figure 4–13. In Figure 4–13 the model resonances more accurately predict the actual measured response. The addition of the thermoviscous losses clearly improves the accuracy of the model. The lowest calibrator frequency is suspected to be influenced by the driver. The model of the lowest resonance poorly predicts the actual measured response of the first resonance. It will be shown in the next section that modeling the actual driver will improve the shape of the lowest resonance. It will also be shown that including the driver in the model increases the accuracy of all of the resonances.

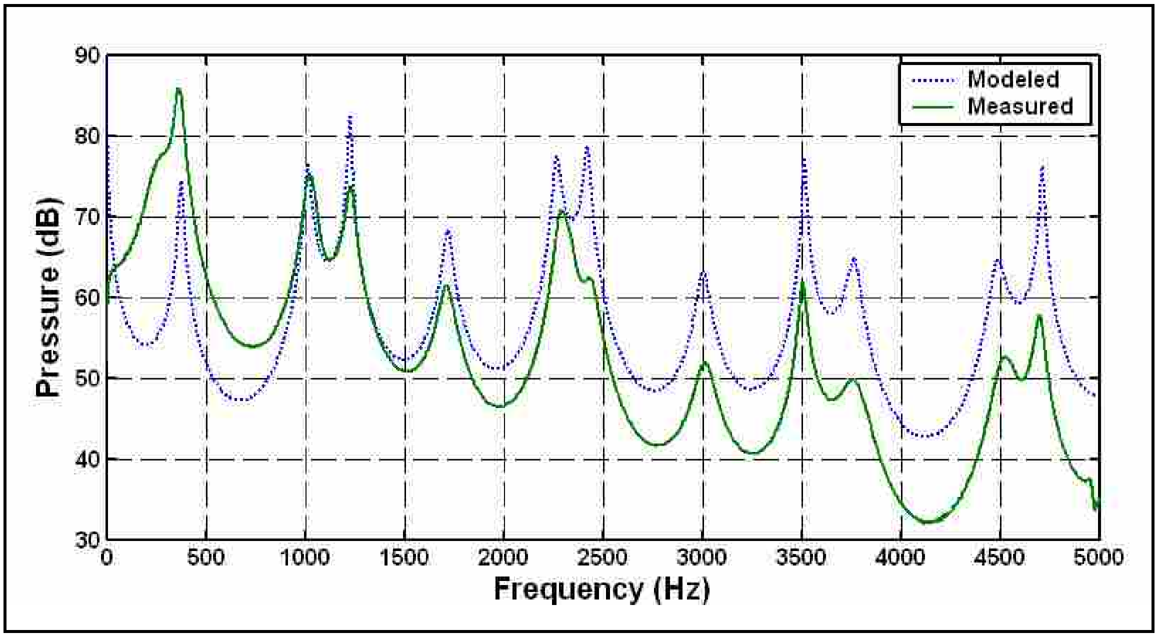

Figure 4–13: Lossy model results compared to actual measured results

4.3.3 Full Calibrator Model Results

The actual driver parameters were measured and included in the calibrator model to further improve the accuracy of the model. The rear of the driver was assumed to have the radiation impedance of a circular piston mounted in an infinite baffle. Including the actual driver parameters in the model clearly increases the accuracy of the model. Figure 4–14 shows the full calibrator model results. The lowest calibrator resonance is significantly improved from the lossy model. By inspection, it can be seen that the overall trend of the full calibrator model results more accurately predicts the measured response than the lossy model. It is evident that the drive has a significant affect on the frequency response of the calibrator.

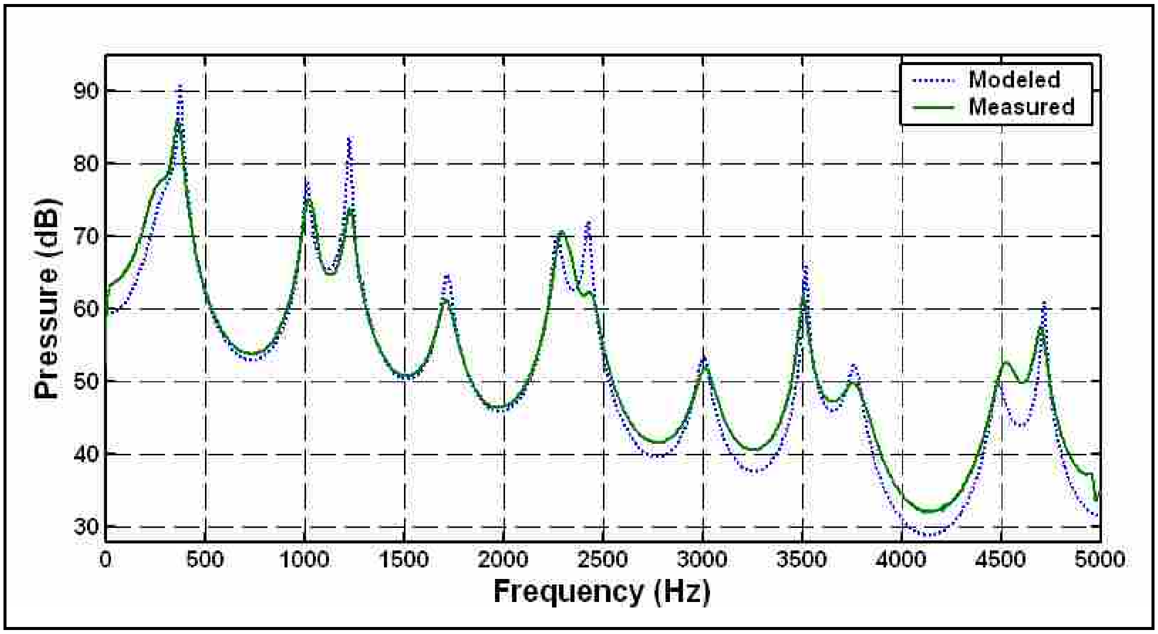

Figure 4–14: Full calibrator model results compared to actual measured results

4.3.4 Potential Model Improvements

The model results could be further improved by including in the model elements that account for errors induced by the assumptions used. Improvement to the model could be made with a more accurate method of modeling the losses. The model used assumes that the fluid boundary layer is small compared to the radius of the tube. The tubes used in the actual calibrator begin to violate this assumption. The calibrator consists of four different sized waveguides, the primary waveguide and the three-segment waveguides. The three-segment waveguides are the same for the five paths. By increasing the losses of the four different waveguides it was possible to increase the accuracy of the model. The losses were arbitrarily added to the numerical model and were adjusted by inspecting the effect of the losses on the plotted results with particular attention to the frequency of interest. Figure 4–15 shows the result of the additional losses. Further investigation is required to analytically verify the correct values of the additional losses.

The model could also be improved by measuring the acoustic impedance of the microphones at the termination of the paths. The microphones also introduce an additional length between the grid cap and the diaphragm of the microphone. The driver has a conical shaped diaphragm that also provides an additional length to the system. Accounting for these additional lengths would improve the model results. The walls of the waveguides were assumed acoustically rigid. Accounting for any error introduced by this assumption would improve the model. The radiation impedance of the rear of the driver was assumed to be the same as a circular piston mounted in an infinite baffle. A more accurate model would be a circular piston mounted in a sphere or a cylindrical tube. These models would be more accurate at low frequencies; however, the solutions converge at higher frequencies.

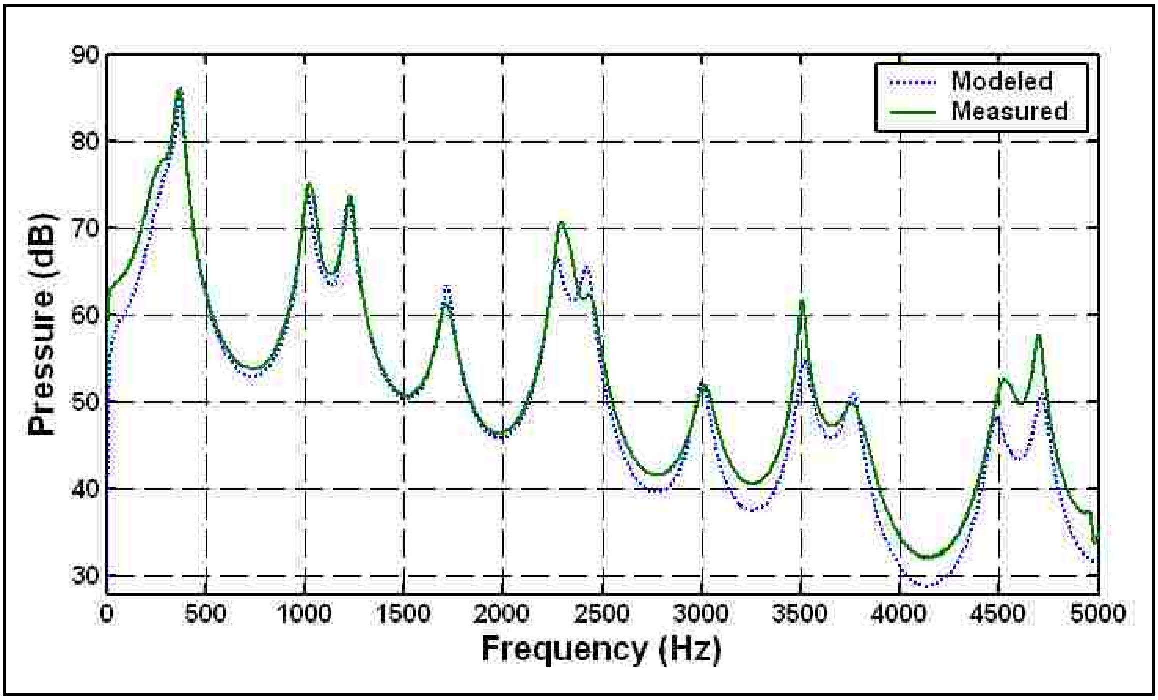

Figure 4–15: Increased losses model results

5 CALIBRATOR HARDWARE

This chapter discusses the components of the calibrator. Each component is described in detail both physically and acoustically. The design and manufacturing of each of the components is also presented. Computer aided drawing (CAD) models of each of the components are used to illustrate their physical interactions with mating parts. The CAD models also help to illustrate the acoustic connection between different components.

5.1 ENTIRE CALIBRATOR

A photograph shows the probe in the calibrator in Figure 5–1. A driver is used to excite the driver tube at all frequencies. Below the cutoff frequency of the first cross mode of the driver tube, only plane waves exist at the splitter. The plane waves allow the splitter to divide the volume velocity into five equal paths. The receiver tubes attach to the splitter, and guide the sound to the four probe microphones and the reference microphone. The bottom half of the calibrator clamp aligns the receiver tubes with probe microphones. The calibrator clamp surrounds the entire probe and provides a consistent seal at each microphone. The two halves of the calibrator clamp are connected with three latches. The individual components are described in detail in the following sections. Detailed dimensioned drawings of all of the calibrator components are shown in Appendix A.

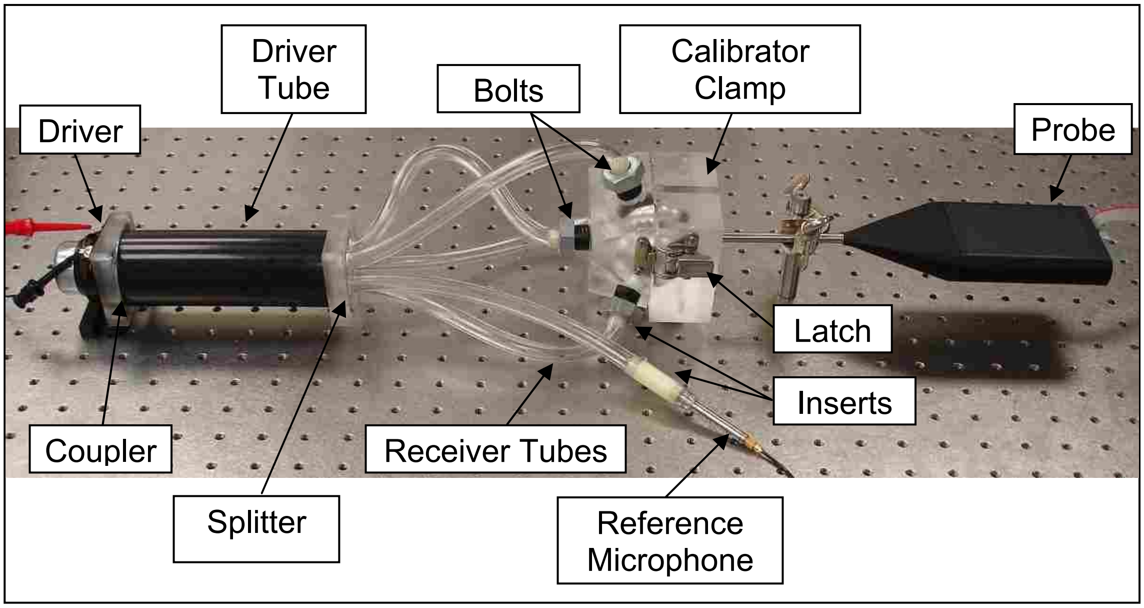

Figure 5–1: Entire calibrator

5.2 SOURCE

The calibrator source is a HiVi A2S full frequency loudspeaker shown in Figure 5–2. The driver dimensions in millimeters are illustrated in the appendix. The loudspeaker frequency response shown in Figure 5–3 is flat (no major resonances) over the frequency range for which the calibrator is designed to operate. This characteristic makes the driver useful in a frequency-band calibration application. The driver size is also of practical importance. The driver must be similar in diameter to the driver tube (discussed in next section).

Figure 5–4 a) shows the top view of the loudspeaker, and Figure 5–4 b) shows the bottom view. The top view of the driver shows the diaphragm, the surround, the seal and the flange. The flange is used to mount the driver to a structure using the four corner holes. The seal is located between the driver surround and the flange, and makes it possible to acoustically isolate the two side of the driver diaphragm. The bottom view shows the driver magnet and the electrical leads.

Figure 5–2: HiVi A2S full frequency loudspeaker

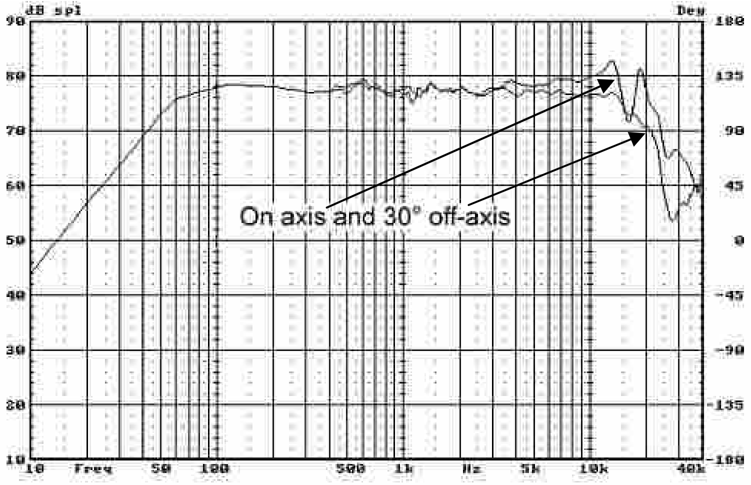

Figure 5–3: HiVi A2S frequency response

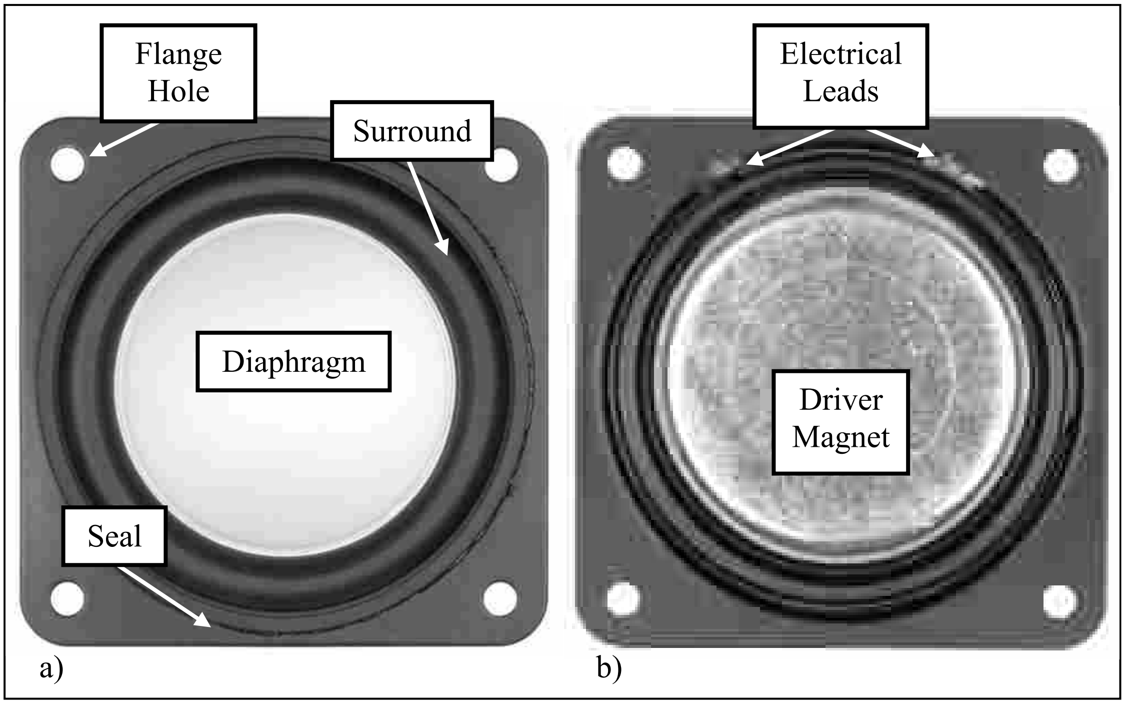

Figure 5–4: HiVi A2S a) top view b) bottom view

5.3 COUPLER

The coupler was designed to connect the driver to the driver tube. The coupler was machined out of clear acrylic glass. A CAD model of the coupler is shown in Figure 5–5. The large hole in the middle of the coupler is placed over the driver diaphragm. The diameter of the hole allows the coupler to rest on the seal without interfering with the driver surround. The outside dimensions were made the same size as the driver flange. The four small holes near each corner of the coupler were drilled and tapped. This allows screws to pass through the driver flange and screw into the coupler securely fastening the coupler to the driver. Figure 5–6 is a CAD model assembly of the driver mated with the coupler. As shown in Figure 5–6 the large coupler hole does not interfere with the driver surround. The coupler has no acoustic function.

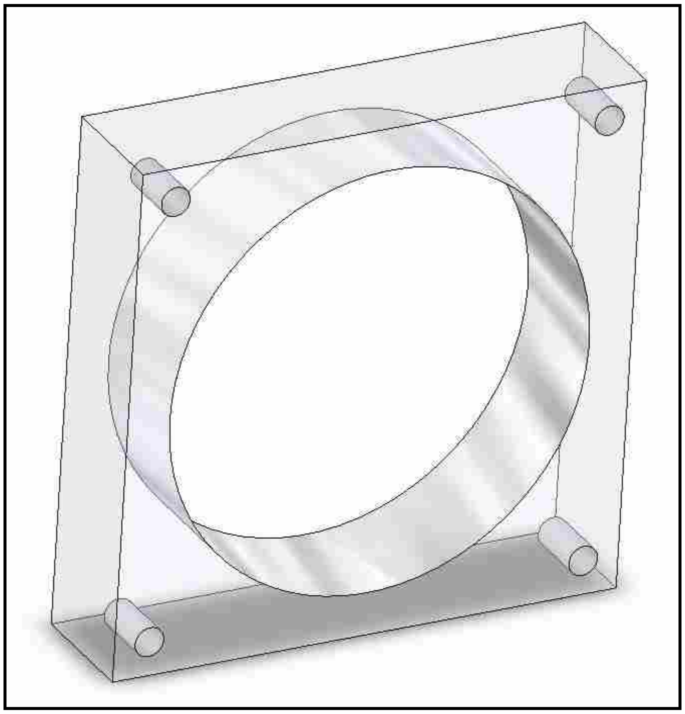

Figure 5–5: Coupler CAD model

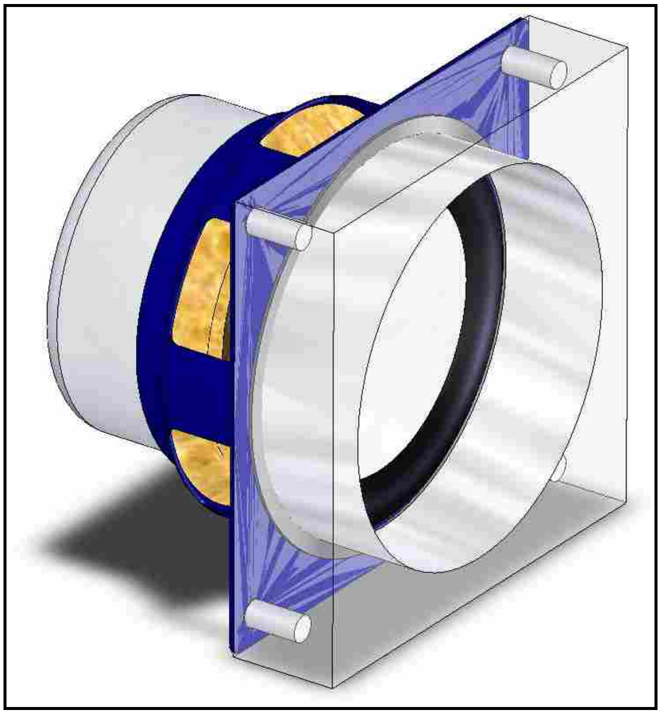

Figure 5–6: Driver coupler CAD assembly model

5.4 DRIVER TUBE

The driver tube was designed to separate the source from the splitter. As discussed in Section 3.2, a waveguide can remove higher order modes that are induced by a source. The driver tube was chosen to be a circular waveguide with a radius of 0.02 m and length of 0.145 m. A CAD model of the driver tube is shown in Figure 5–7. The driver tube is the primary waveguide in the circuit models in Chapter 4.

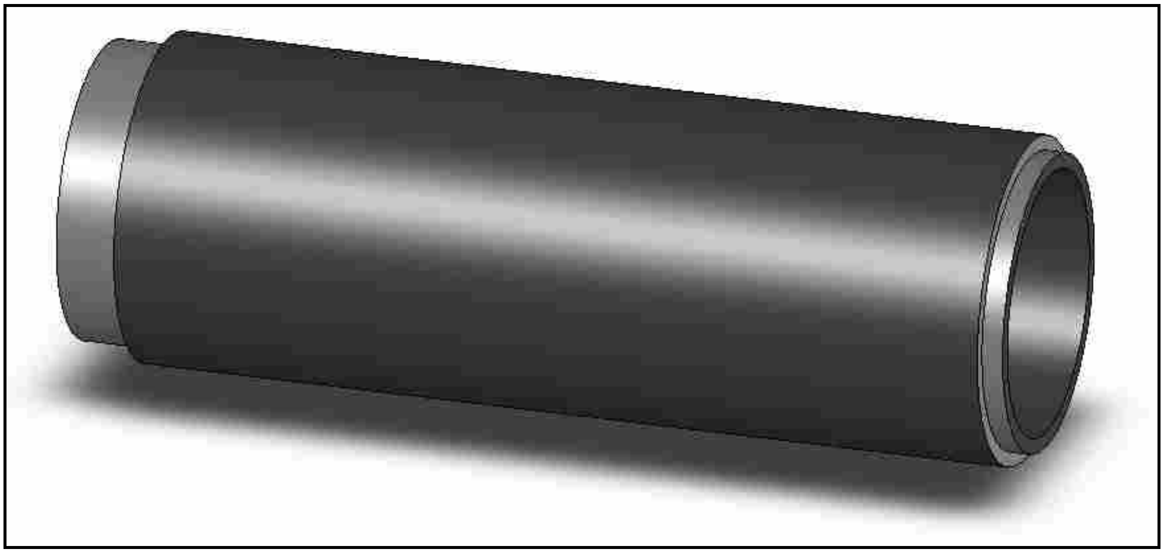

Figure 5–7: Drive tube CAD model

This radius was designed be large enough to cover the driver diaphragm and be able to be divided into five parts. The driver tube must also be small enough to keep the cutoff frequency of the first cross mode above the operational limit of the calibrator. The resulting f_c of the first higher order mode of the driver tube is 5000 Hz.

The length was calculated by solving for z_2 in Eq. (3.17). The length was designed to attenuate the first higher order mode by more than 90 dB when the driver tube is driven at 3000 Hz, or more than 105 dB of attenuation when the tube is driven at 2000 Hz (the probe upper frequency limit). All other higher order modes would attenuate before the first one (see Eq. (3.17)). If all of the higher order modes have attenuated, only plane waves exist in the tube. With only plane waves propagating in the driver tube, the pressure is the same at the entrance to each of the individual receiver tubes.

The driver tube was manufactured using a piece of black PVC tube. Both ends of the tube were machined to allow them to connect to the coupler and the splitter. Figure 5–7 illustrates these two diameter changes. The left end of the driver tube shown in Figure 5–7 connects to the coupler described in Section 5.3. The right end of the tube shown in Figure 5–7 connects to the splitter described in Section 5.5.

Figure 5–8 is a CAD model assembly showing the driver, the coupler and the driver tube. The model is sectioned to show how the coupler and the driver tube interface. The driver tube is inserted into the coupler. The driver tube was designed to avoid interfering with the driver surround. Figure 5–8 illustrates how the coupler and the driver tube connect without interfering with the driver surround. The driver tube is not fastened to the coupler in any way. The driver tube fits inside the coupler in such a way that it can be removed, but the interface between the two components is tight. The coupler and driver tube models are complete models. The CAD model of the driver is not a complete model. In this assembly, the driver does not represent the interior of the actual driver. The model of the driver shown in Figure 5–8 was made to superficially resemble the actual driver. The purpose of the driver model shown in Figure 5–8 is to illustrate the interface between the coupler and the driver tube relative to the driver surround.

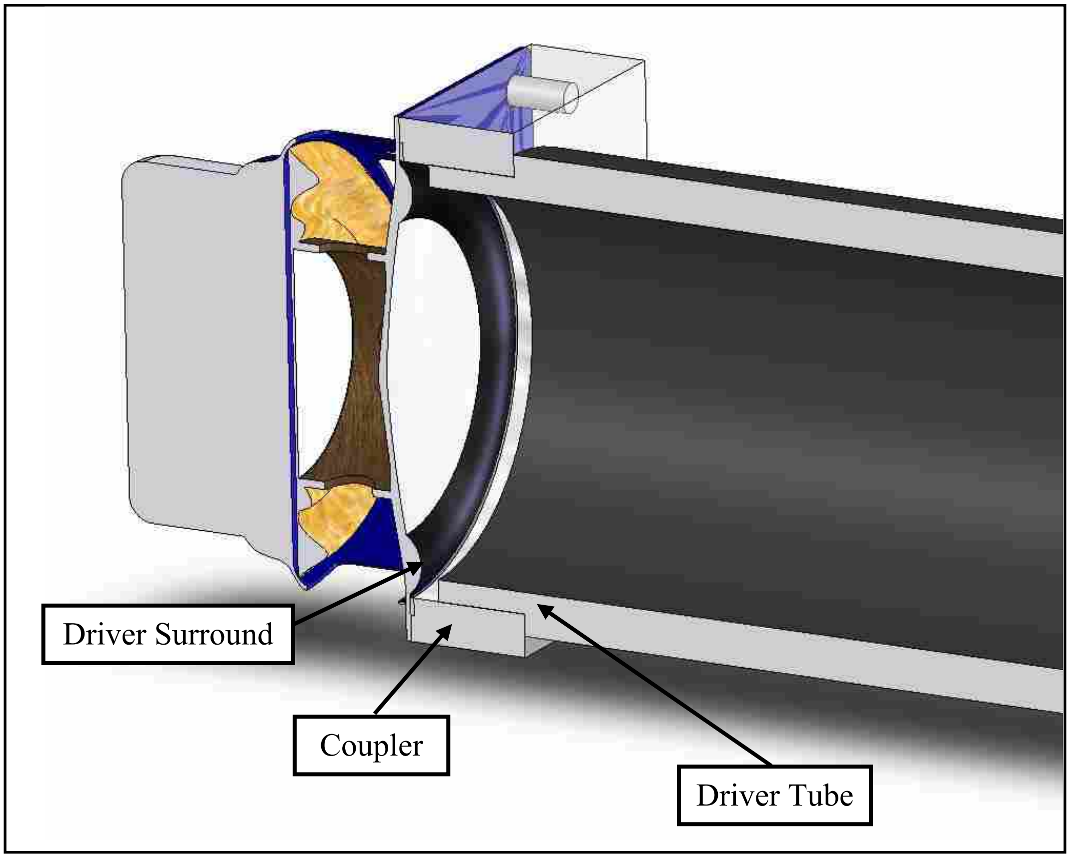

Figure 5–8: Driver, coupler and driver tube assembly

5.5 SPLITTER

The splitter was designed and built to divide the volume velocity into equal separate paths as illustrated in Figure 3–1. The splitter is equipped with five holes (one for each microphone on the probe and one for a reference microphone). The holes are located symmetrically about the center of the splitter as shown in Figure 5–9 a). Each hole is equipped with a port that is designed to connect to a receiver tube. Figure 5–9 b) illustrates the driver tube splitter interface. These holes are the first waveguide in the path circuit used in the models in Chapter 4. The driver tube interface is where the driver tube connects to the splitter. The driver tube connection to the splitter is similar to the connection to the coupler. The port side of the splitter as shown in Figure 5–9 a) illustrates the ports around the holes designed to attach the individual receiver tubes.

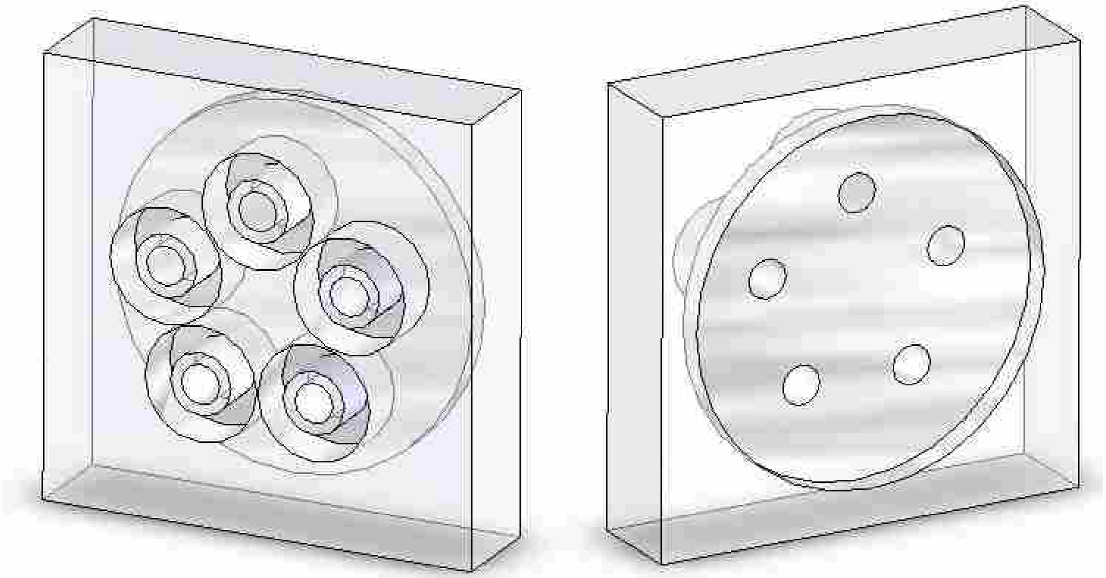
a) Receiver tube ports

b) Driver tube interface

Figure 5–9: Splitter

The splitter was manufactured using clear acrylic glass. The splitter has the same outside dimensions as the coupler. The large circular cutout in the splitter illustrated in Figure 5–9 b) has the same diameter as the large through hole of the coupler illustrated in Figure 5–6. The splitter is connected to the driver tube in the same manner as the coupler. Figure 5–10 is a CAD assembly drawing of the splitter mounted on the end of the driver tube, with the coupler and the driver on the opposite end. Figure 5–10 illustrates the relative size of the splitter to the driver tube and the coupler.

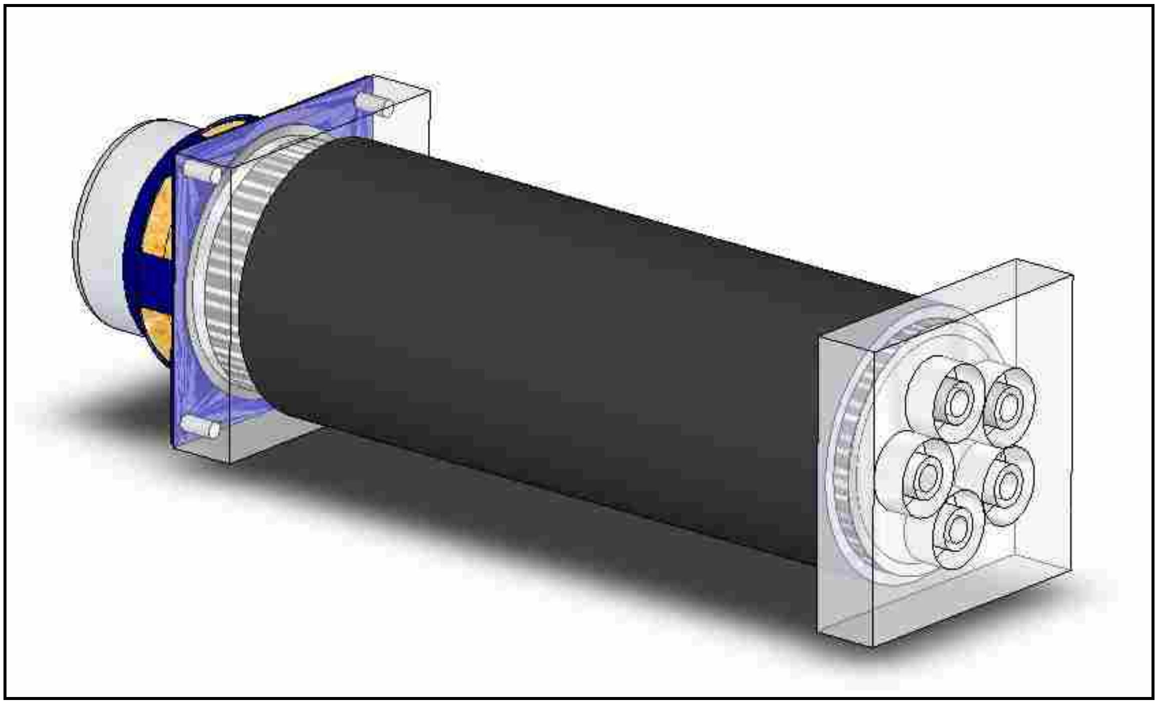

Figure 5–10: CAD assembly drawing of the splitter mounted on the driver tube opposite the driver and coupler

A sectioned view of the assembly in Figure 5–10 is shown in Figure 5–11. The sectioned view illustrates how the splitter is connected to the driver tube. This view also allows one to visualize where the sound travels from the driver tube to the splitter. Figure 5–11 illustrates the diameter discontinuity between the driver tube and the splitter. This diameter discontinuity is the cause of the added acoustic inductance in the circuit models of Chapter 3. Recall from Chapter 3, the change in diameter can be thought of physically as an added length.

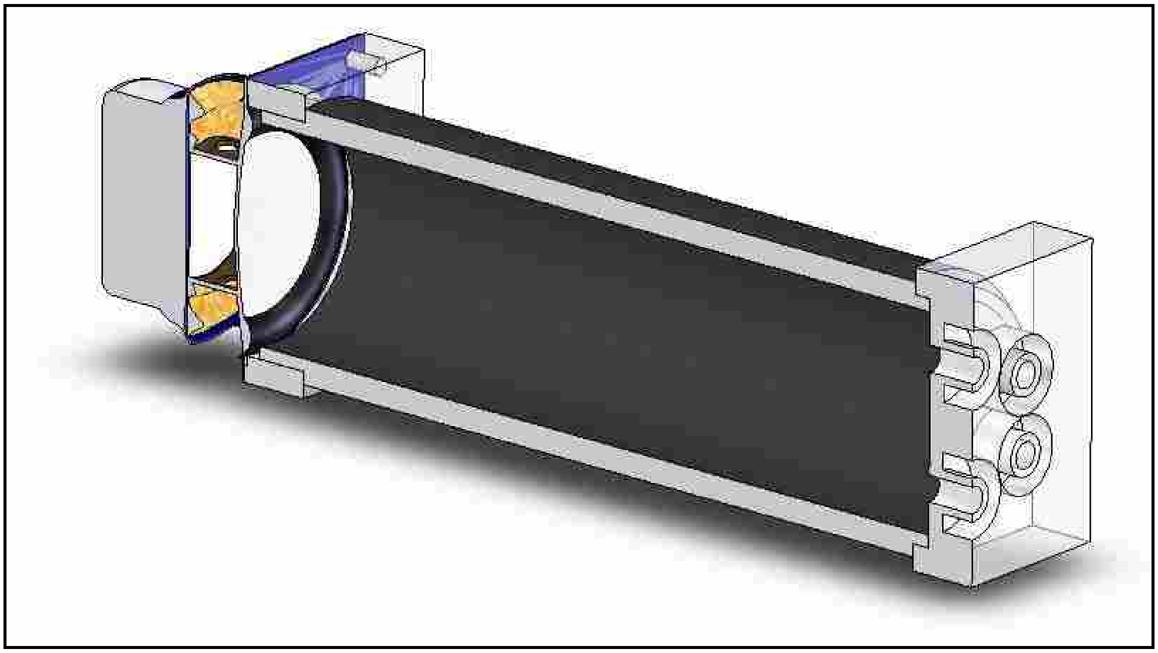

Figure 5–11: Section view of the CAD assembly drawing of the splitter mounted on the driver tube opposite the driver and coupler

5.6 RECEIVER TUBES

Flexible PVC tubes with an outside diameter of 0.0119 m were added to the end of each port of the splitter. The receiver tubes were chosen to have an inside diameter of 0.00635 m. The receiver tubes are 0.203 m long, and the acoustic path is 0.188 m long. The receiver tubes need to be this length to allow all receiver tubes to reach a microphone without a kink. A kink in the receiver tubes would cause a change in the cross section of the tube and cause the kinked receiver tube to differ from the remaining four. A CAD model of one of the receiver tubes is shown in Figure 5–12 .

The receiver tubes connect to the ports on the splitter at one end and the inserts at the other end. The connections are an interference fit meaning the tube is stretched over the port, and the elastic properties of the tube hold it in place. The receiver tube is 0.203

m long, and when connected to the splitter on one end, and the insert on the other end the acoustic path is shortened to 0.188 m.

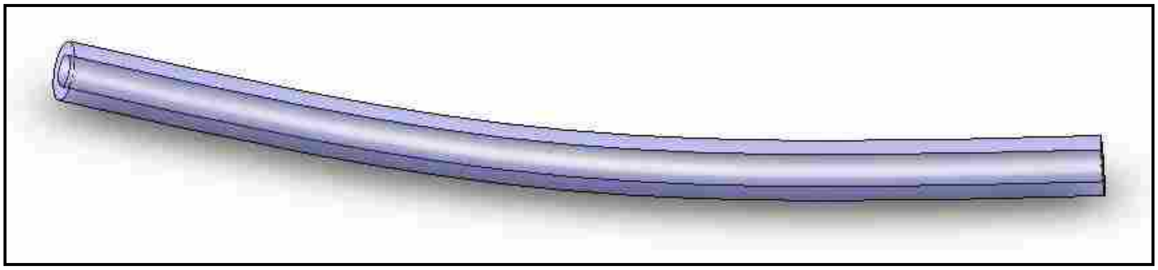

Figure 5–12: Receiver tube CAD model

The five receiver tubes are identical in length and diameter. The physical similarities are essential to ensure the acoustic path is the same for each. The receiver tubes needed to be flexible to allow them to have the same length and reach all of the microphones as shown in Figure 5–1.

Figure 5–13 is a CAD model assembly showing all five of the receiver tubes connected to the splitter. The receiver tubes are flexible and are unrestrained at the open end. The receiver tube orientations were arbitrarily chosen for this illustration. A sectioned view of the assembly shown in Figure 5–13 is illustrated in Figure 5–14. The sectioned view allows the reader to visualize where the sound travels as it propagates from the source on the left to the end of the receiver tubes on the right. After the splitter divides the volume velocity, it must pass through another diameter discontinuity. This discontinuity occurs because the splitter port diameter is smaller than the receiver tube diameter. Figure 5–15 is a closer look at the discontinuity between the splitter and the receiver tubes. Figure 5–15 also illustrates the interference connection between the receiver tubes and the splitter ports.

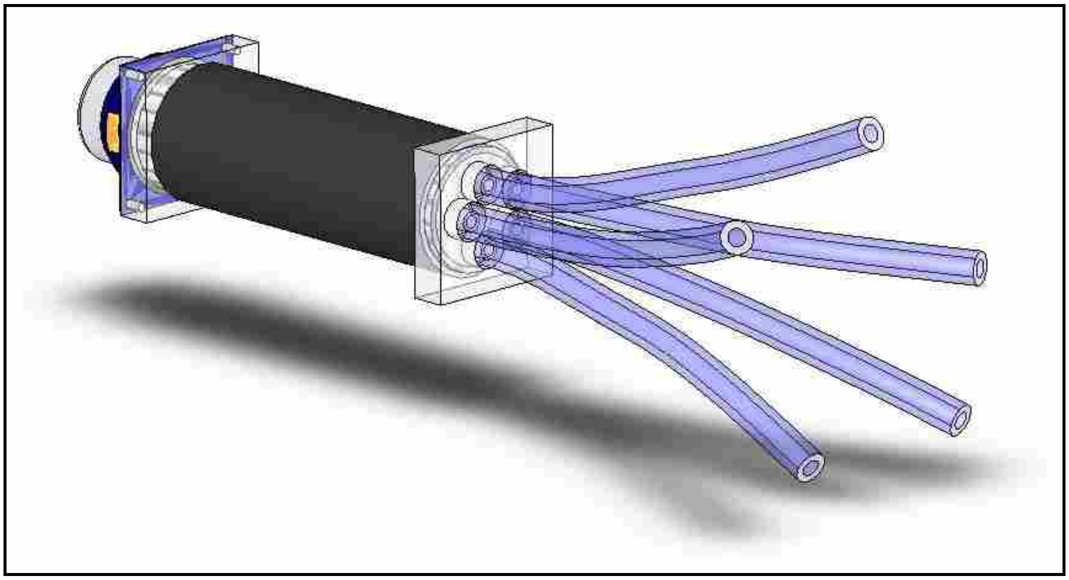

Figure 5–13: CAD assembly model with the receiver tubes connected to the splitter

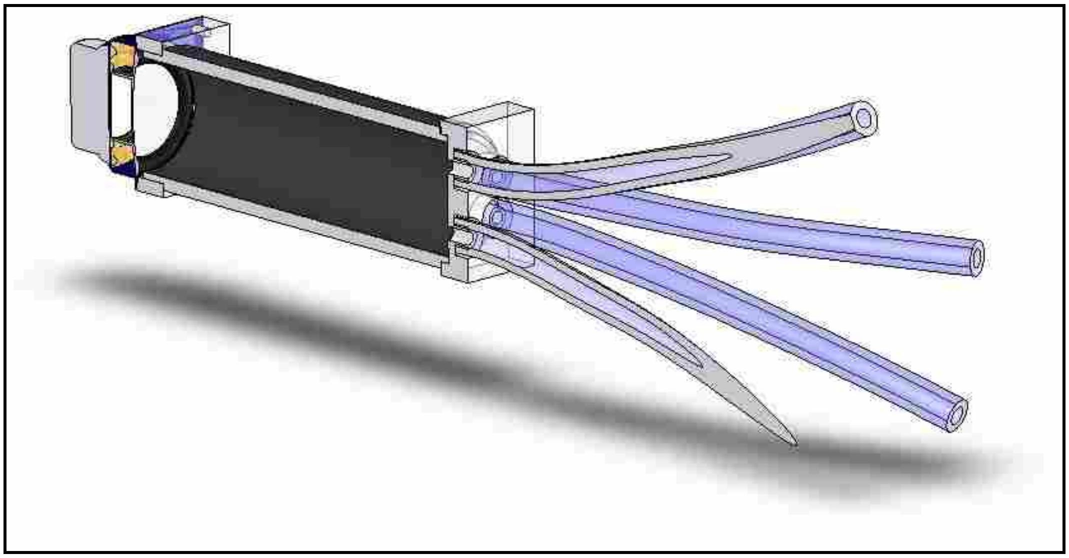

Figure 5–14: Sectional view of CAD assembly model with the receiver tubes connected to the splitter

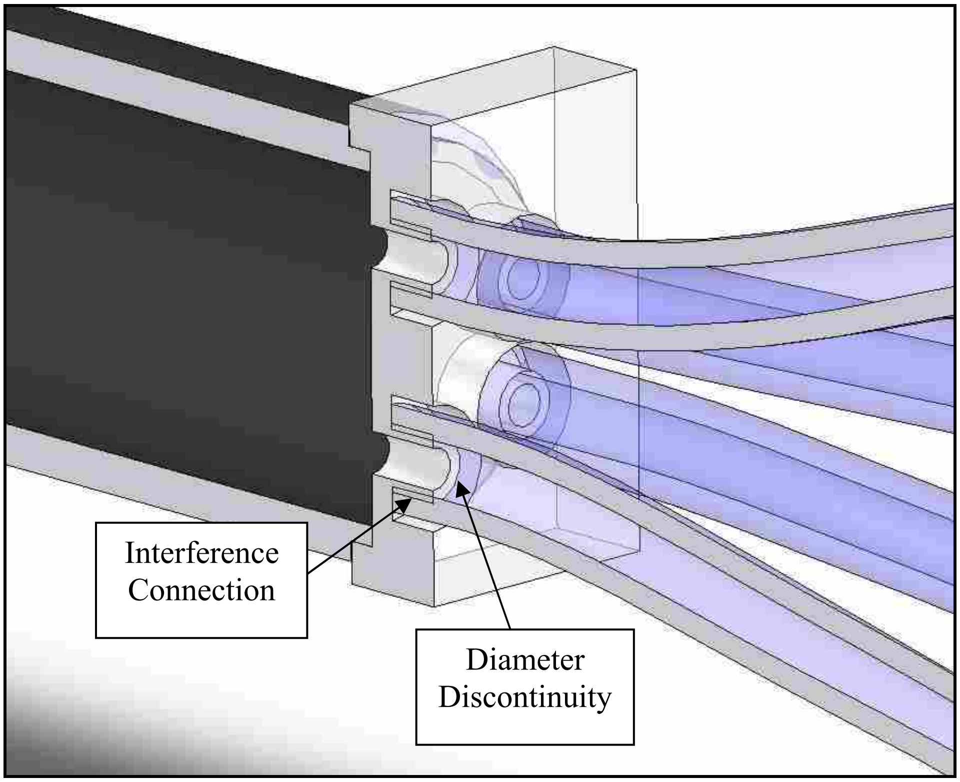

Figure 5–15: Receiver tube, splitter connection

5.7 CALIBRATOR CLAMP

The calibrator clamp aligns the end of each receiver tube with a probe microphone. The calibrator clamp was designed using two halves with spherical cavities that come together and enclose the probe as shown in Figure 5–16. The top half of the calibrator clamp is equipped with a groove that allows the probe shaft to pass through to its center.

The bottom half of the calibrator clamp is where the probe microphones are met. This half of the calibrator clamp is equipped with a notch that aligns with the top half. The bottom is also equipped with four ports. Each port lines up with a microphone on the probe.

In Figure 5–16, the calibrator clamp function is illustrated from left to right. On the left side of Figure 5–16, the top half of the calibrator clamp is shown around the probe shaft. In the center of Figure 5–16, the bottom half of the calibrator clamp is shown aligned with the four microphone ports. On the right side of Figure 5–16, the two halves are together and surrounding the probe. The two halves are held together using three latches. The latches are not shown in the CAD model. One of the latches is illustrated in the photograph of the entire calibrator presented in Section 5.1.

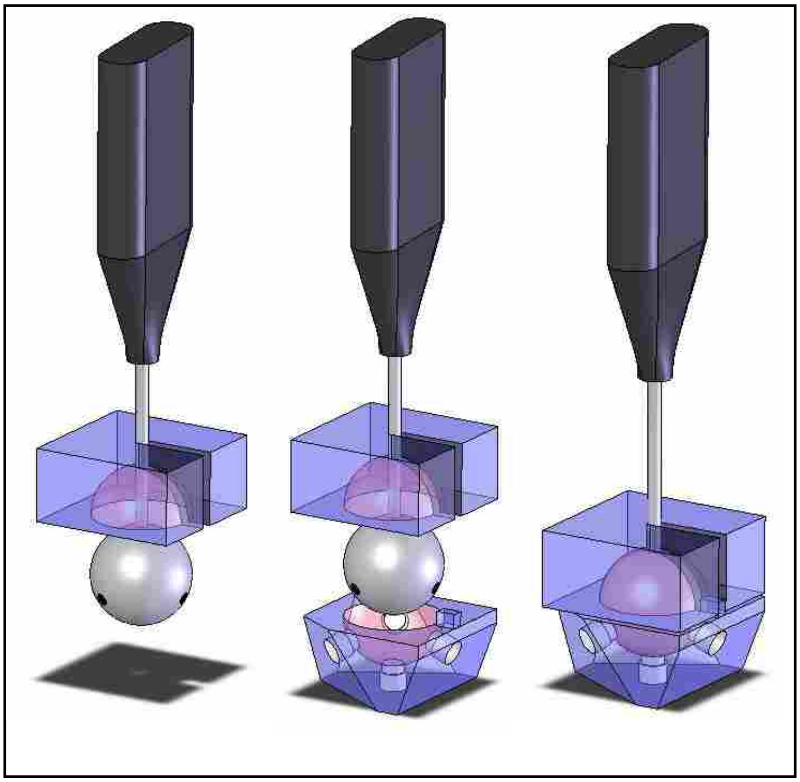

Figure 5–16: Calibrator clamp

5.7.1 Top Half of Calibrator Clamp

A CAD model of the top half of the calibrator clamp is shown in Figure 5–17. Figure 5–17 illustrates the groove that allows the probe shaft to pass through to the center. A view of the inside of the spherical cavity is shown on the left in Figure 5–17. The right side of Figure 5–17 shows the outside of the top half of the clamp.

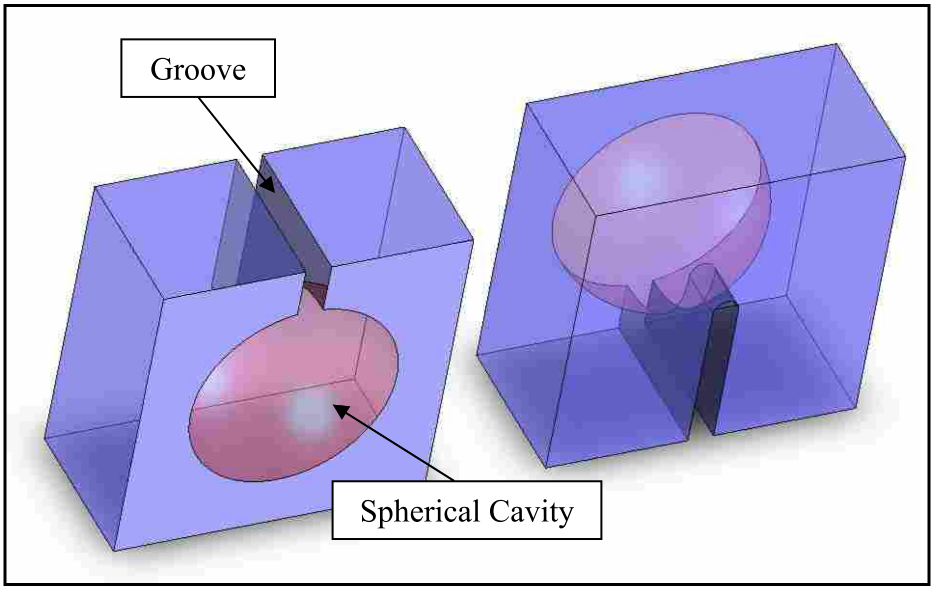

Figure 5–17: Top half of the calibrator clamp

5.7.2 Bottom Half of Calibrator Clamp

The bottom half of the calibrator clamp is shown in Figure 5–18. The left side of Figure 5–18 illustrates the inside of the spherical cavity and the notch used to align the two halves. The notch mates with the groove as shown in Figure 5–16. The right side of Figure 5–18 illustrates the outside of the bottom half with the four microphone ports.

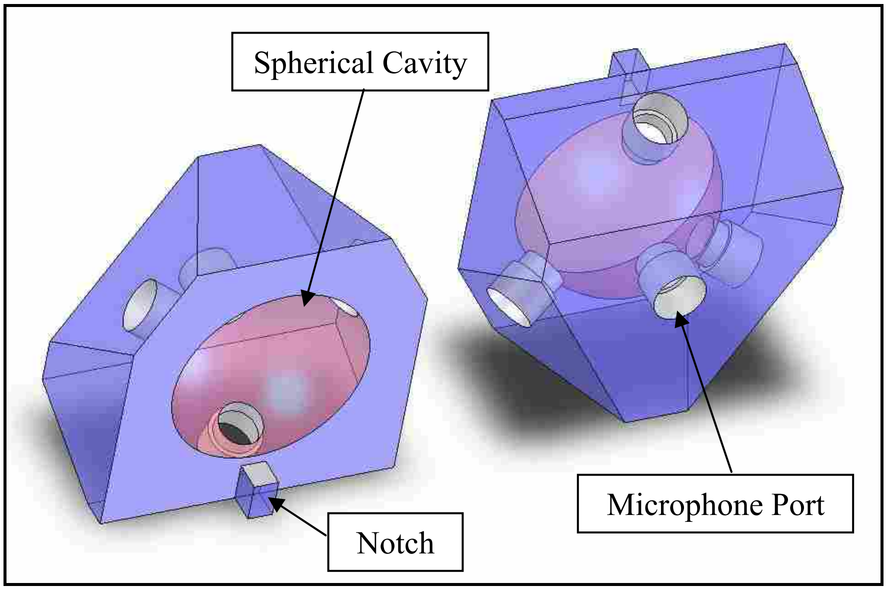

Figure 5–18: Bottom half of the calibrator clamp

5.7.3 Microphone Ports

Each microphone port has an insert that is fit with an o-ring to seal where the probe interfaces with the bottom half of the calibrator clamp. The o-ring has an inside diameter of 0.00632 m and an outside diameter of 0.010 m. The o-ring forms a seal around the microphone. The inserts are connected to the receiver tubes. The inserts are the third and final waveguide in each of the five acoustic paths. The inserts are held in place by a bolt that has a hole in the center to allow the insert to pass through it. The bolts screw into threaded holes in the bottom half of the calibrator clamp. The inserts were machined out of PVC, the bolts are stock items that were modified, both the bolts, and the o-rings were purchased.

The two halves of the calibrator clamp and the components of one of the microphone ports are illustrated in a CAD assembly model exploded view shown in

Figure 5–19. In Figure 5–19 the components are illustrated relative to the probe. A close up view of the microphone port exploded view is shown in Figure 5–20. Figure 5–20 illustrates the individual microphone port components. Figure 5–20 also illustrates how the insert passes through the bolt, and is held in place by the bolt as the bolt is screwed into the bottom half of the calibrator clamp.

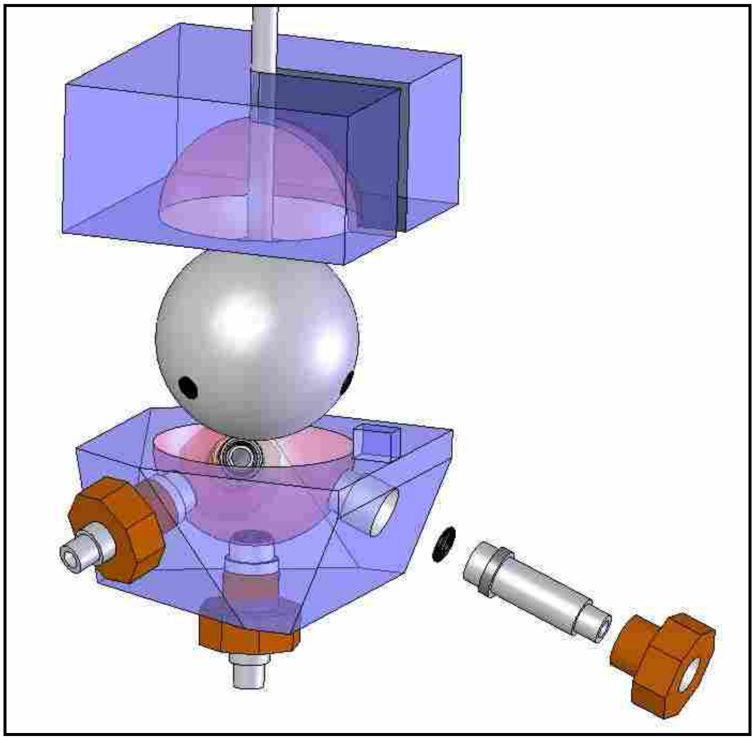

Figure 5–19: Microphone port exploded view

The inserts have an acoustic effect on the calibrator frequency response. The inserts are necessary to align the receiver tubes with the microphones. The only function of the bolt is to physically hold the insert tight against the probe. The inserts are equipped with a groove in the end that interfaces with the probe. The groove provides an interference fit for the o-ring that allows it to stay in place. The receiver tube end of the insert is the same size as the splitter port. The receiver tubes mate with inserts with an interference fit exactly the same as the splitter ports.

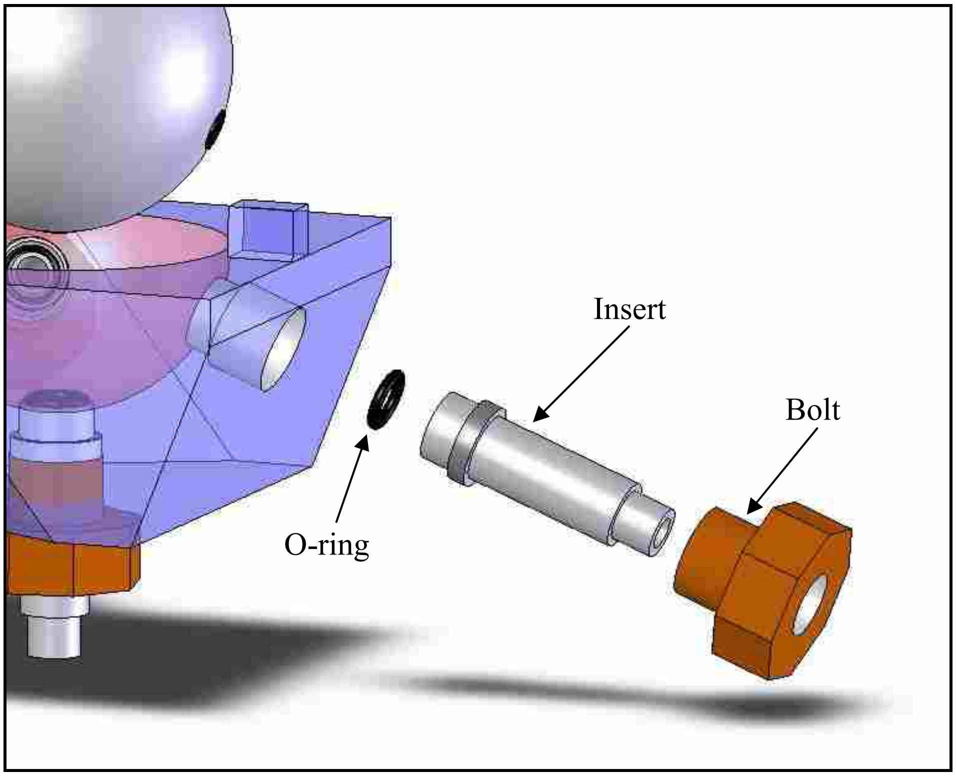

Figure 5–20: Microphone port exploded view close-up

The interference mate between the receiver tubes and the inserts compared to the interference fit between the receiver tubes and the splitter ports is illustrated in Figure 5–21. Figure 5–21 illustrates that the connection at both ends of the receiver tube is the same. The interference fit at both ends of the receiver tube is made possible by the flexible nature of the receiver tube material. The tube simply stretches over the splitter port and over the insert. The connection at both ends of the receiver tube causes diameter discontinuities that are accounted for in the models in Chapter 4. The discontinuities, as discussed in Chapter 4, are acoustic inductances and can be thought of physically as additional length.

The acoustic path from the splitter to the probe microphones is illustrated in Figure 5–21. The sectioned view is useful to see how the sound travels from the splitter at the end of the driver tube, through the receiver tube to the insert. The probe microphone terminates the insert. The tubes must be the same length for the acoustic path to be similar. The length restriction and probe microphone locations cause the tubes leading to different microphones to bend in different ways.

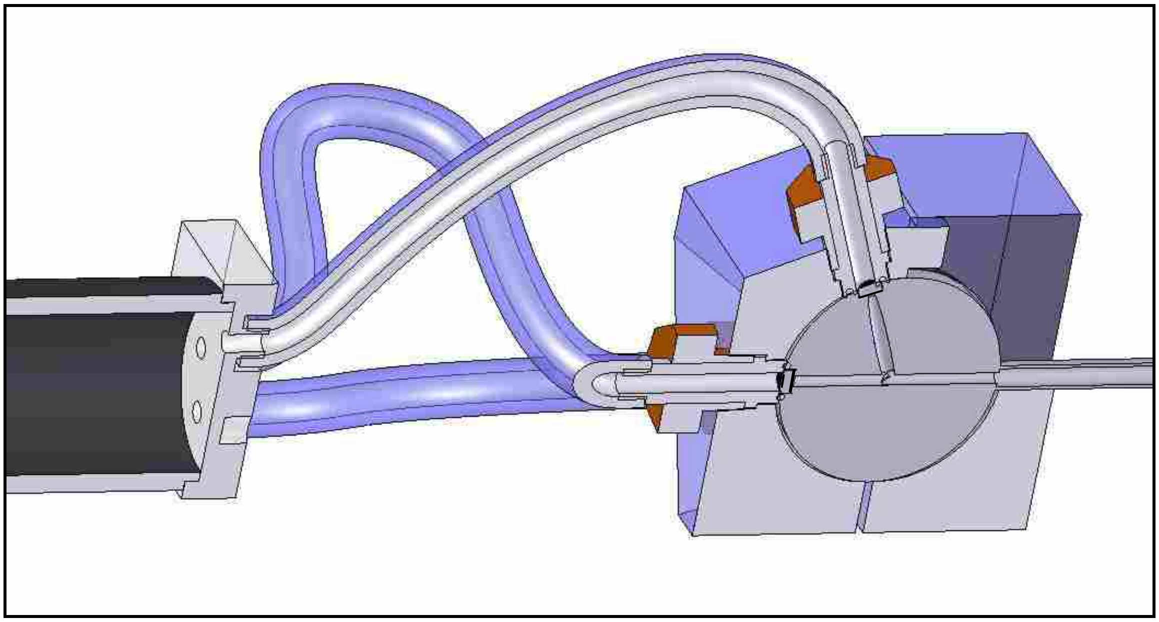

Figure 5–21: Sectioned view of acoustic path from the splitter to probe microphone

5.8 ENTIRE CALIBRATOR ACOUSTIC PATH

A CAD model of the entire calibrator is shown in Figure 5–22. This model illustrates the actual calibrator photographed and shown in Figure 5–1. This model is useful to visualize the entire acoustic path the sound must take from the calibrator source to the probe microphones and the reference microphone. The reference microphone is used as the reference in the relative calibration technique to obtain the sensitivity of the probe microphones.

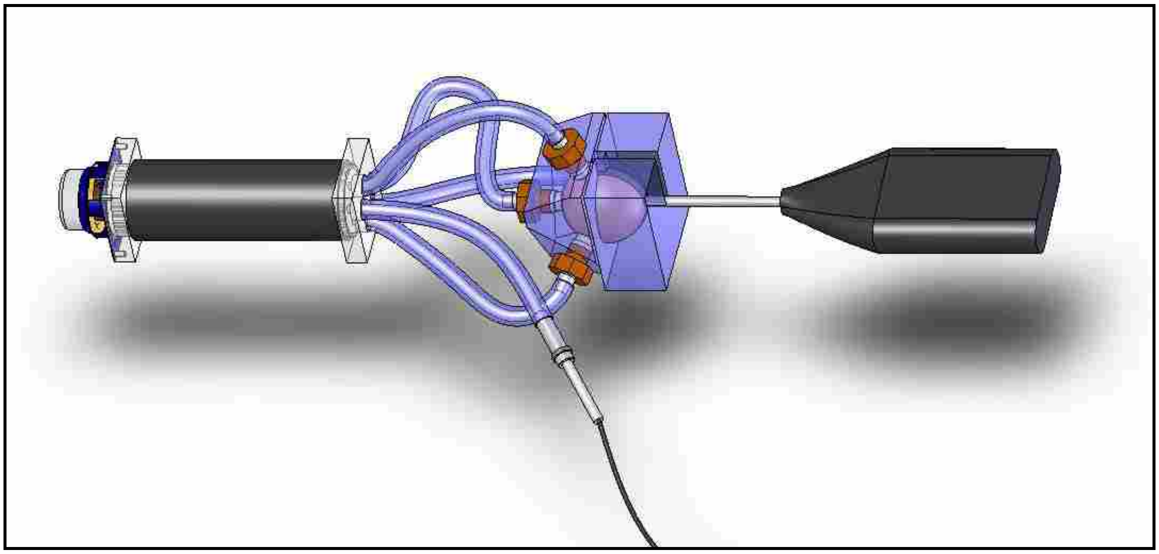

Figure 5–22 Entire calibrator CAD model

A sectioned view of the entire calibrator is shown in Figure 5–23. The sectioned view allows the reader to see exactly where the sound travels as it propagates through the entire calibrator. Figure 5–23 illustrates all of the waveguides in the calibrator. The driver tube is the primary waveguide and each of the five paths consists of three waveguides. The first path waveguide is inside of the splitter port, the second is the receiver tube, and the third is the inside of the insert.

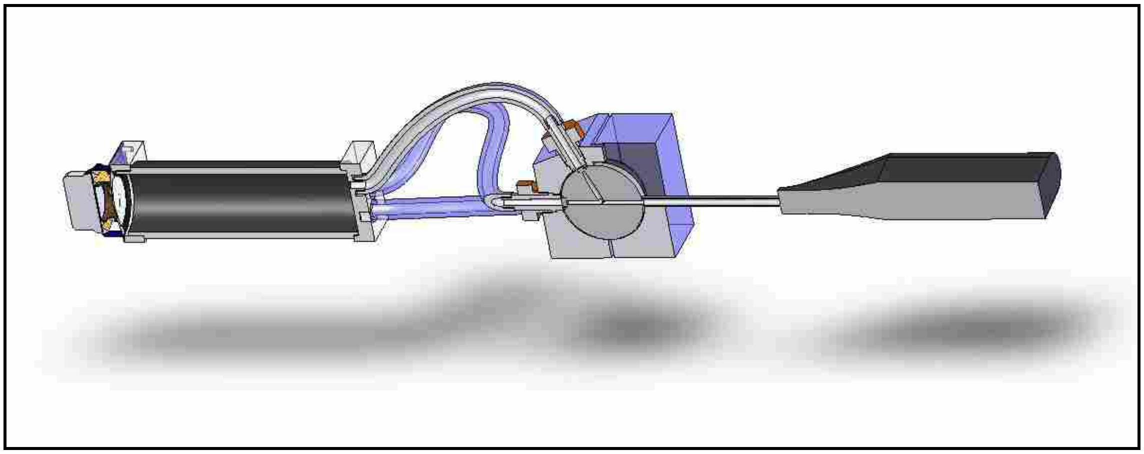

Figure 5–23: Entire calibrator CAD model sectioned view

6 MEASUREMENTS AND RESULTS

This chapter discusses the methods used to validate the calibrator. The calibrator was validated at three different stages. The procedure and experimental setup used at each of the stages is explained. The results obtained from the validation at each stage are presented and discussed.

6.1 VALIDATION STAGES

The calibrator was validated at three stages. The first stage validated was the splitter. Second, the receiver tubes were validated to show that the tubes are acoustically the same. Third, the full calibrator was validated. All three stages were validated at several discrete frequencies as outlined in Sections 6.2–6.4. The entire calibrator was then validated over a continuous range of frequencies as outlined in Section 6.4.

6.2 SPLITTER VALIDATION

The purpose of validating the splitter was to prove that the splitter was dividing the volume velocity into equal parts. If the volume velocity is equally divided the pressure would be the same at the entrance to each port. To validate that the splitter was dividing the volume velocity equally to each receiver tube, the driver was excited with a 500 Hz harmonic sine wave. The pressure was measured at each of the five ports of the splitter using a 0.00632 m precision microphone. A photograph showing the splitter validation setup is shown in Figure 6–1. In Figure 6–1 a single microphone is shown positioned at one of the splitter ports.

Each port was measured individually using the same microphone. The pressure measured does not represent the pressure that exists at the port prior to the microphone placement. The port being measured has a different acoustic impedance than the ports not being measured. The microphone being placed in front of the port causes a change in impedance. For this validation the impedance differences were ignored because the setup was the same for each measurement. For each measurement, the port being measured had the same impedance, and the ports not being measured had the same impedance. This setup compares each port when being measured using the microphone and the remaining four open, to all five ports under the same circumstances.

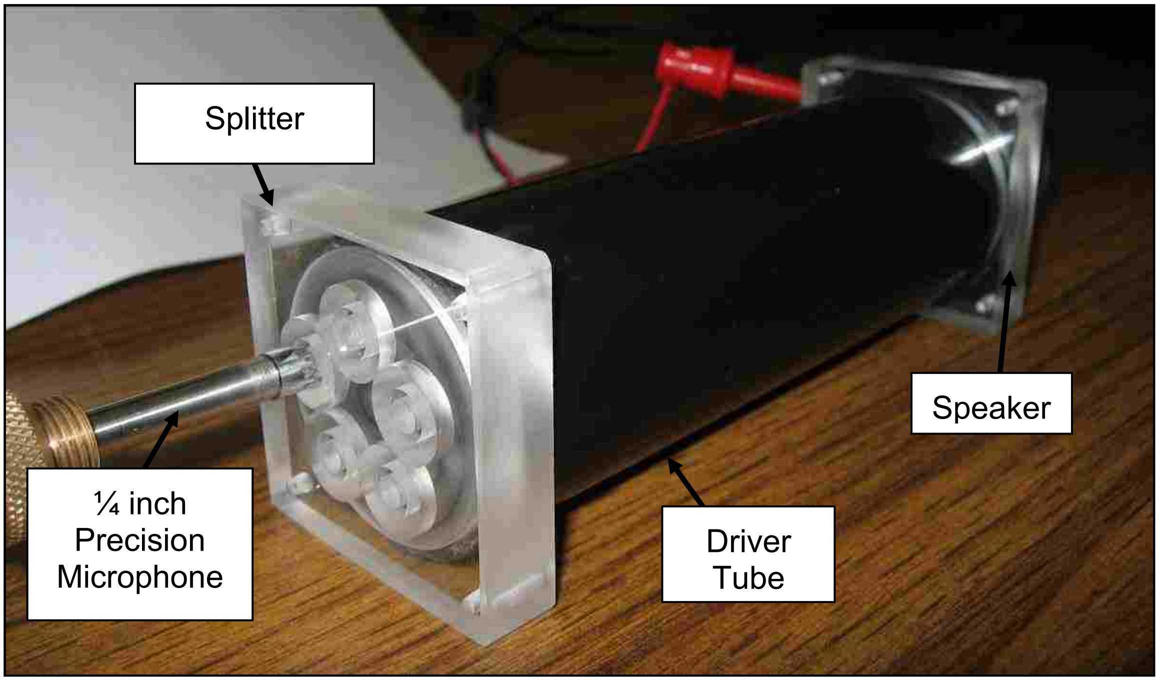

Figure 6–1: Splitter validation.

No change in the results was observed after five measurements; therefore only five measurements were made at each port. The five measurements at each port were averaged, and the largest difference (in dB) between any two of the five ports was calculated. This process was repeated at every 500 Hz, from 500 Hz to 6000 Hz. The results from this test were plotted. The results are shown in Figure 6–2. The splitter is capable of dividing the volume velocity equally within ± 0.5 dB up to at least 3000 Hz. These results show that the splitter adequately divides the volume velocity to each of the five ports. As expected the error is very large at the cutoff frequency (5 k Hz) of the first higher order mode of the driver tube.

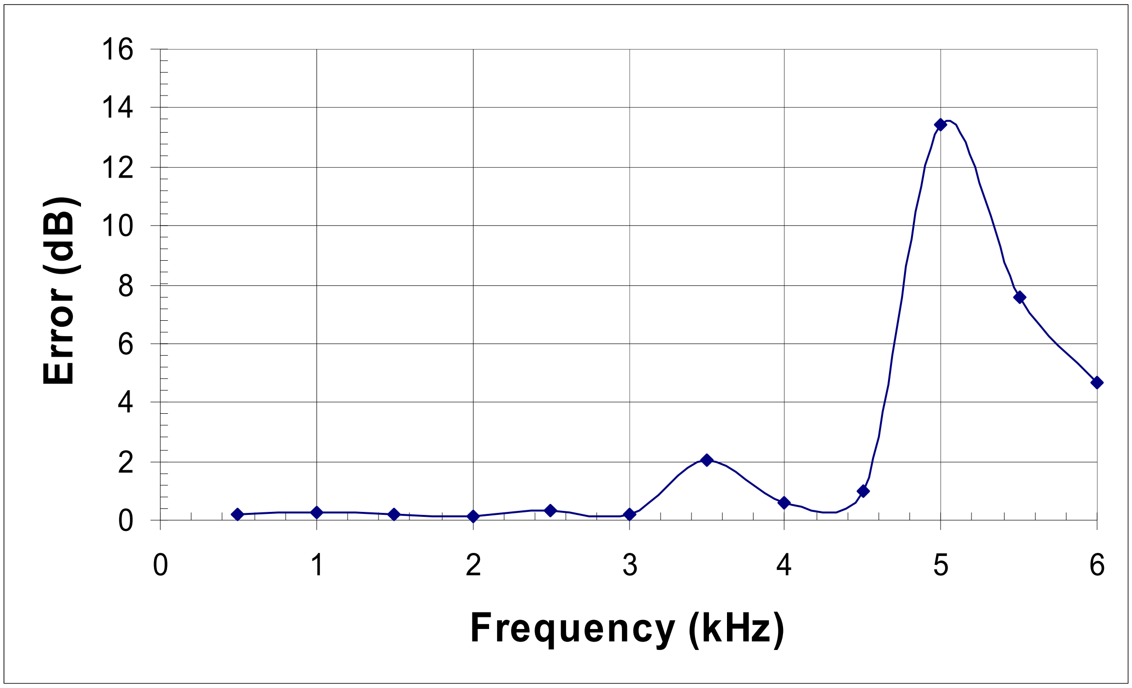

Figure 6–2: Splitter verification results

6.3 RECEIVER TUBE VALIDATION

The receiver tubes were validated two ways. The first receiver tube validation compared the pressure at the end of each receiver tube. The second receiver tube validation compared different bending orientations of one of the receiver tubes. The purpose of the first validation was to prove that the receiver tubes are acoustically the same. The purpose of the second validation was to prove that the receiver tubes could be allowed to bend without introducing error.

6.3.1 Acoustic Equality Validation

The receiver tubes were tested similar to the splitter port test described above, using harmonic waves at frequencies of 250 Hz, 300 Hz, 400 Hz, 500 Hz, 600 Hz, 700 Hz, 800 Hz, 900 Hz, 1000 Hz, 1500 Hz, and 2000 Hz. The 2000 Hz upper limit was chosen based on the operational limit of the probe. At each of the above frequencies the pressure was measured at the end of each receiver tube, and the largest difference between any of the five receiver tubes was calculated. This difference was used to calculate the error in dB at each of the frequencies listed above. The error was plotted at each of the measured frequencies. The results of this test are shown in Figure 6–3. The goal was to limit the error to less than ±0.5 dB (a class 1 probe), and as can be seen from Figure 6–3, this was accomplished at the discrete frequencies listed above. Conclusions can only be made from the results at the discrete frequencies and not the frequencies that were not measured.

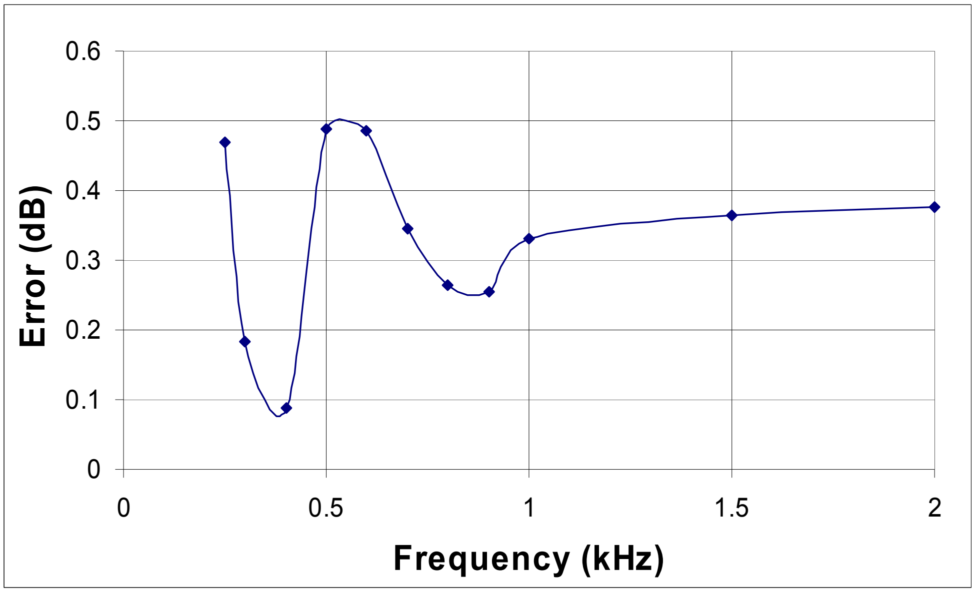

Figure 6–3: Receiver tube acoustic equality validation results

6.3.2 Bending Validation

In order to reach each microphone on the probe, the receiver tubes need to bend. The error introduced as a result of bending the tubes was determined with the following test. The pressure at the end of each tube was measured with the tube straight and then bent at 30, 60, and 90 degrees. The pressure was measured at the end of each tube in each position five different times.

The null hypothesis was formulated that the bending of the tubes would not cause any change in the acoustical path of the receiver tubes. A single factor analysis of the variance (ANOVA) was performed on the five runs at each orientation with $\alpha = 0.05$. The analysis produced a *P*-value of 0.57. Since the *P*-value is greater than the α value of 0.05 the null hypothesis was not rejected[36]. With $\alpha = 0.05$ and a *P*-value that is larger, the probability that the variance in the data is just noise is 95%.

Table 6–1 shows the results of the ANOVA. In Table 6–1, the number of measurements for each receiver tube is given by the count; the sum, average, and variance for each receiver tube are also shown. Table 6–1 also shows the squared error *(SS)*, the degrees of freedom *(df)*, the mean square *(MS)*, and the P-value. The P-value is the probability value used to compare to the confidence interval. The analysis of the variance provided confidence that the receiver tubes could be bent to align with the probe and remain acoustically the same.

Table 6–1: Bending validation ANOVA results

ANOVA: Single Factor

Groups	*Count*	*Sum*	*Average*	*Variance*
Tube 1	4	53.998	13.4995	0.00205767
Tube 2	4	53.859	13.46475	0.00107958
Tube 3	4	53.861	13.46525	0.00175225
Tube 4	4	53.858	13.4645	0.002531
Tube 5	4	53.819	13.45475	0.00046958

Source of Variation	*SS*	*df*	*MS*	*P-value*
Within Tubes	0.00473	4	0.00118288	0.57346547
Between Tubes	0.02367	15	0.00157802	
Total	0.0284	19		

6.4 FULL CALIBRATOR VALIDATION

The entire calibrator was validated at several discrete frequencies, and over a continuous frequency range. Both the discrete and continuous validations were performed using the calibrator with the orthogonal probe in calibrator position. Both the continuous and discrete calibrator validations indicate that the calibrator can calibrate the probe microphones within 0.5 dB at frequencies at or below 2000 Hz. Both validations also show that the calibrator can calibrate within 0.7 dB for frequencies above 2000 Hz.

6.4.1 Discrete Frequency Validation

The driver was excited with a 114-dB (as measured with the reference microphone) harmonic wave at 250 Hz, 500 Hz, 1000 Hz, 2000 Hz, and 3000 Hz. The probe were inserted into the attachment and a one-second time signal was recorded from each microphone on the probe, and the reference microphone. The probe was taken out of the attachment and rotated so that the three side microphones on the probe were each connected to a different receiver tube. The pole microphone and the reference microphone remained connected to the same receiver tubes. Another time signal was recorded and the rotation was repeated. The data for each of the three measurement configurations were normalized about the first position. The error at the second and third positions relative to the first position was calculated. This entire process was repeated for the five frequencies mentioned above. The physical limitations of the driver reduced the amplitude of the harmonic wave at 2 and 3 kHz to 110 dB.

The error plots for each of the five frequencies can be seen in Figure 6–4 through Figure 6–8. The error at 250, 500, 1000, and 2000 Hz were all less than the 0.5 dB. The error at 3000 Hz was greater than 0.5 dB but less than 0.7 dB. The results indicate that the calibrator is capable of calibrating the probe at 250, 500, 1000, and 2000 Hz to the class 1 probe standard. The results at 3000 Hz indicate that the calibrator is capable of calibrating the probe to the class 2 probe standards at 3000 Hz.

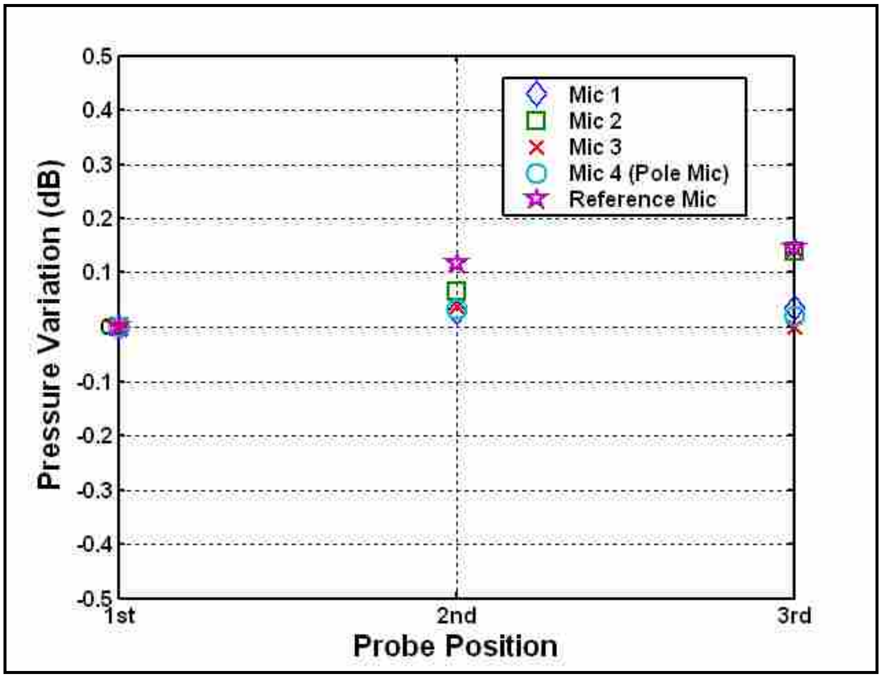

Figure 6–4: Calibration error at 250 Hz and 114 dB

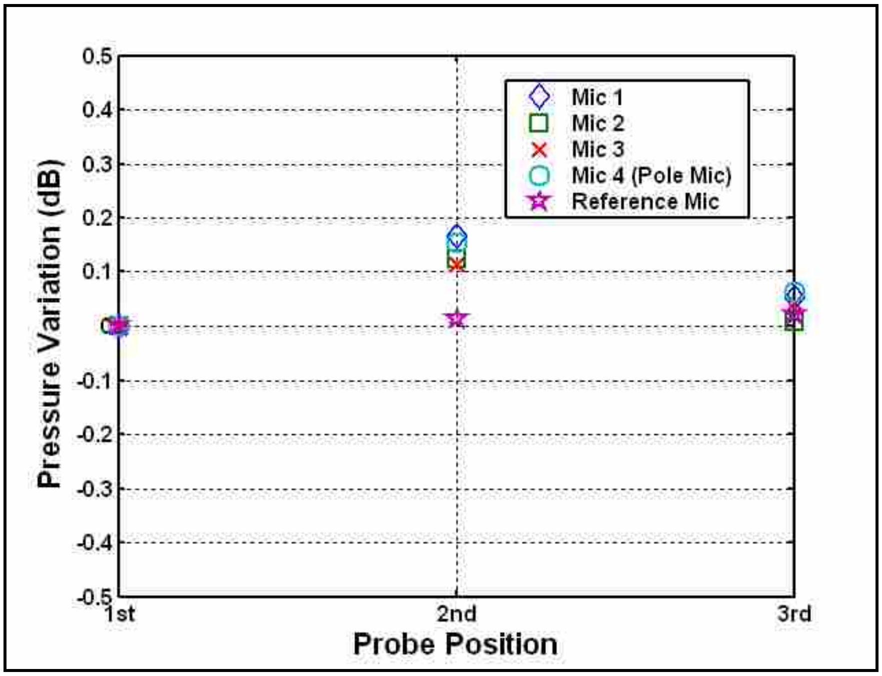

Figure 6–5: Calibration error at 500 Hz and 114 dB

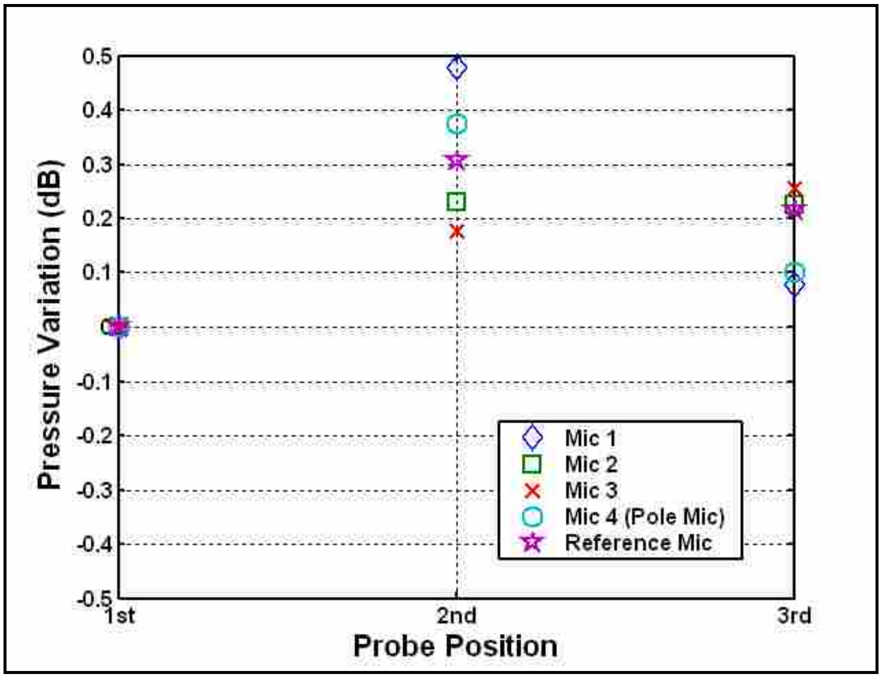

Figure 6–6: Calibration error at 1000 Hz and 114 dB

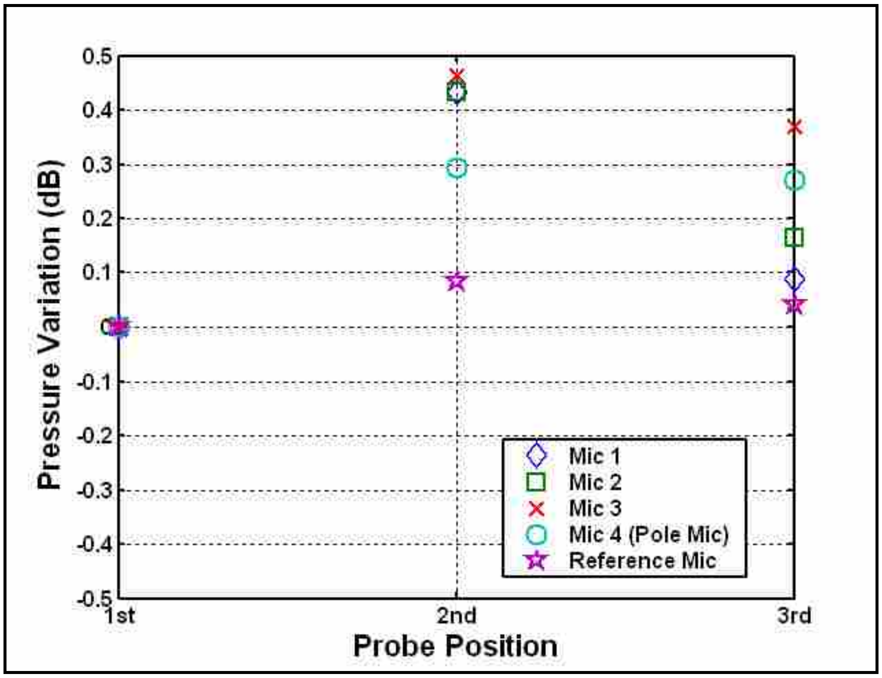

Figure 6–7: Calibration error at 2000 Hz and 110 dB

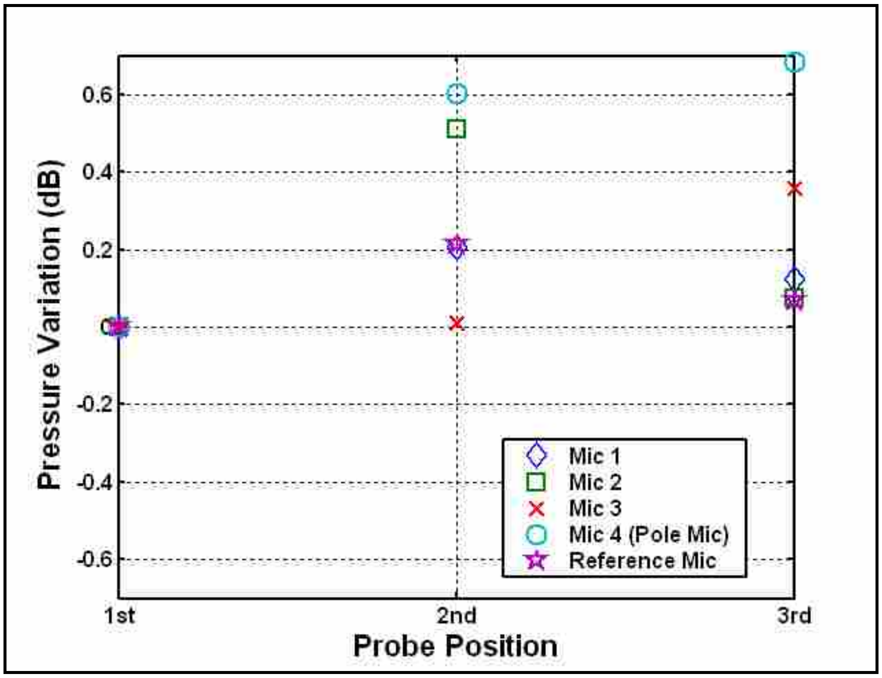

Figure 6–8: Calibration error at 3000 Hz and 110 dB

For all five of the frequencies tested, the second and third positions showed random variation. This variation was deemed insignificant as it was not repeatable and the results are within the target limits.

6.4.2 Continuous Frequency Range Validation

The calibrator was further tested using white noise as the signal input. Measurements were made with the probe in the calibrator just as it would be during calibration. The frequency response function (FRF) was calculated using 20 averages. The number of averages corresponded with a coherence greater than 0.98 between the input and the output. The FRF was measured at the end of each insert connected to the end of a receiver tube (end of the acoustic path). Five measurements were made, and the average of each receiver tube was calculated. The FRF of each of the receiver tubes is shown in Figure 6–9. Figure 6–9 also illustrates that beyond the cutoff frequency of the first higher order mode in the driver tube the pressure varies significantly. One of the measured FRFs shown in Figure 6–9 was used as the measured FRF to compare with the modeled results in Chapter 4. Recall from Chapter 4 that the path terminations were assumed to have infinite acoustic impedance. This can be thought of physically as the microphones have a much higher acoustic impedance than the tubes. For this to occur the ends of the paths (the inserts) must seal around the microphones.

The FRF results from each receiver tube were averaged to obtain an overall mean. To calculate the error at each receiver tube, the overall mean was subtracted from each of the five FRF measurements at each receiver tubes. The resulting errors at each receiver tube were then averaged to obtain an average receiver tube error (μ). The standard deviation of each of the five error calculations for each receiver tube was calculated (σ). Using the mean and standard deviation of the error, an interval at each receiver tube is calculated using Eq. (6.1).

$$Interval = \mu \pm 2\sigma \qquad \textbf{(6.1)}$$

The interval corresponds to a confidence of 95.45% that the error will fall in the limits of the interval[36]. The interval for each receiver tube was plotted along with the mean error μ and the upper and lower control limits for a class 1 and class 2 probe. These plots are shown in Figure 6–10 through Figure 6–14. In Figure 6–10 through Figure 6–14 the upper and lower limits of the confidence interval are illustrated using the down pointing and up pointing triangle respectively. The upper and lower control limits for a class 1 and class 2 probe are illustrated by the dashed and dotted lines respectively.

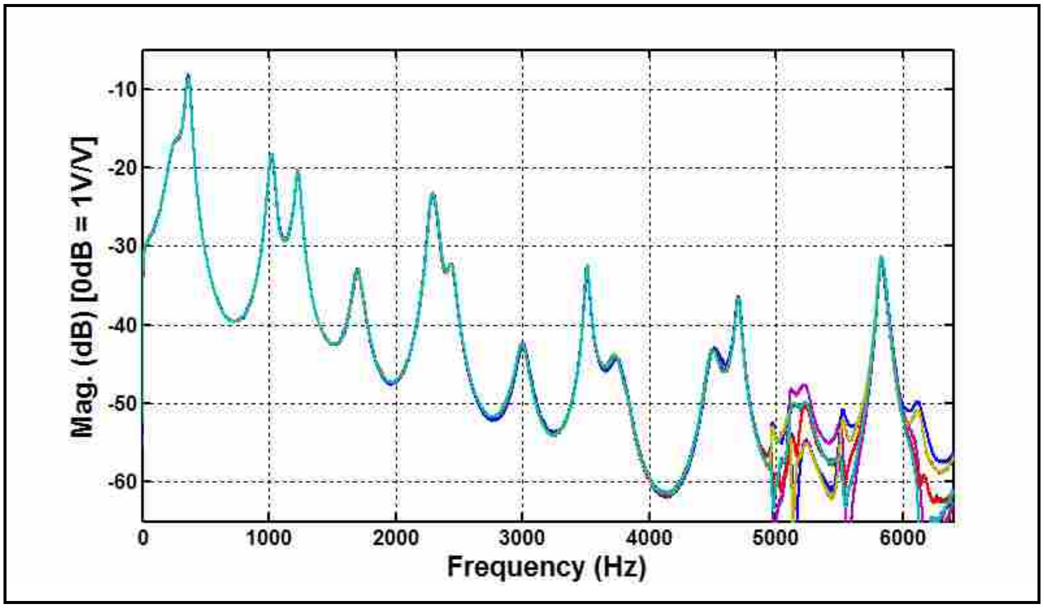

Figure 6–9: FRF of the five receiver tubes

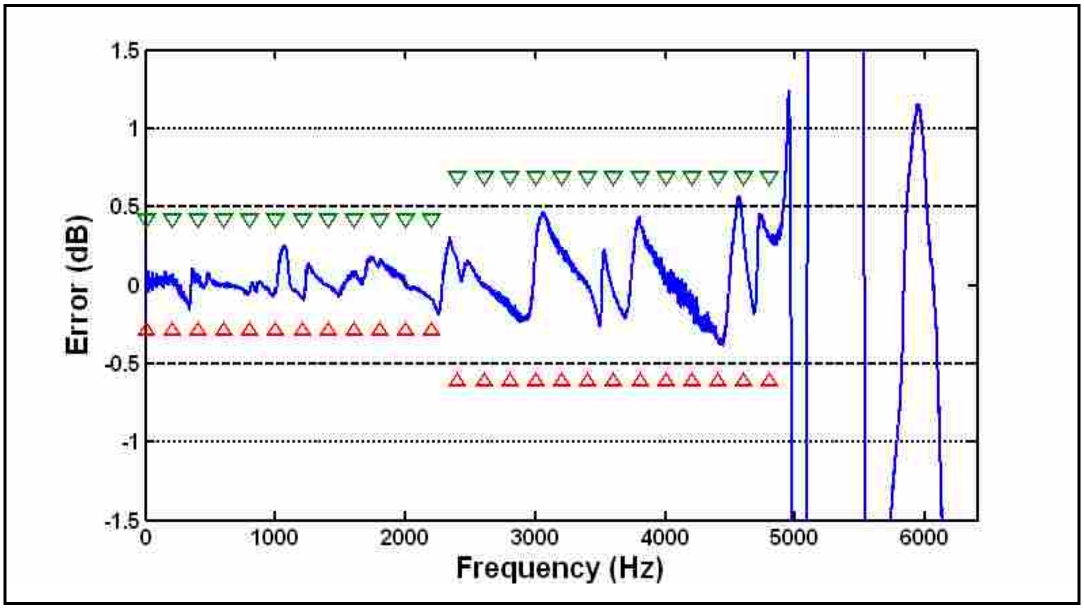

Figure 6–10: Receiver tube 1 error with confidence interval

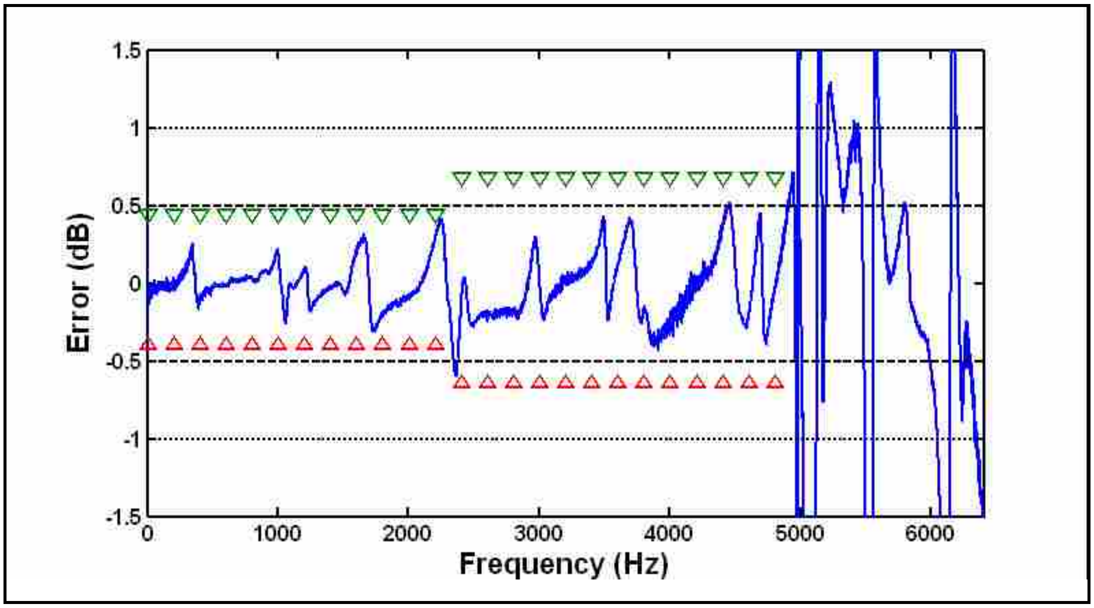

Figure 6–11: Receiver tube 2 error with confidence interval

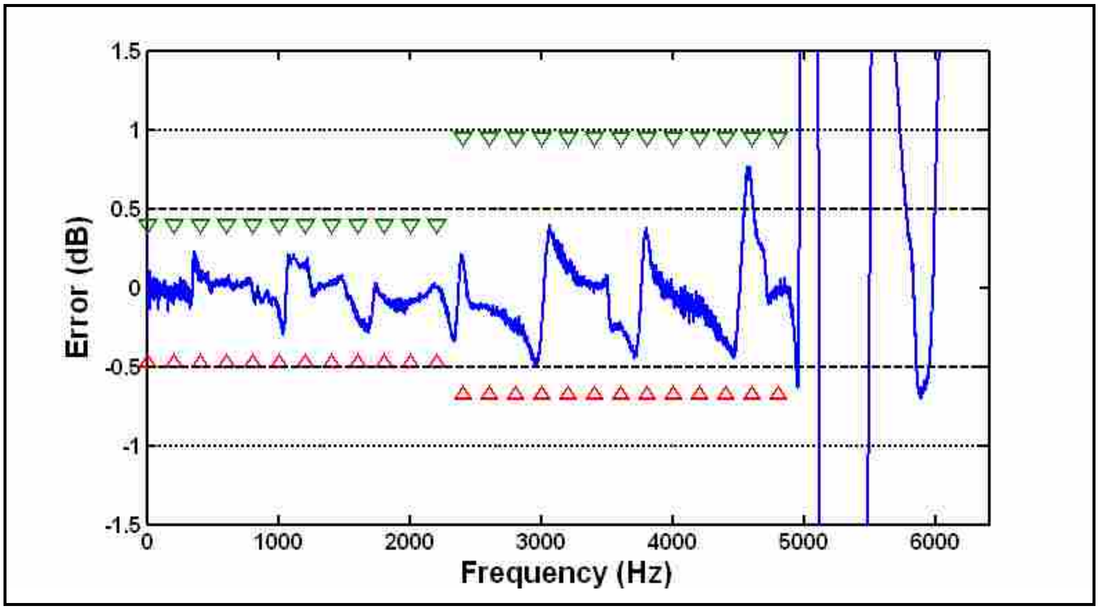

Figure 6–12: Receiver tube 3 error with confidence interval

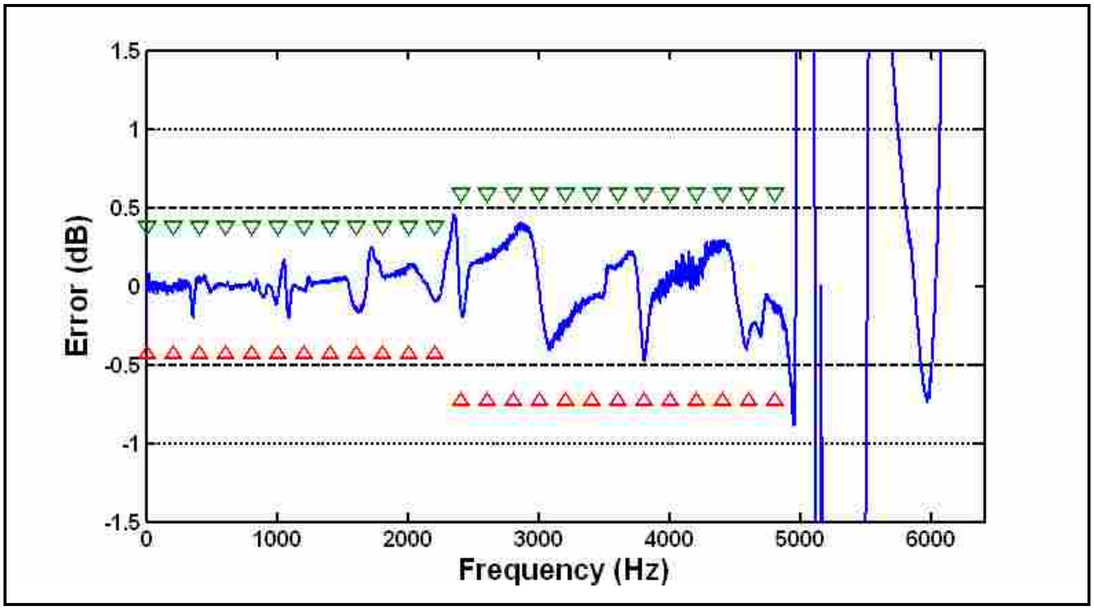

Figure 6–13: Receiver tube 4 error with confidence interval

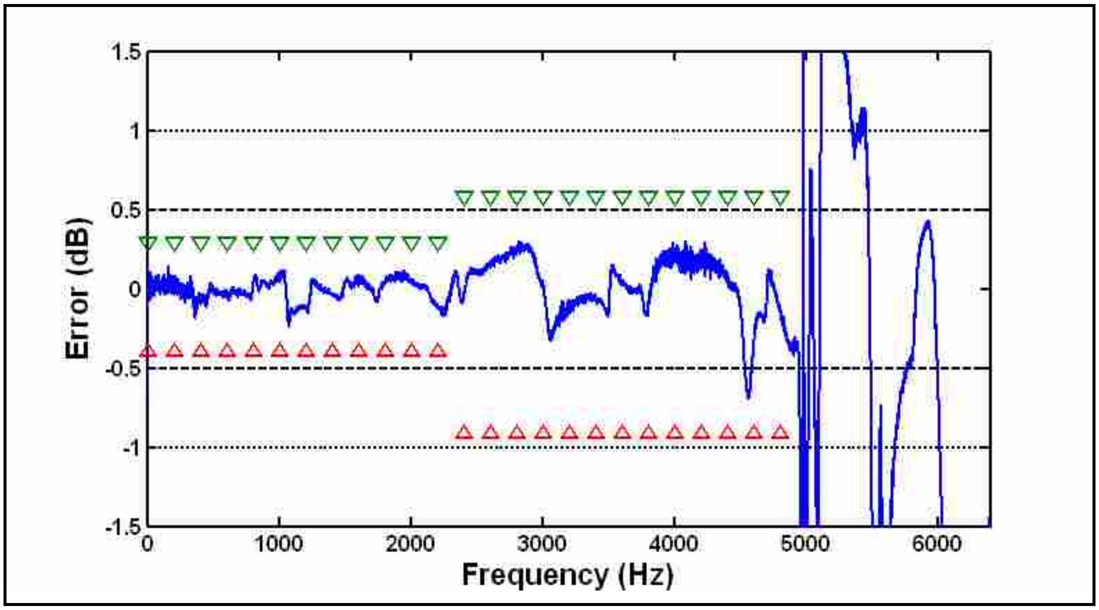

Figure 6–14: Receiver tube 5 error with confidence interval

7 ORTHOGONAL PROBE DIRECTIVITY

This chapter discusses the directional characteristics of the probe used to verify the calibrator referred to as the orthogonal probe[20]. The probe is intended to measure pressure and calculate acoustic energy density independent of the probes orientation when the pressure measurements are made. Locey[20] stated that the orthogonal probe had the most potential of the three spherical probes he investigated, but that it might have a directional dependence. This chapter discusses how the orthogonal probe calculates energy density, and the source of the directional dependence of the probe. The chapter presents the corrections made to allow the orthogonal probe to be directionally independent. This chapter also presents the results of a comparison between the calibrated orthogonal probe and the Microflown.

7.1 ENERGY DENSITY CALCULATION

The total energy density calculation uses the particle velocity, which is a vector. The velocity calculations have a large affect on the probe’s directional performance. The probe’s dependence on particle velocity necessitates an investigation into how the velocity is calculated when using the orthogonal probe.

The orthogonal probe shown in Figure 7–1 calculates energy density from four pressure microphone measurements. Spherical probes use the pressure measurements that are made on the surface of the sphere to calculate the pressure at the center of the sphere using a finite sum[18,20]. The orthogonal probe uses the pressure measurements to calculate the particle velocity at the center of the sphere using finite difference along with a Taylor series expansion[20]. After the pressure and particle velocity are calculated at the center of the sphere, the energy density is calculated at the center of the sphere. The energy density is calculated as outlined in Section 2.2.

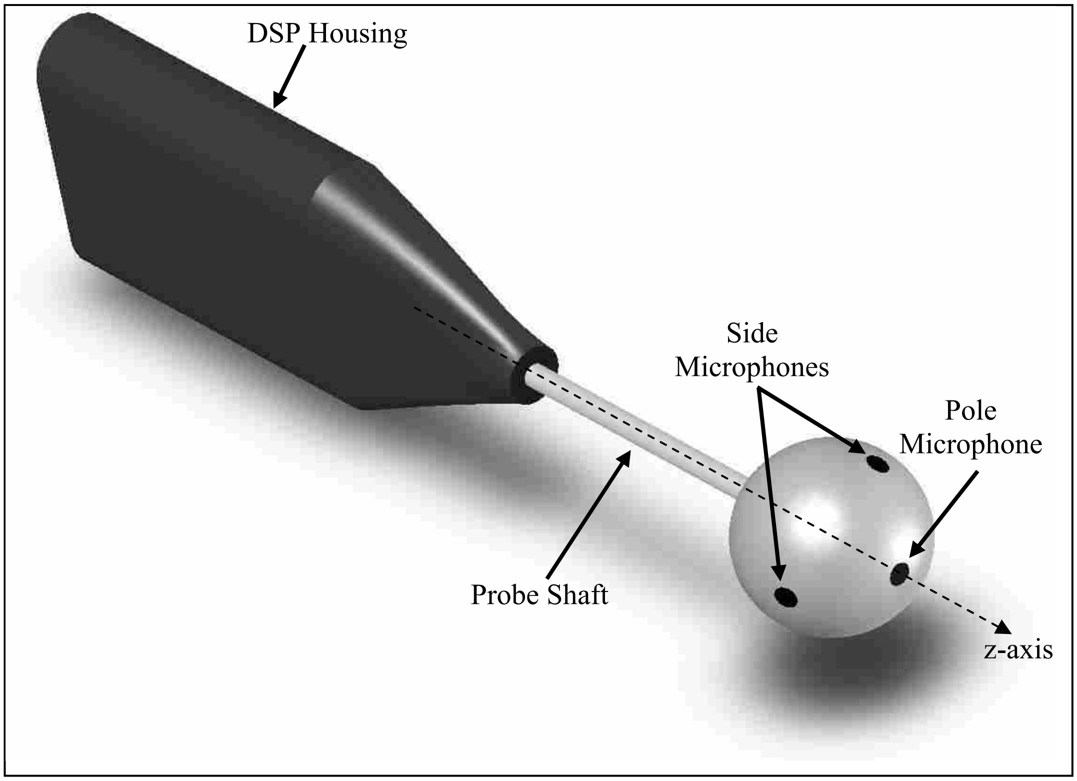

Figure 7–1: Orthogonal probe

7.1.1 Particle Velocity Estimation

The orthogonal probe calculates the particle velocity at the midpoint between two microphones using Eq. (2.5). Locey[20] modeled the orthogonal probe using a coordinated system that was derived from the microphone positions in the probe. To understand how the velocity is calculated the coordinate system must be examined. Locey[20] labeled the pole microphone as microphone 3 the side microphones as microphones 1, 2, and 4. The vectors that connect microphone 3 to the other three microphones form an orthogonal set of vectors. The origin of the coordinates was at the center of microphone 3. Figure 7–2 illustrates the microphone coordinate system relative to the probe microphone with the microphones labeled using Locey's labeling system. The microphone coordinate system is unrelated to the probe coordinated system described in Section 7.2.

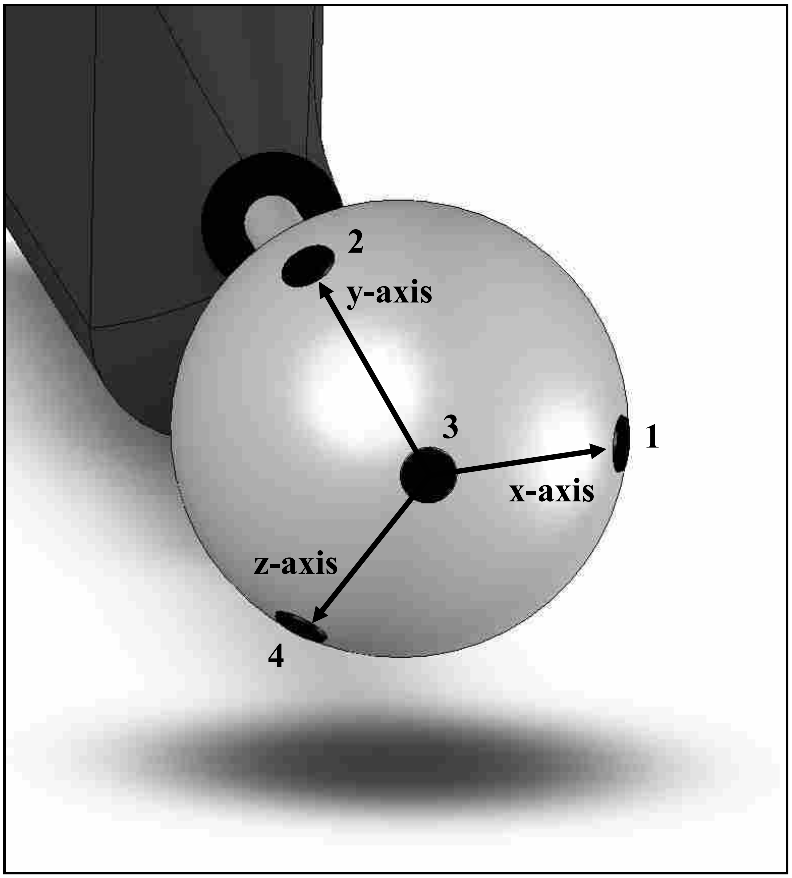

Figure 7–2: Orthogonal microphone coordinate system

The coordinate system axes travel from the pole microphone at the origin through the sphere to the respective side microphones. The pole microphone is numbered microphone 3 and 1, 2, and 4, are the side microphones. The x-y plane cuts through the probe sphere as shown in Figure 7–3. Locey[20] explained that with four microphone measurements six pressure gradients exist from which the velocity is estimated. Three of these velocities can be describe with only one coordinate, the other three require two coordinates. Locey[20] referred to the single coordinate velocities as the "on-axis velocities", and the double coordinate velocities as the "diagonal velocities". Locey [20] labeled the three on-axis velocities as V_{31}, V_{32}, and V_{34} representing the velocity in the x-direction, the y-direction, and the z-direction respectively. Locey[20] referred to the diagonal velocities as V_{12}, V_{14}, and V_{24} representing the velocity in the x-y, x-z and y-z planes respectively. The three on-axis velocities and the three diagonal velocities are used to estimate the velocity at the center of the sphere.

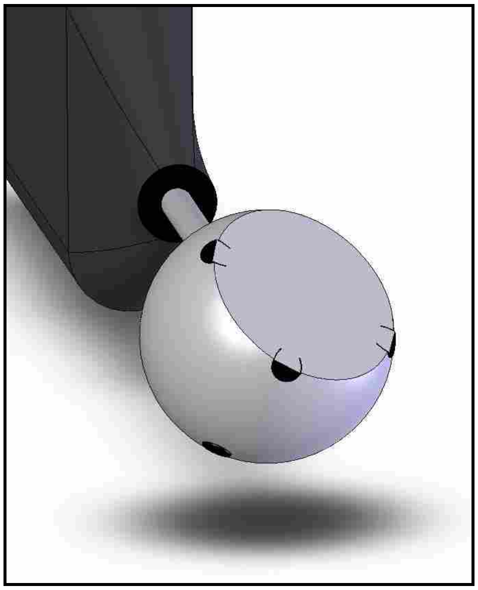

Figure 7–3: Microphone coordinate x-y plane section

The x-y plane sectioned in Figure 7–3 is used to illustrate the calculation of the over all particle velocity component in the x-y direction. Locey[20] referred to this velocity as the unknown velocity. This velocity is labeled V_{xy}. Only the x-y plane is illustrated, because it is the same for the other two planes.

The x-y plane is illustrated in Figure 7–4 relative to the probe microphones and the x, and y axes. The angle α in Figure 7–4 is calculated from the magnitude of V_{31} and V_{32}, which are the two on axis velocities associated with the x-y plane as shown in Eq. (7.1).

$$\alpha = \tan^{-1}\left(\frac{|V_{32}|}{|V_{31}|}\right) \tag{7.1}$$

Once α is determined, θ as shown in Figure 7–4, is calculated by subtracting α from $3\pi/4$ as shown in Eq. (7.2).

$$\theta = \frac{3\pi}{4} - \alpha \tag{7.2}$$

The unknown velocity for the x-y plane is then calculated using the diagonal velocity for the x-y plane and θ as shown in Eq. (7.3).

$$V_{xy} = \frac{V_{12}}{\cos(\theta)} \tag{7.3}$$

This velocity along with the velocity in the x-z plane and the on-axis velocity in the x-direction, are used to calculate the overall particle velocity in the x-direction. Similar analysis is performed for the y and z directions. The correction was implemented at this point. Locey[20] developed the full velocity calculation for this probe.

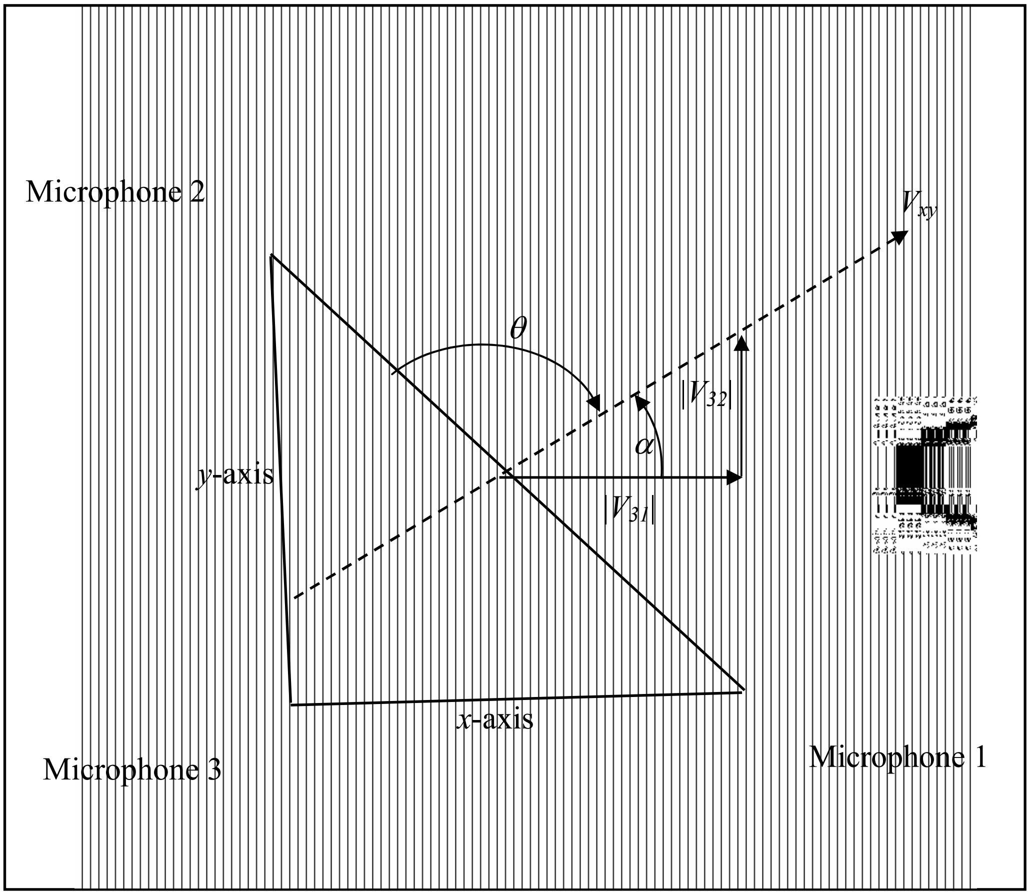

Figure 7–4: Microphone coordinate system x-y plane

7.2 PROBE DIRECTIVITY TEST

The probe was placed in a free field environment and rotated about three orthogonal axes. The three axes of rotation are not the same as the three microphone axes used to calculate the particle velocity described in Section 7.1.1. To avoid confusion the rotation axes were labeled *l*, *m*, and *n*. These axes were chosen based on practical measurement orientations of the probe relative to a source. The *n*-axis used in the rotation is the same as the z-axis shown in Figure 7–1. The *l*-axis was arbitrarily chosen perpendicular to the *n*-axis. The *m*-axis is perpendicular to both the *l* and *n* axes. The origin of the three axes is the center of the probe sphere. Figure 7–5 illustrates the rotational coordinate system of the probe.

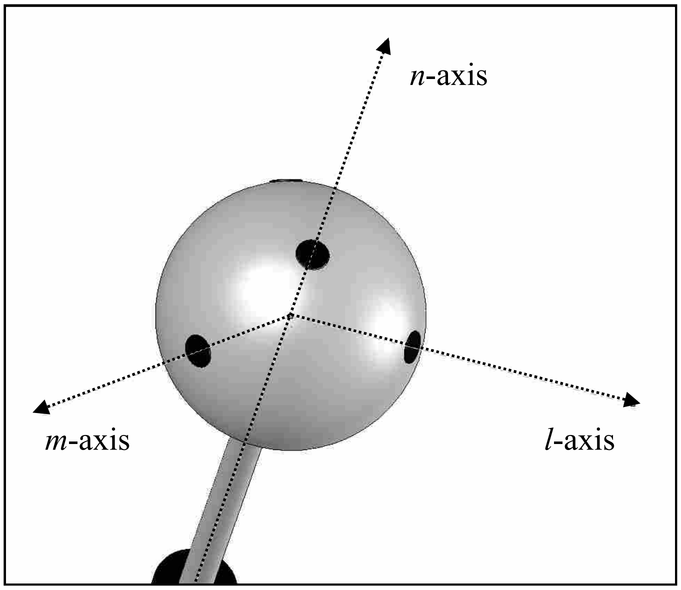

Figure 7–5: Probe rotation axes

7.2.1 Probe *l*-axis Rotation

The orthogonal probe was placed in an anechoic chamber 2 m from a source. The source used was a Mackie High Resolution Active Studio Monitor. The *l*-axis of the probe was aligned with the axis of the bottom Mackie driver as shown in Figure 7–6. In

Figure 7–6 the solid rendering of the probe represents the starting position, and the two transparent renderings represent where the probe will be in future positions as it is rotated about the *l*-axis.

The source was excited using white noise. A 20-second time waveform was recorded using the Larson Davis Digital Sensing System (DSS) connected to a pc laptop via a crossover cable. The data was exported as an ASCII text file. This was repeated every 15 degrees from the starting position (0 degrees) to the final future position (180 degrees). This resulted in 13 measurements that were each 20 seconds long. The positions that would result from a rotation from 180 degrees to 360 degrees were assumed to mirror the results from 0 to 180 degrees.

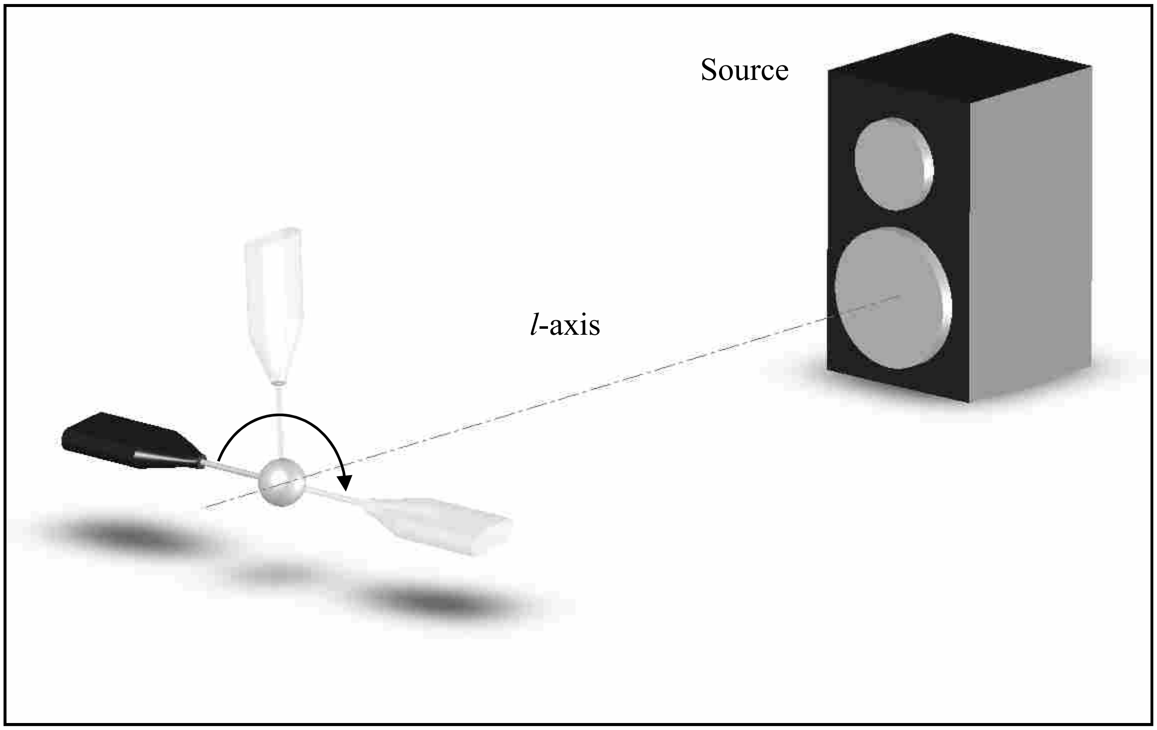

Figure 7–6: Probe *l*-axis rotation

7.2.2 Probe *m*-axis Rotation

The process and setup used to obtain the data for the *l*-axis rotation was repeated for the *m*-axis rotation. The same number of measurements were made for the *m*- axis rotation as the *l*- axis rotation. The *m*- axis rotation is illustrated in Figure 7–7. In Figure 7–7 the starting position (0 degrees) is shown as a solid rendering of the probe, and the two transparent renderings of the probe are two future positions (90 and 180 degrees) of the rotation.

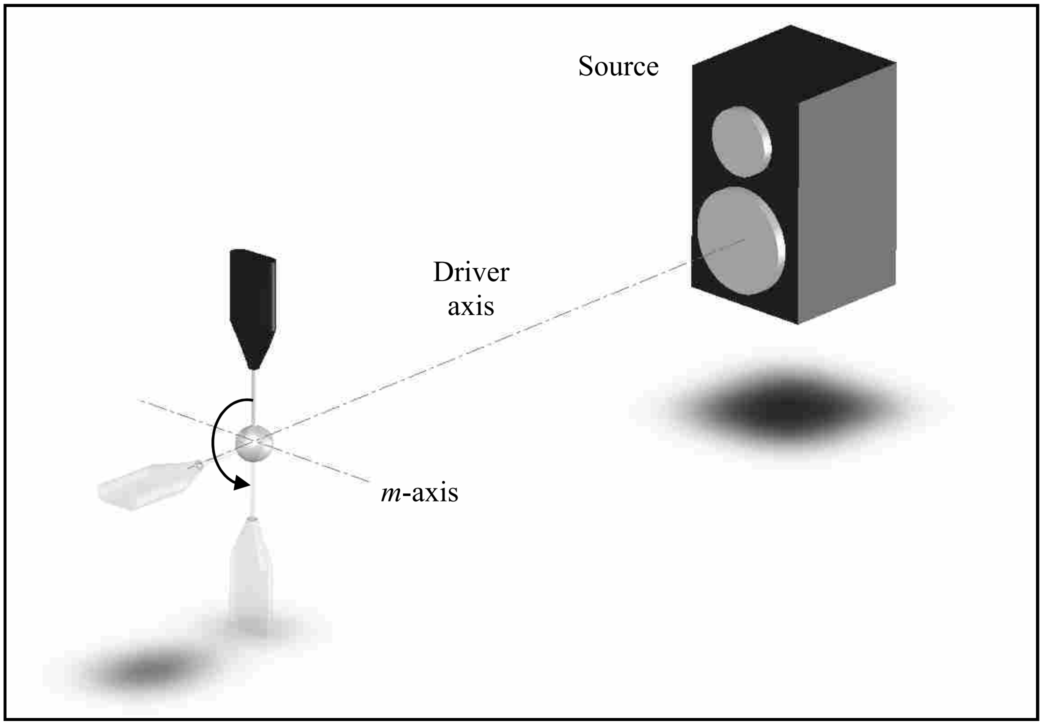

Figure 7–7: Probe *m*-axis rotation

As shown in Figure 7–7 the center of the sphere is aligned with the axis of the bottom driver. An equal number of measurements were made for the *m*-axis rotation as were made for the *l*-axis rotation. For the *m*-axis rotation, the positions from 180–360 degrees were excluded for practical reasons. It was assumed that the probe DSP housing would interfere with the result if the housing was between the probe sphere and the source.

7.2.3 Probe *n*-axis Rotation

For the *n*-axis rotation, the center of the sphere was again aligned with the axis of the bottom driver. Figure 7–8 illustrates the *n*-axis rotation. In Figure 7–8 the orientation of the probe is shown. The source was excited the same as the previous two rotations. The data was obtained and exported the same as the previous two rotations. The probe was rotated all the way around the *n*-axis from 0–360 degrees. The time waveform was recorded at every 15 degrees resulting in 25 measurements each 20 seconds long.

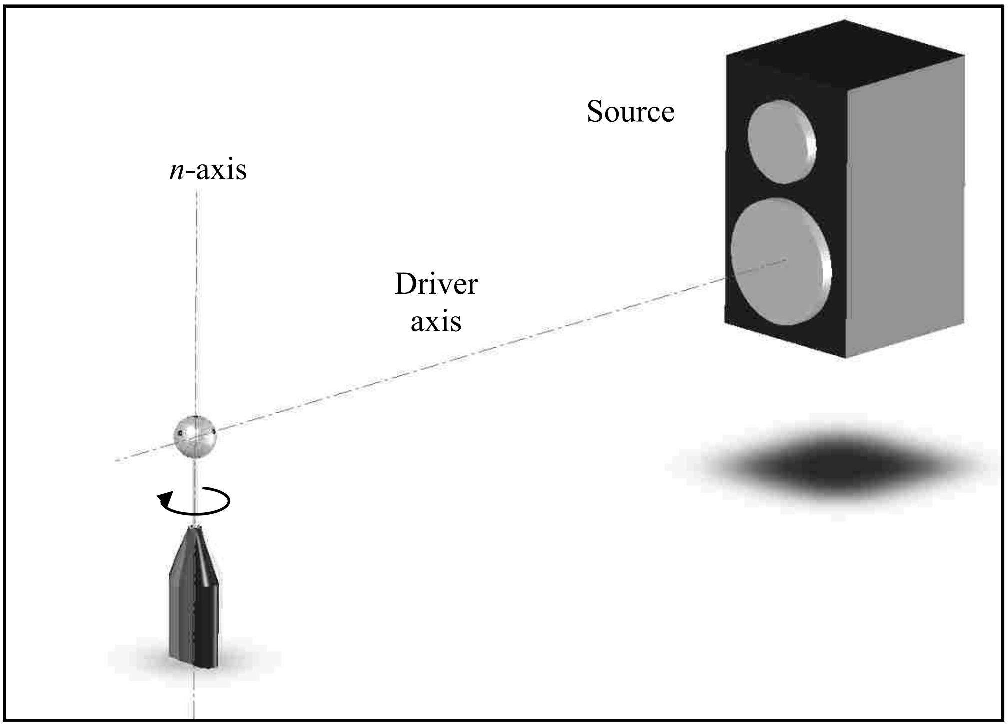

Figure 7–8: Probe *n*-axis rotation

7.3 DIRECTIVITY RESULTS

The data files were imported into MATLAB. At each position 20 seconds of data was recorded. The 20 seconds of data was separated into 20 1-second segments. The FFT of each segment was calculated and the average of all 20 segments for each position was used to calculate the total acoustic energy density.

The energy density as a function of probe position and frequency was calculated two ways. First, the exact MATLAB code developed by Locey[20] for the orthogonal probe was used to calculate the energy density. Second, using a correction function included in Locey's code the energy density was calculated. The correction factor eliminated the velocity calculation in Eq. (7.3) when θ was between 87–90 degrees. In both the original and corrected case, the total acoustic energy density was plotted in dB. The energy density reference used was derived from the reference used for acoustic intensity shown in Eq. (7.4).

$$I_{ref} = 1 \times 10^{-12} \qquad \textbf{(7.4)}$$

The intensity has units of W/m^2. Energy density can be calculated from intensity of a propagating plane wave using

$$ED = \frac{I}{2c} \qquad \textbf{(7.5)}$$

In Eq. (7.5) *ED* is the total energy density, *I* is the intensity, and *c* is the wave speed. By substituting Eq. (7.4) into Eq. (7.5) and solving for *ED,* a reference of 1.5×10^{-15} J/m^3 results. This reference was used to calculate the energy density in dB.

7.3.1 Correction Function

A correction function was developed based on the calculation of the energy density results using Locey's code. It was observed that the velocity calculation in Eq. (7.3) has a singularity point at $\theta = 90$ degrees. If the argument of the cosine function is π/2 or multiples of π/2 the velocity is undefined. The correction function was implemented in the pre-existing code. The results from the calculation using the preexisting code and the results from the calculation using the code with the correction function are presented for all three rotations.

The correction function applies to results when θ was between 87–93 degrees. When this occurred, the velocity calculated using Eq. (7.3) was not used in the calculation of the overall particle velocity. Neglecting this velocity greatly improved the energy density results that will be discussed in Sections 7.3.2 and 7.3.3. The tradeoff for neglecting the velocity component is the energy density calculation is no longer approximated at the exact center of the sphere. The small change in the spatial position of the estimate was deemed acceptable.

7.3.2 Pre-existing Code Directivity Results

The directivity test revealed that the orthogonal probe demonstrated certain frequency dependence. Locey[20] suspected the orthogonal probe to have a directional dependence. The directivity results for the rotation around the *l*, *m,* and *n* axes are shown in Figure 7–9–Figure 7–11 respectively. The plots illustrate the energy density as a function of frequency and probe orientation. The large amplitude spikes result from the singularity point in the velocity calculation shown in Eq. (7.3). It is evident from the results that the sinularity point causes large distortions at certain frequencies and certain angles of probe orientation. Without correction these large distortions cause the energy density results to be unusable.

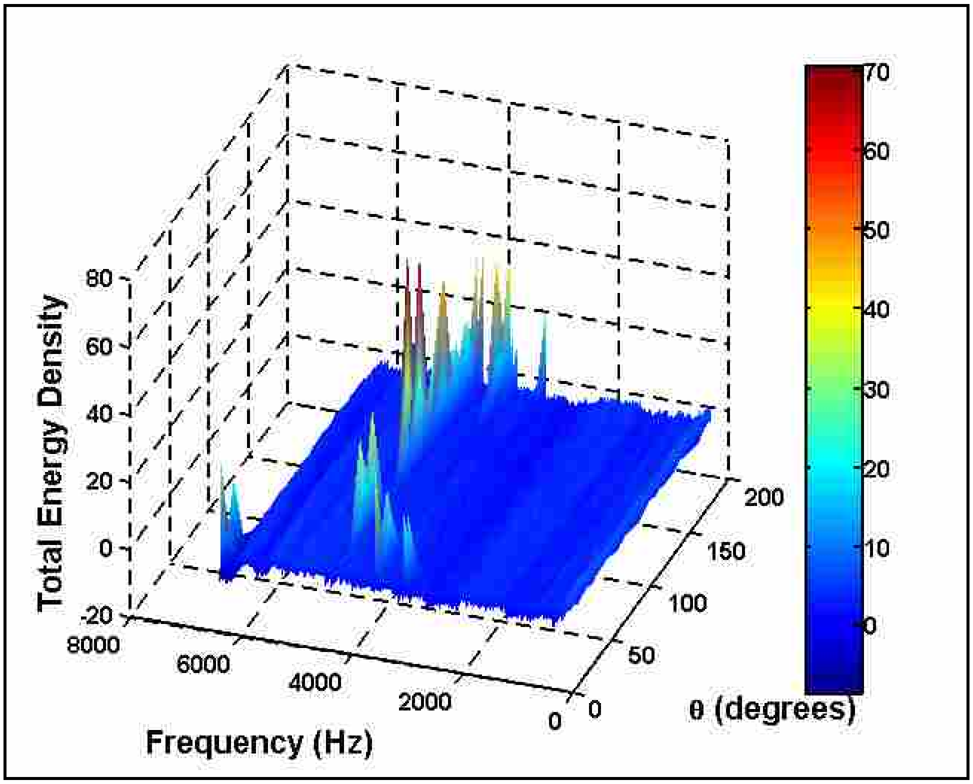

Figure 7–9: *l*-axis directivity results without correction function

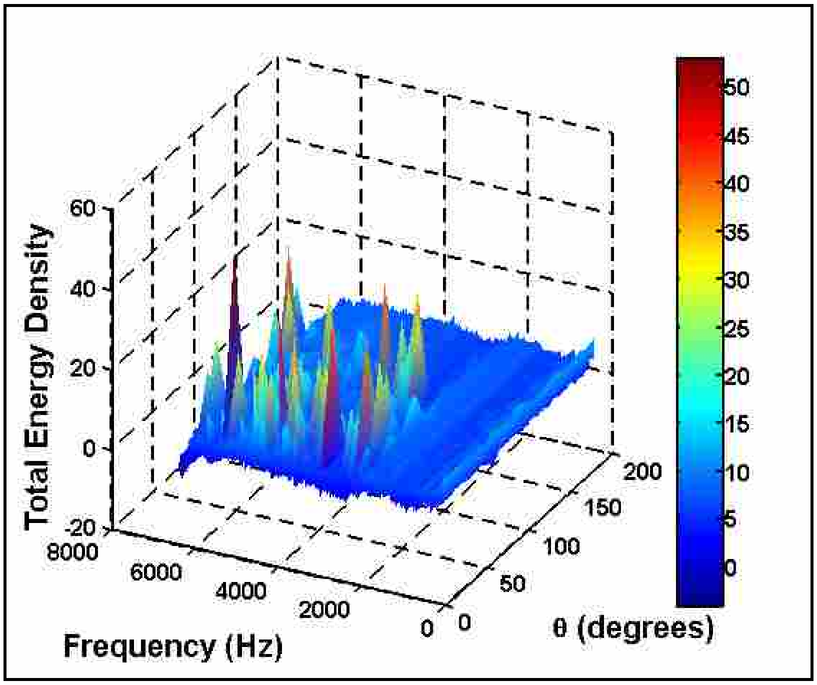

Figure 7–10: *m*-axis directivity results without correction function

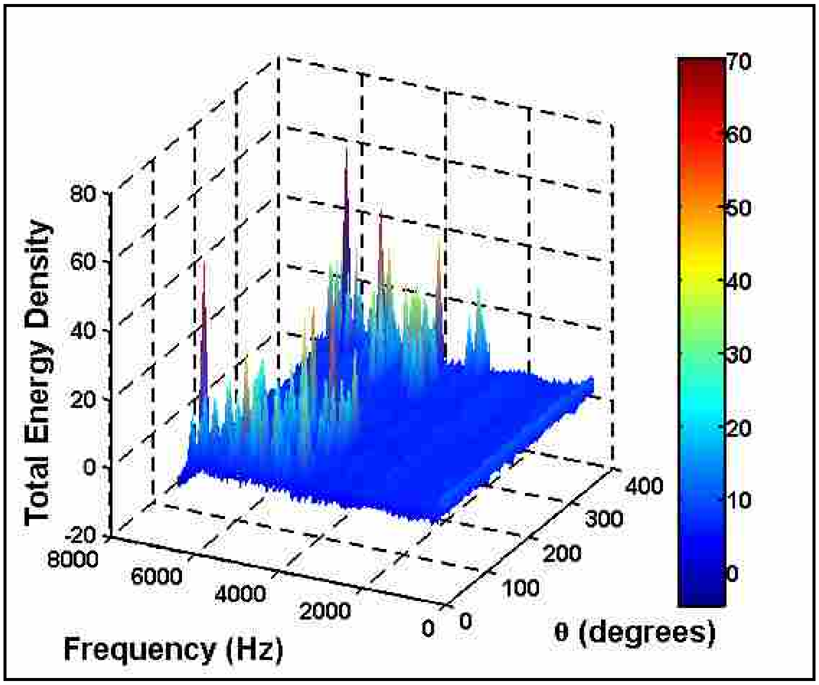

Figure 7–11: *n*-axis directivity results without correction function

7.3.3 Correction Function Directivity Results

The correction function was added and the energy density was recalculated. The results of the directivity test with the correction function included completely eliminated the large spikes due to the singularity point. The total energy density results were plotted as a function of frequency and probe orientation, in 3-dimensional plots similar to those in Section 7.3.2. To illustrate the rotations further, a pseudo color plot was generated for each of the three rotations. Plots showing the average at each frequency and the standard deviation at each frequency were also generated. The results for the rotation about the *l, m,* and *n,* axes are shown in Figure 7–12–Figure 7–23. All of the plots were generated with 10-Hz resolution.

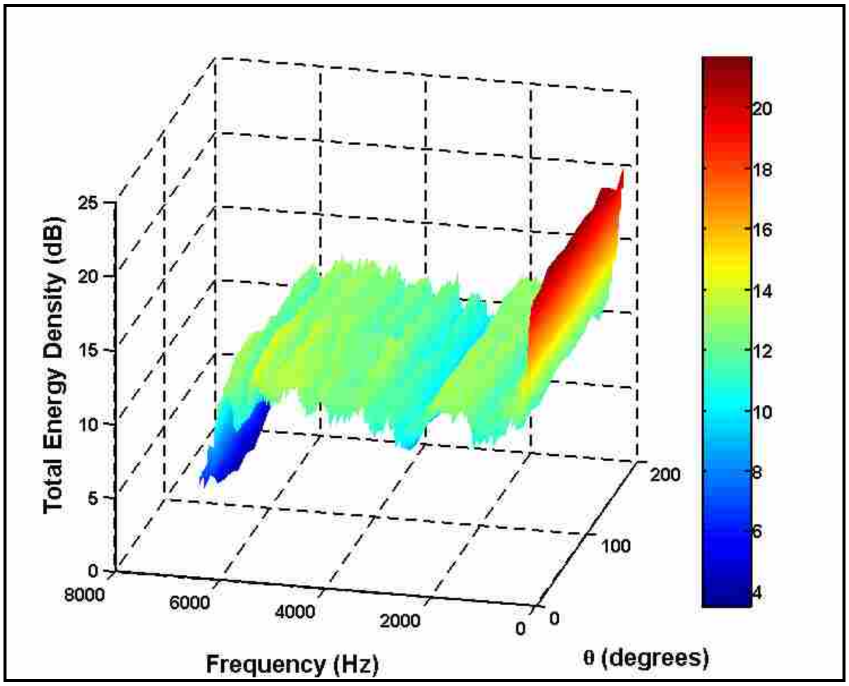

Figure 7–12: *l*-axis directivity results with correction function

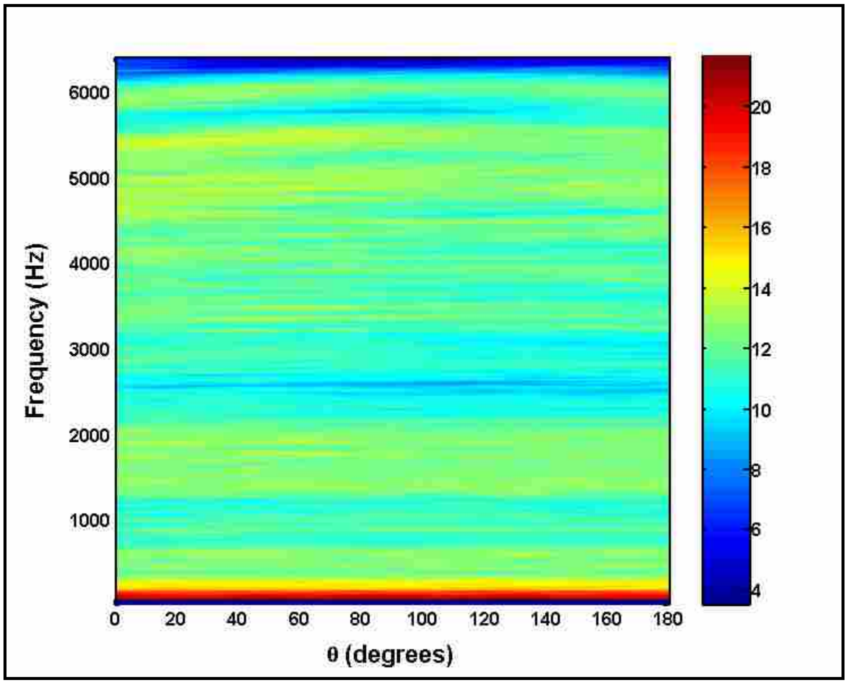

Figure 7–13: *l*-axis directivity results pseudo color plot

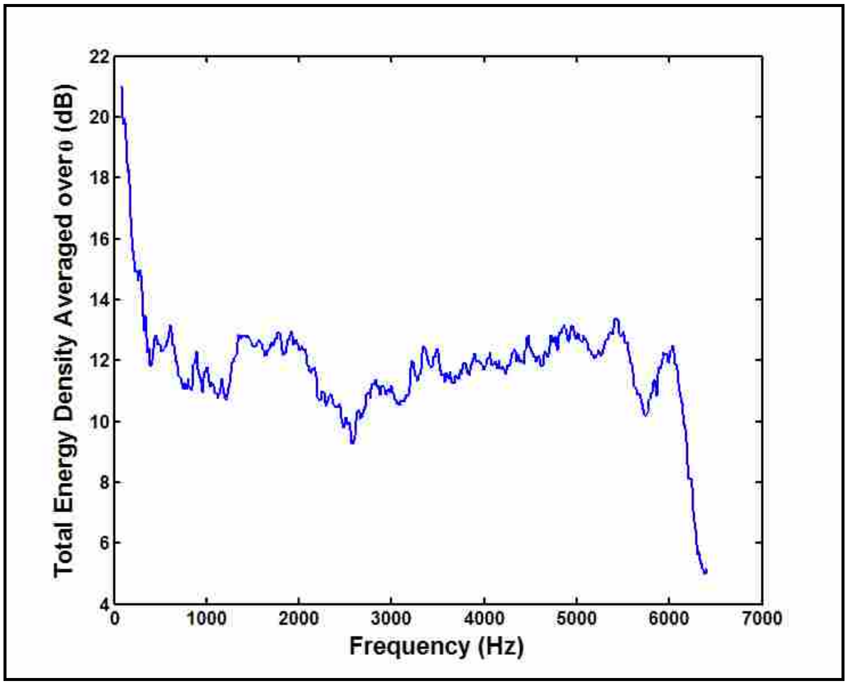

Figure 7–14: *l*-axis directivity results averaged over the rotation angle θ

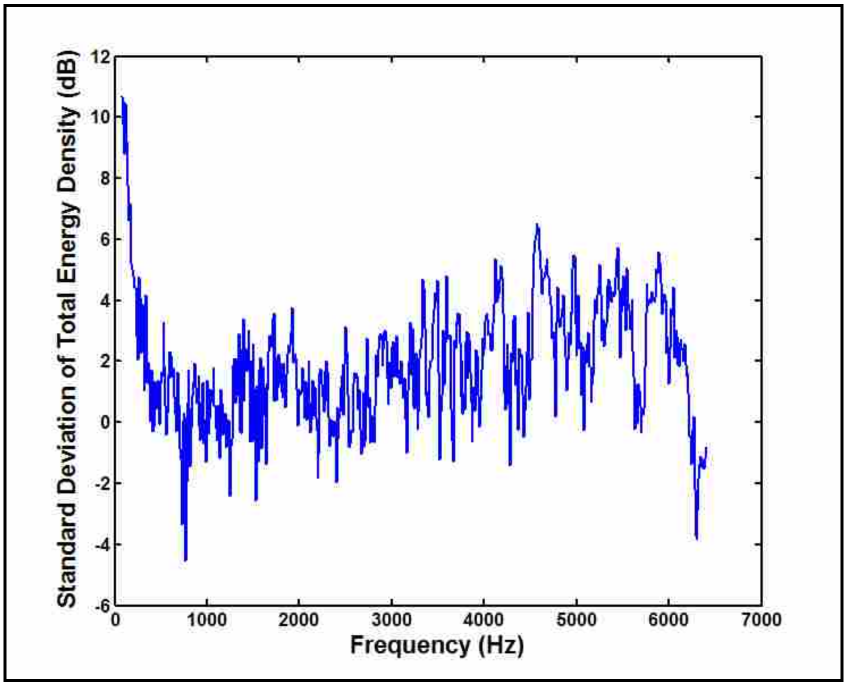

Figure 7–15: *l*-axis directivity standard deviation

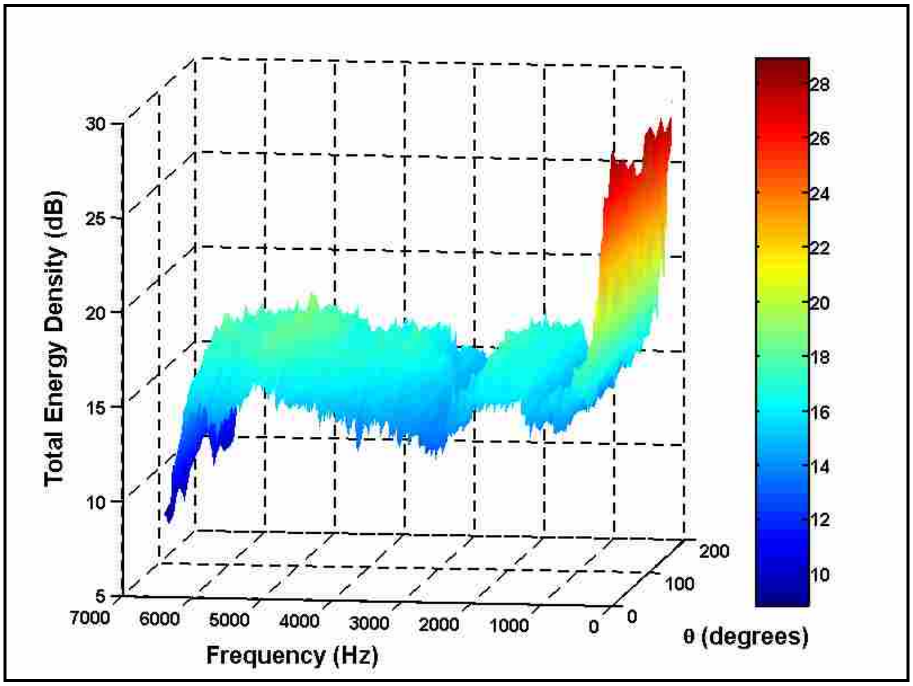

Figure 7–16: *m*-axis directivity results with correction function

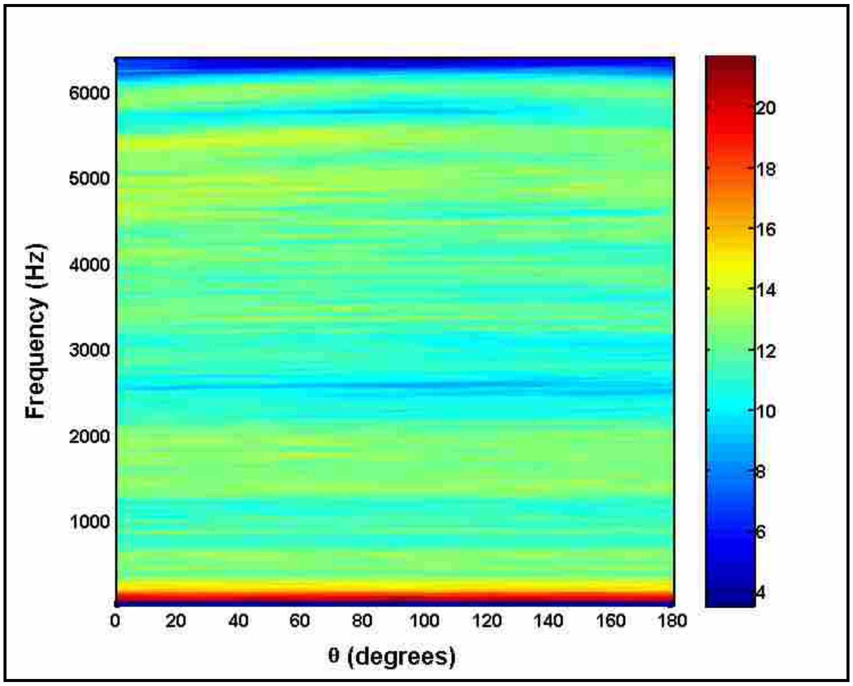

Figure 7–17: ***m*****-axis directivity results pseudo color plot**

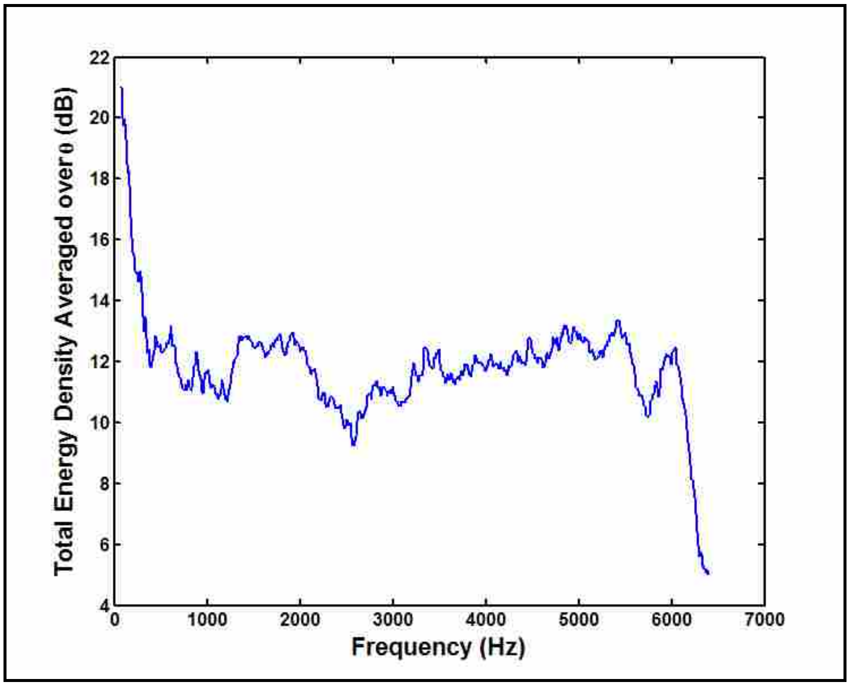

Figure 7–18: ***m*****-axis directivity results averaged over the rotation angle θ**

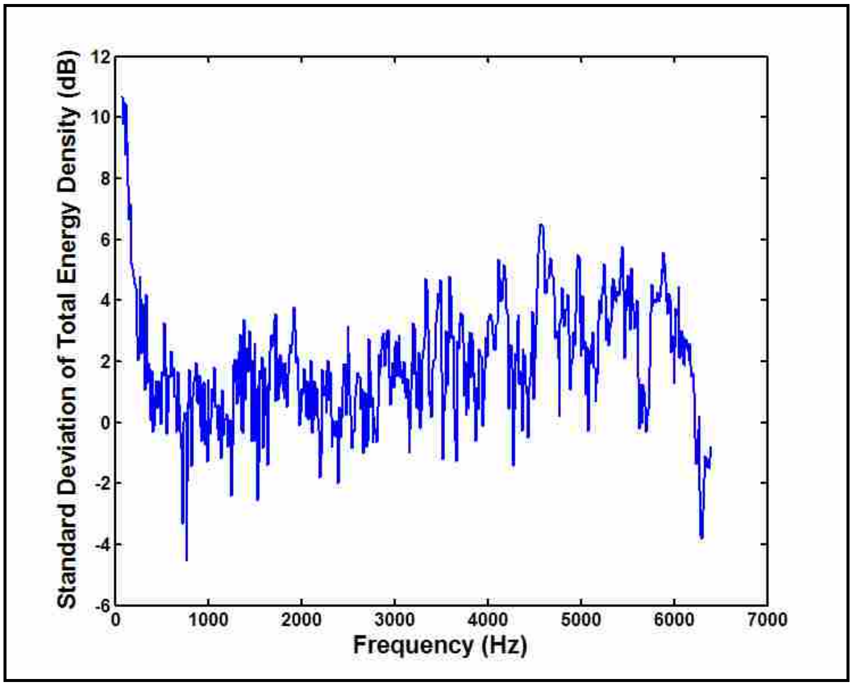

Figure 7–19: *m*-axis directivity standard deviation

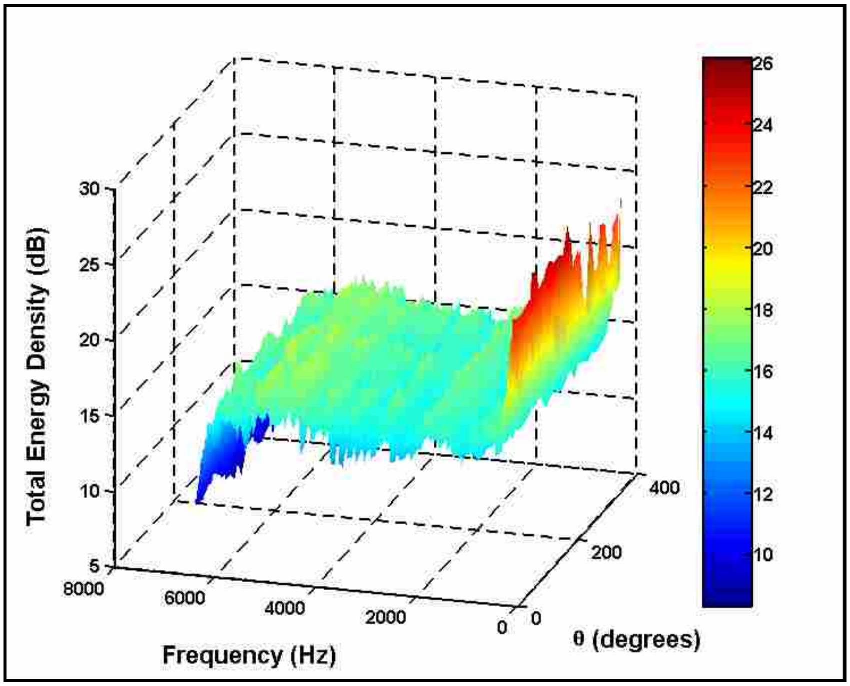

Figure 7–20: *n*-axis directivity results with correction function

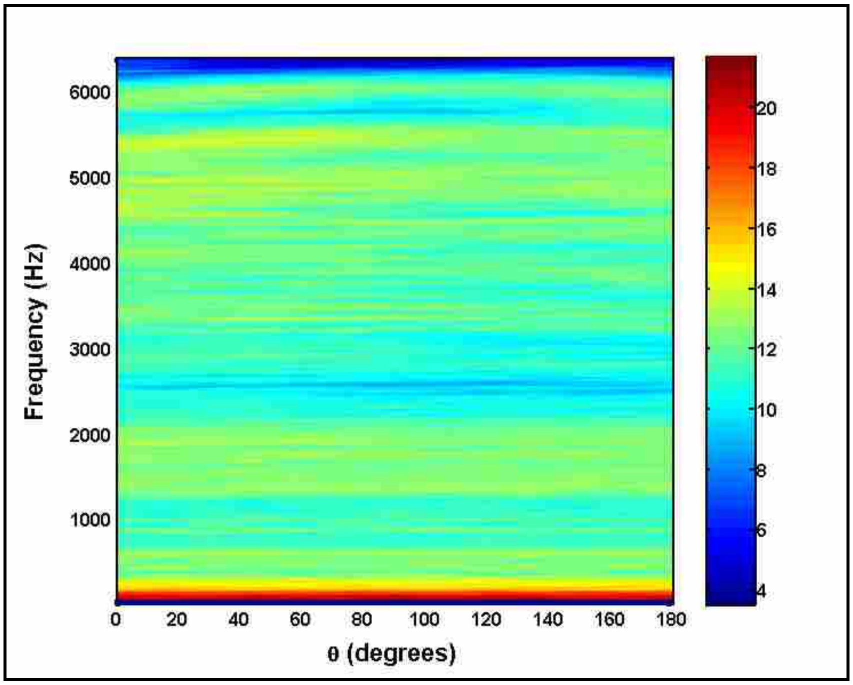

Figure 7–21: *n*-axis directivity results pseudo color plot

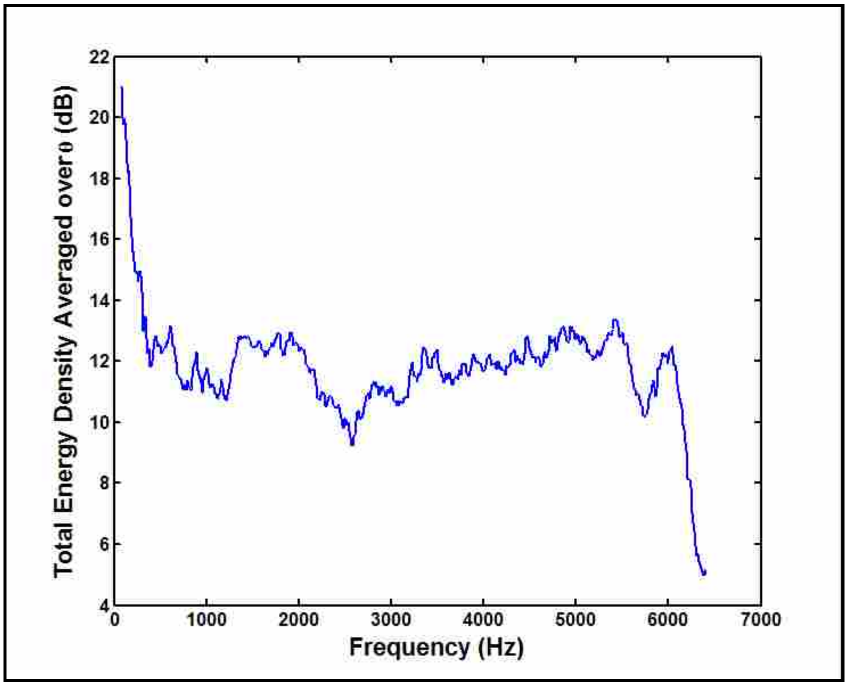

Figure 7–22: *n*-axis directivity results averaged over the rotation angle θ

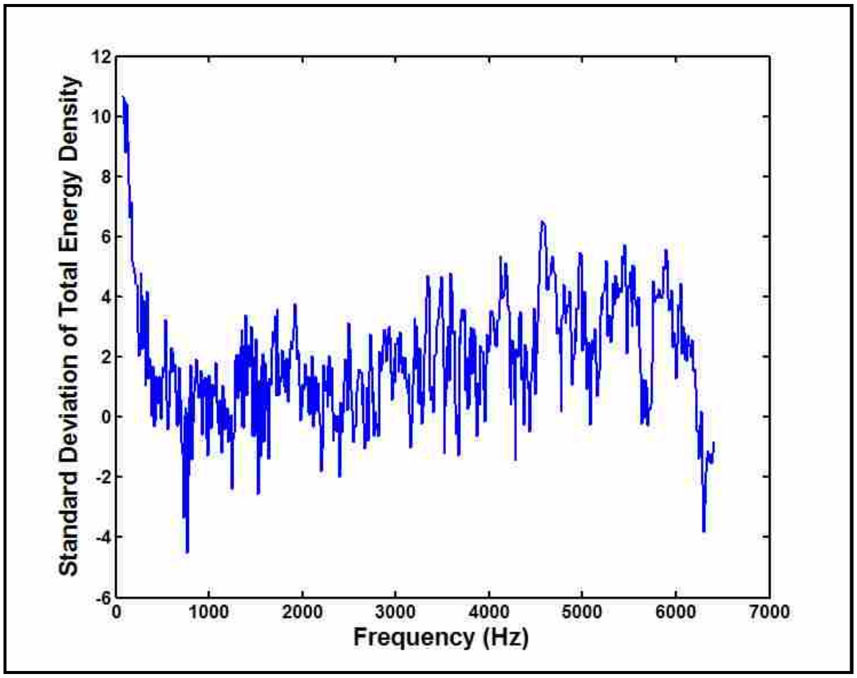

Figure 7–23: *n*-axis directivity standard deviation

7.4 MICROFLOWN COMPARISON

The orthogonal probe was calibrated using the calibrator. A ¼ inch GRASS microphone was used as the reference. The sensitivity of the probe microphones was obtained using the relative calibration technique discussed in chapter 2. The calibration curves used for the three side microphones are shown in Figure 7–24-Figure 7–26. The calibration curve for the pole microphone is shown in Figure 7–27. Each of the calibration curves are given in volts/Pascal and are presented up to the cutoff frequency of the fist cross mode (5000 Hz).

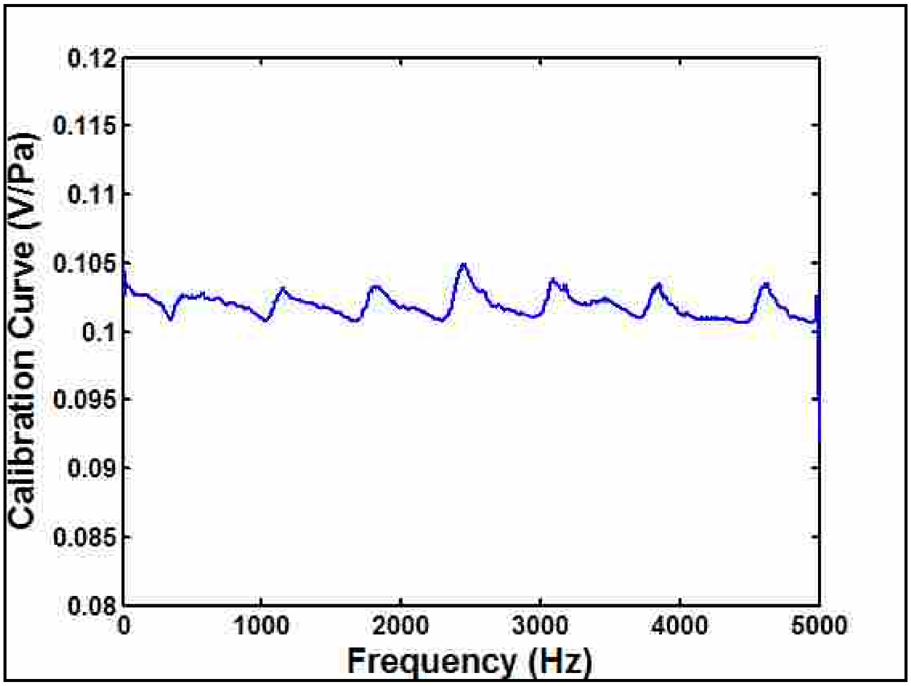

Figure 7–24 Calibration curve (side microphone)

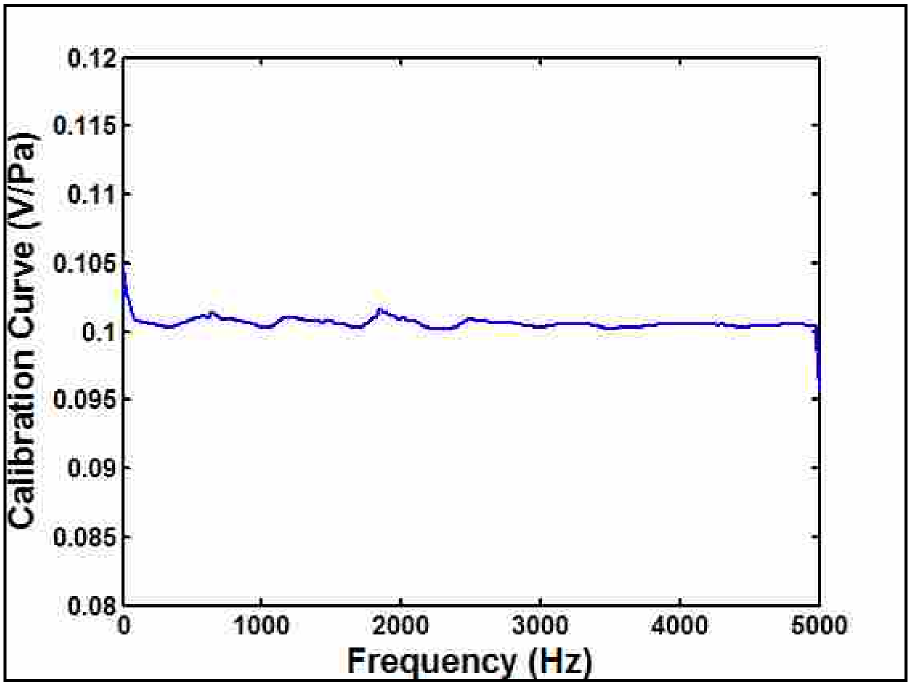

Figure 7–25: Calibration curve (side microphone)

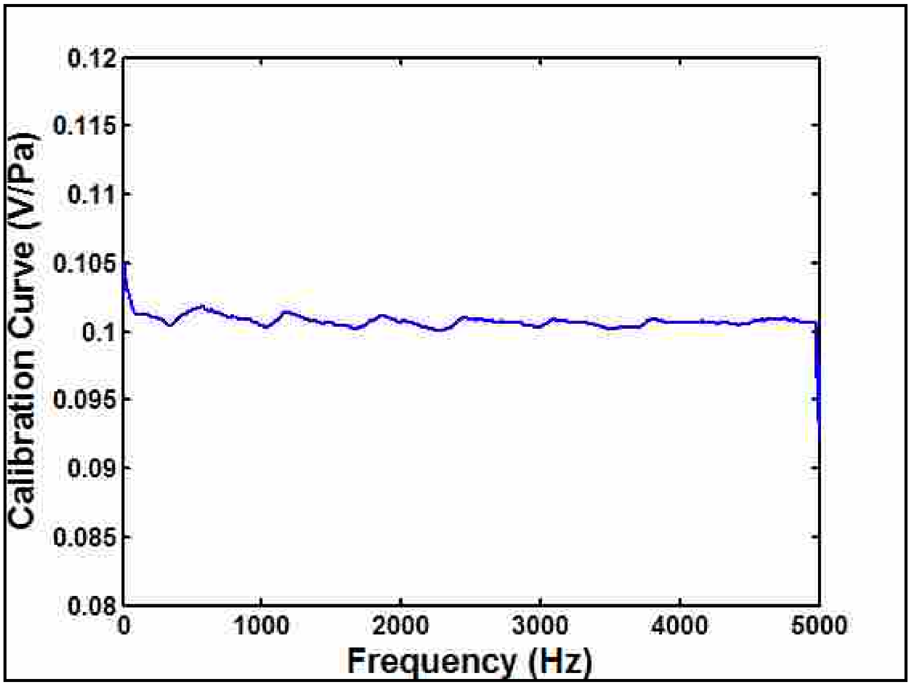

Figure 7–26: Calibration curve (side microphone)

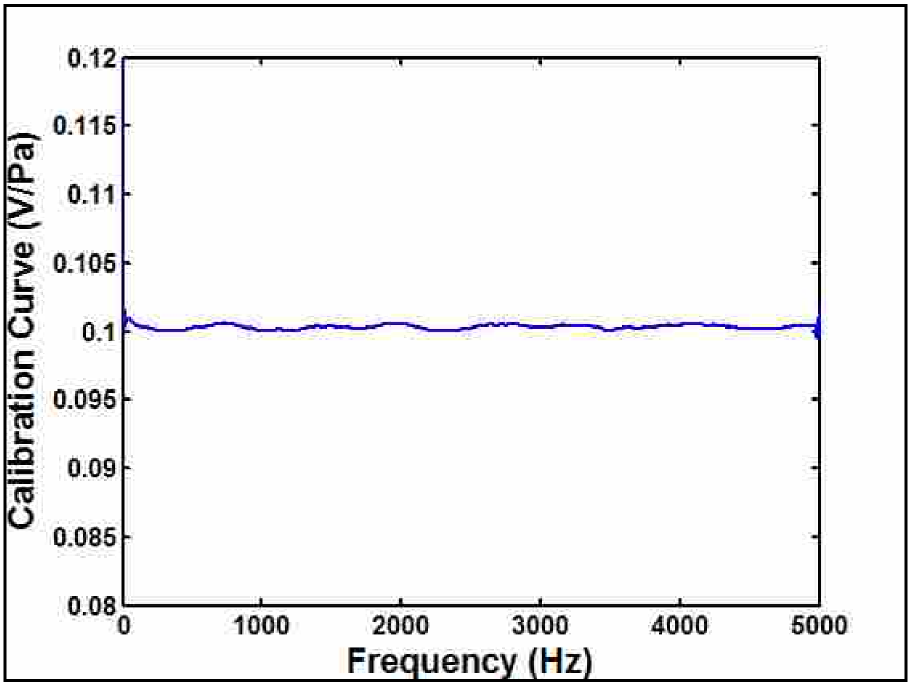

Figure 7–27: Calibration curve (pole microphone)

The orthogonal probe was place along side the Microflown probe in an anechoic environment. The probes were placed 4 m from a source. The source was excited with white noise from a signal generator. The four orthogonal probe measurements (all pressure) were recorded as a 20 second time history. Each second was averaged to obtain 20 averages. The calibration curves were applied to the averaged results. The calibrated results were used to calculate the total energy density. The four Microflown probe measurements (one pressure and three velocity measurements) were obtained using 20 averages. The published sensitivity values for each sensor were used to calibrate the results[21]. The results from both probes are shown in Figure 7–28.

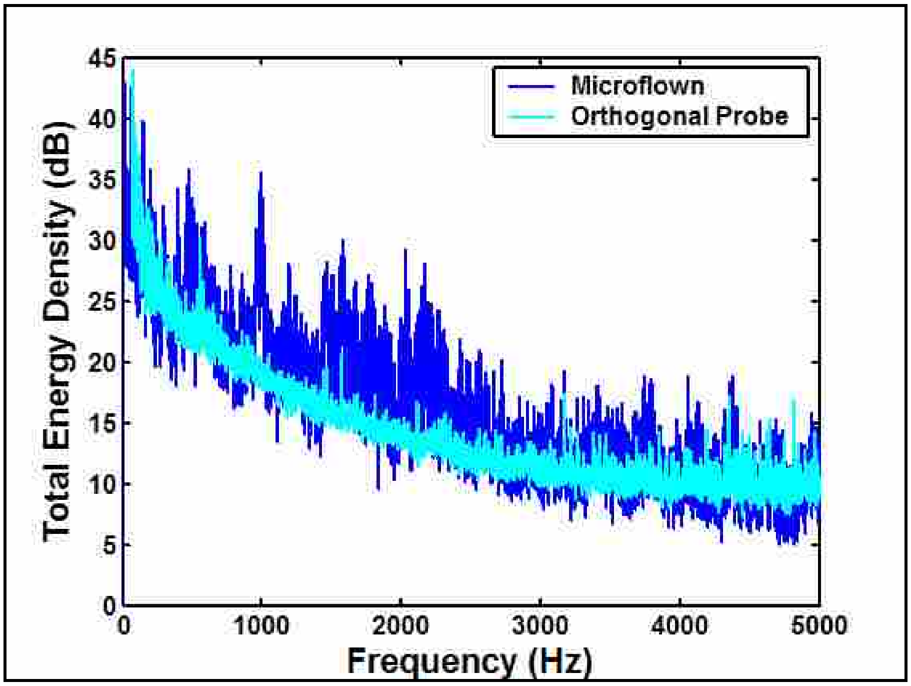

Figure 7–28: Orthogonal and Microflown probe comparison

The results agree very well up to 1000 Hz. The largest discrepancy occurs at 1000 Hz. This is likely due to a corner frequency of the Microflown that results from the spacing of the thin wires used to measure the particle velocity. The orthogonal probe results contain less variation than the Micrflown results. Further investigation into the limitations of the Microflown probe is beyond the scope of this research.

8 CONCLUSIONS

This chapter summarizes the work presented in this thesis. Recommendations and suggestions regarding future work are given. The publications associated with the work involved in this thesis are listed in chronological order.

8.1 SUMMARY

It has been shown that the calibrator can accurately calibrate four microphones within ±0.5 dB up to 2000 Hz, and within ±1dB up to 4900 Hz. The calibrator is designed for a specific probe, but the concept could easily be extrapolated to use on other probes with minor modification to the calibrator clamp described in Section 5.7. The concept could also be extrapolated to higher frequencies by decreasing the size of the driver tube. This would increase the cutoff frequency of the first higher order mode. A higher cutoff frequency would increase the bandwidth of the calibrator. With a higher cutoff frequency, the driver tube could limit the propagation to only plane waves. As long as only plane waves are present at the splitter the calibrator error will be minimal. The calibrator is adequate for the probe used in the validation process. Using this calibrator to calibrate this probe would result in a class 1 acoustic energy density probe.

In addition to the work done to calibrate multiple microphones simultaneously, the orthogonal probe used to validate the calibrator was directionally characterized. The error introduced in the velocity calculation can be eliminated using a correction function.

8.2 RECOMMENDATIONS FOR FUTURE RESEARCH

Future work involving the calibrator could include decreasing the radius of the driver tube. If the driver tube had a smaller radius the cutoff frequency of the first higher order mode would increase to a higher frequency. Increasing the cutoff frequency of the driver tube would increase the calibrator frequency range. The full calibrator model could be used to predict the frequency response. If the driver tube radius was decreased from 0.02 m to 0.015 m the cutoff frequency of the first higher order mode would be above 6600 Hz.

Further investigation could be done on the effect bending has on the receiver tubes. For example if tube one is bent what effect if any, does the bend have on the pressure results of tubes 2–5? The results from this type of study could be used to reduce the error, and expand the frequency range over which class 1 probe standards can be met.

It is recommended that the inserts be made with a larger termination diameter. This would allow for a larger o-ring to be mounted to the end of the insert. A larger o-ring would allow more flexibility in the microphone alignment inside the calibrator clamp. This would make the calibrator more user friendly. The effect of the new insert on the frequency response of the calibrator could be predicted using the model.

The calibrator clamp is probe specific, and limits the calibrator to certain probes. Future work involving a more universal calibrator clamp would greatly increase the usability of the calibrator. The calibrator would be much more universal if it could be used to calibrate probes with different microphone orientations, without separate probe-specific, calibrator clamps.

8.3 PUBLICATIONS

The work involved in this thesis was presented at the 12th annual Rocky Mountain NASA Space Grant Consortium Fellowship Symposium on May 8, 2006. A paper was printed in the Symposium proceedings. A presentation was also given at the Inter-Noise conference held December 3–6, 2006. A paper was printed in the conference proceedings. A journal paper on the work in this thesis has been submitted for publication in the Noise Control Engineering Journal.

9 REFERENCES

[1] C. M. Harris, *Handbook of Acoustical Measurements and Noise Control* (McGraw-Hill, New York, 1991).

[2] Y. Liu and F. Jacobsen, "Measurement of absorption with a p-u sound intensity probe in an impedance tube," J. Acoust. Soc. Am. **118**, 2117–2120 (2005).

[3] B.S. Cazzolato and J. Ghan, "Frequency domain expressions for the estimation of time-averaged acoustic energy density," J Acoust. Soc. Am. **117**, 3750–3756 (2005).

[4] P. M. Morse and K. U. Ingard, *Theoretical Acoustics*, pp. 258, 311–313 (McGraw-Hill Book Company, New York, 1968).

[5] B. M. Faber and S.D. Sommerfeldt, "Global active control of energy density in a mock tractor cabin," Noise Control Eng. J. **54**, 187–193 (2006).

[6] B. M Faber, *Thesis-(M.S.): Active minimization of acoustic energy density in a mock tractor cab*, Brigham Young University Department of Physics and Astronomy, 2004.

[7] S. D. Sommerfeldt, J. W. Parkins, and Y. C. Park, "Global Active Noise Control in Rectangular Enclosures," Proc. ACTIVE 95, (1995): pp. 477–488.

[8] M. C. Harris, *Thesis-(M.S.): Development of energy based nearfield acoustic holography system,* Brigham Young University Department of Mechanical Engineering, 2005.

[9] F. Jacobsen and Y. Liu, "Near field acoustic holography with particle velocity transducers," J. Acoust. Soc. Am **118**, 3139–3144 (2005).

[10] D. B. Nutter, *Thesis-(M.S.): Sound absorption and sound power measurements in reverberation chambers using energy density methods,* Brigham Young University Department of Physics and Astronomy, 2006.

[11] R. S. Figliola and D. E. Beasley, *Theory and Design for Mechanical Measurements*, 3rd ed. (Wiley, New York, 2000) pp. 13–20.

[12] L. E. Kinsler, A. R. Frey, A. B. Coppens, and J. V. Sanders, *Fundamentals of Acoustics*, 4th ed. (Wiley, New York, 2000).

[13] Brüel & Kjær Technical Review, “Low Frequency Calibration of Acoustic Measurement Systems. Calibration and Standards. Vibration and Shock Measurements,” No. 4-1981.

[14.]T. W. Leishman, *Physics 562 Class Notes: Applied Acoustics*, Brigham Young University Department of Physics and Astronomy, 2005.

[15] R. B. Bobber, *Underwater Electroacoustic Measurements* (Naval Research Laboratory, Washington, 1970).

[16] D. R. Yntema, W. F. Druyvesteyn, and M. Elwenspoek, “A four particle velocity sensor device,” J. Acoust. Soc. Am. **119**, 943–951 (2006).

[17] J. W. Parkins, S. D. Sommerfeldt, and J. Tichy, “Narrowband and broadband ActiveControl in an enclosure using the acoustic energy density,” J. Acoust. Soc. Am. **108**, 192–203 (2000).

[18] J. W. Parkins, S. D. Sommerfeldt, and J. Tichy, “Error analysis of a practical energy density sensor,” J. Acoust. Soc. Am. **108** 211–222 (2000).

[19] J. Ghan, B.S. Cazzotato, and S.D. Snyder, “Expression for the estimation of time-averaged acoustic energy density using the two-microphone method (L),” J. Accoust. Soc. Am. **113**, 2404–2407 (2003).

[20] L. L. Locey, *Thesis-(M.S.): Analysis and comparison of three acoustic energy density probes*,: Brigham Young University Department of Physics and Astronomy, 2004.

[21] Microflown Technologies B.V. “Microflown Ultimate Sound Probe (USP) model Z” (version 1.3, 2002), www.microflown.com

[22] G. W. Elko, “An acoustic vector-field probe with calculable obstacle bias, “ Proc. Noise-Con 91, pp.525–532 (July 1991).

[23] R. Raangs, T. Schlicke, and R. Barham, “Calibration of a micromachined particle velocity microphone in a standing wave tube using a LDA photon-correlation technique,” Meas. Sci. Technol. **16** 1099–1108 (2005).

[24] F. Jacobsen and V. Jaud, “A note on the calibration of pressure-velocity sound intensity probes”, J. Acoust. Soc. Am. **120** 830–837 (2006).

[25] J. W. Parkins, *Thesis-(Ph.D.): Active minimization of energy density in a three-dimensional enclosure,* The Pennsylvania State University Department of Acoustics, 1998.

[26] A. D. Pierce, Acoustics an Introduction to Its Physical Principles and Applications, (Acoustical Society of America, New York, 1989).

[27] L. L. Beranek, *Acoustics,* (Acoustical Society of America, New York, 1996).

[28] T. W. Leishman, *Thesis-(Ph.D.): Active Control of Sound Transmission through Partitions Composed of Discretely Controlled Modules*, The Pennsylvania State University Department of Acoustics, 2000.

[29] N. Solokhin, "Basic types of discontinuity in circular acoustic wave guide," J. Acoust. Soc. Am. **114** 2626–2632 (2003).

[30] S. K. Lee, B. R. Mace, and M. J. Brennan, "Wave propagation, reflection and transmission in non-uniform one-dimensional waveguides," J. Sound Vib. **304** 31–49 (2007).

[31] F. C. Karal, "The analogous acoustical impedance for discontinuities and constrictions of circular cross section," J. Acoust. Soc. Am. **25** 327–334 (1953).

[32] G. Rizzoni, *Principles and Applications of Electrical Engineering,* (McGraw-Hill Book Company, New York, 2004).

[33] M. W. Thompson and W. J. Strong, "Inclusion of wave steepening in a frequency-domain model of trombone sound production," J. Acoust. Soc. Am. **110** 556–562 (2001).

[34] D. D. Rife, "MLSSA SPO (Speaker Parameter Option)" reference manual version 4WI Rev 8, DRA Laboratories 2005.

[35] R. M. Aarts and A. J. E. M. Janssen, "Approximation of the Struve function H_1 occurring in impedance calculations," J. Acoust. Soc. Am. **113** 2635–2637 (2003).

[36] J. Lawson and J. Erjavec, *Modern Statistics for Engineering and Quality Improvement* (Duxbury California, 2001).

APPENDIX A: CAD DRAWINGS

This Appendix shows all of the calibrator component drawings. The dimensions of the drawings are all in mm. All of the parts were manufactured specifically for the calibrator with the exception of the loudspeaker, which was purchased.

A.1 DRIVER DRAWING

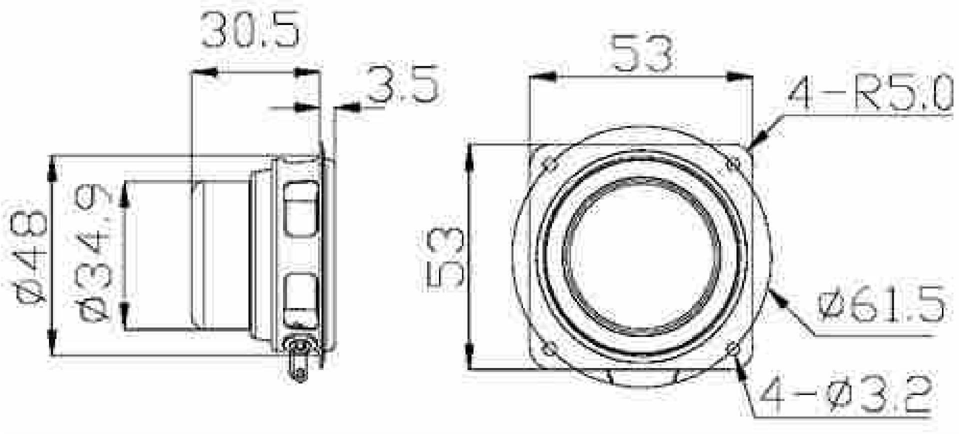

Figure A–1: HiVi A2S drawing

A.2 COUPLER DRAWING

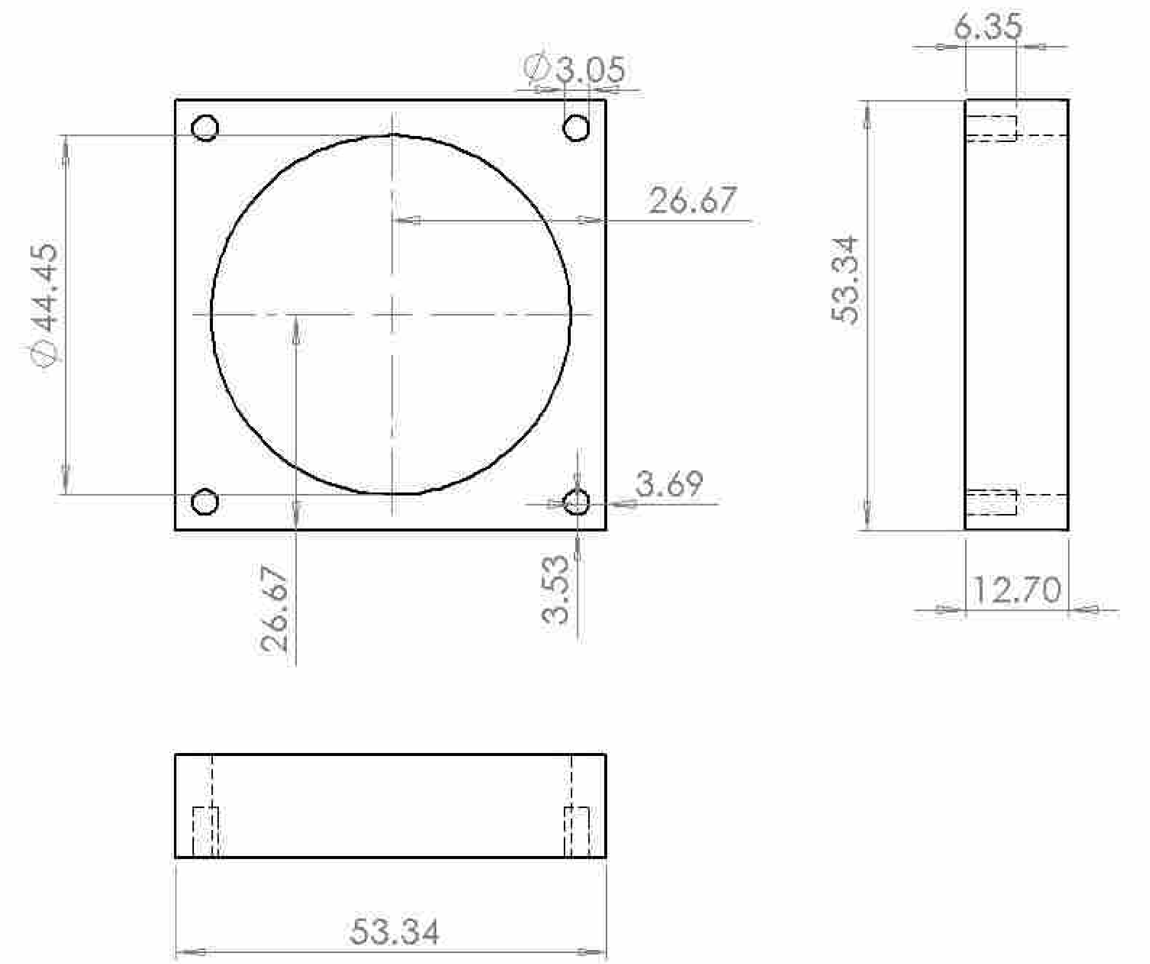

Figure A–2: Coupler CAD drawing

A.3 DRIVER TUBE DRAWING

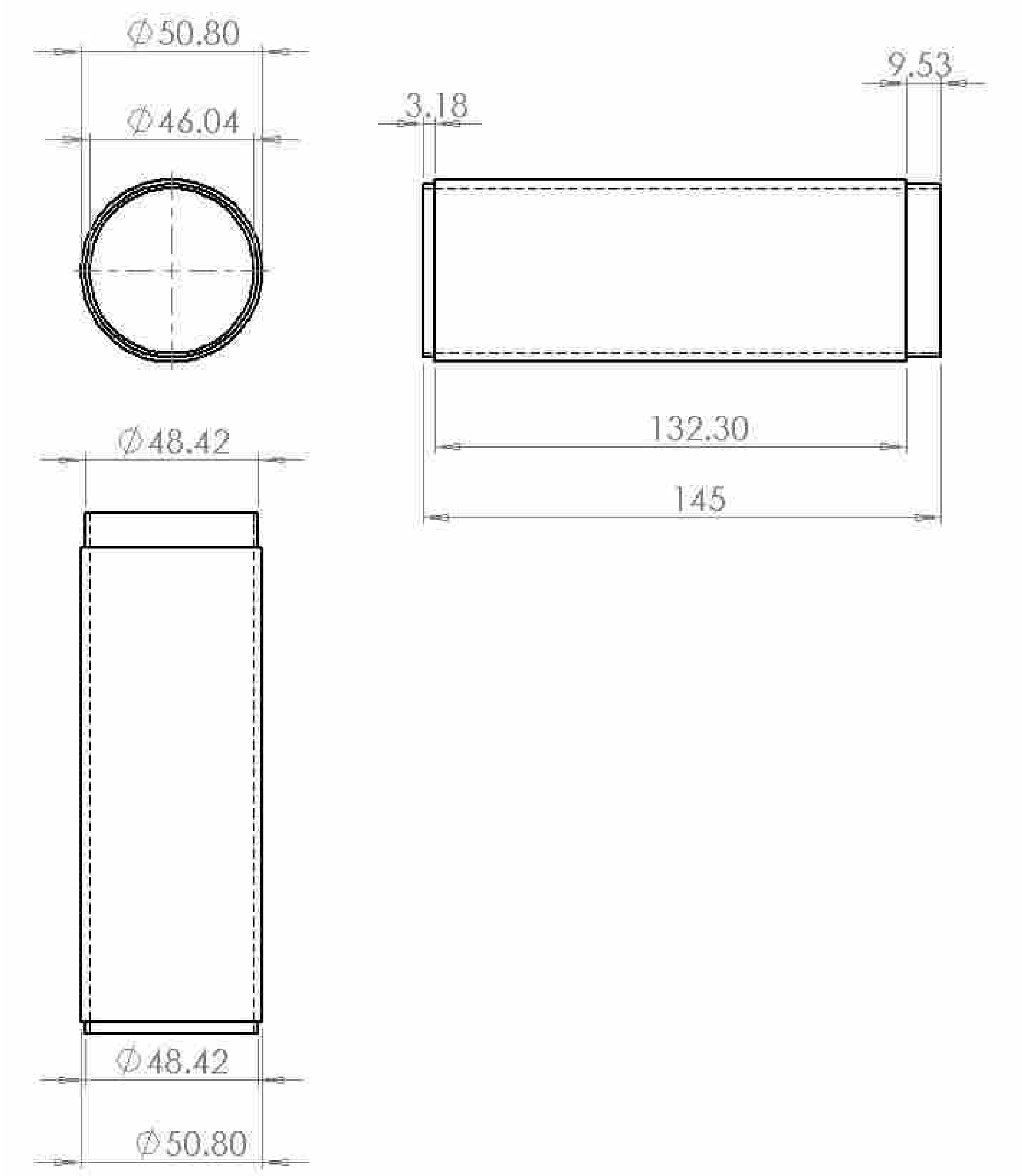

Figure A–3: Driver tube CAD drawing

A.4 SPLITTER DRAWING

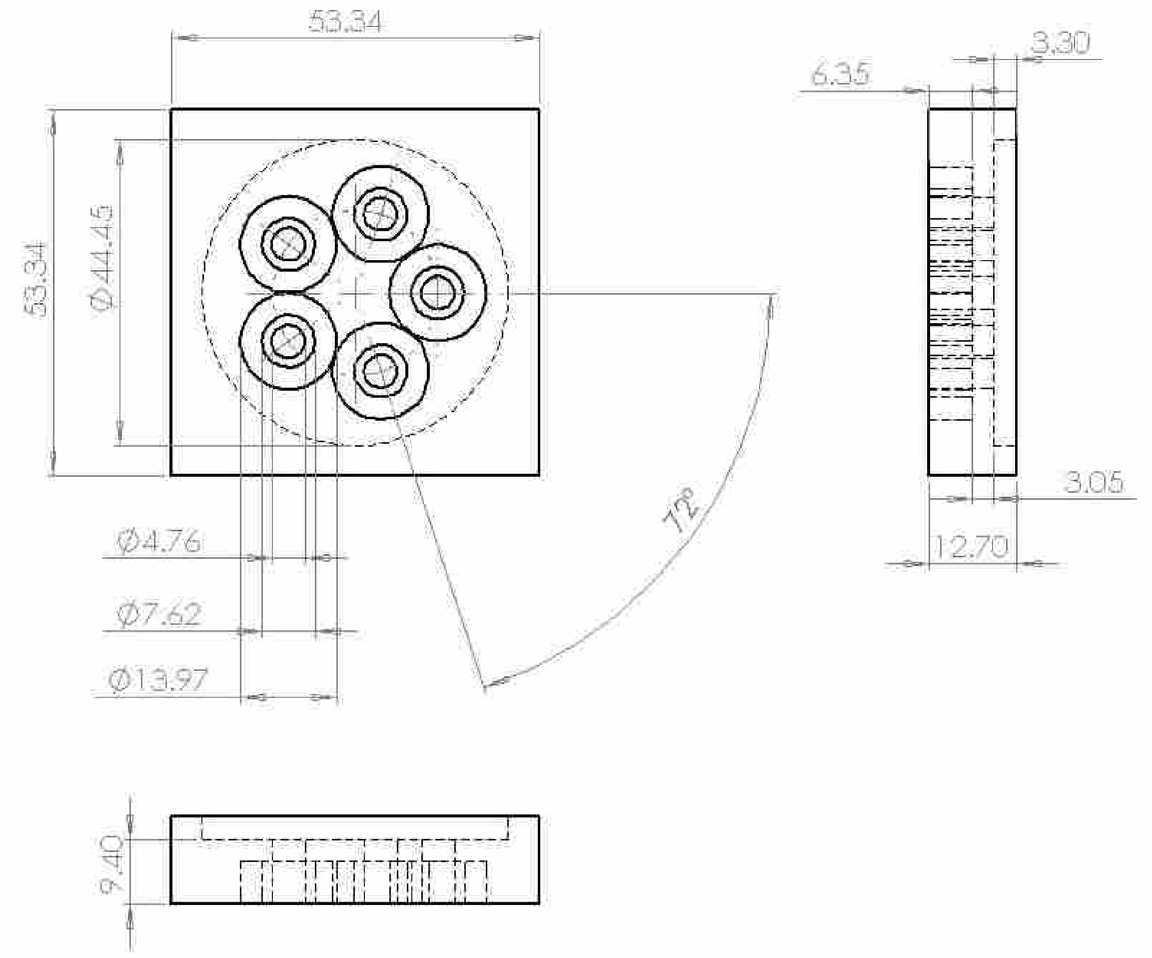

Figure A–4: Splitter CAD drawing

A.5 RECEIVER TUBE DRAWING

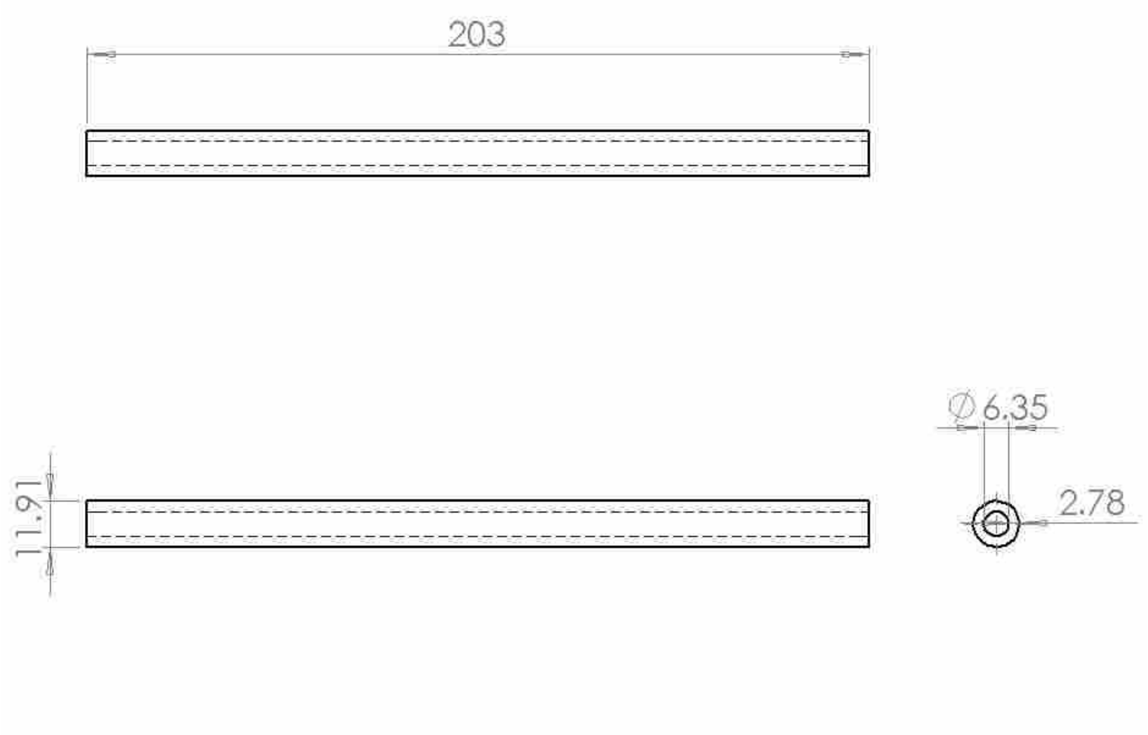

Figure A–5: Receiver tube CAD drawing

A.6 INSERT DRAWING

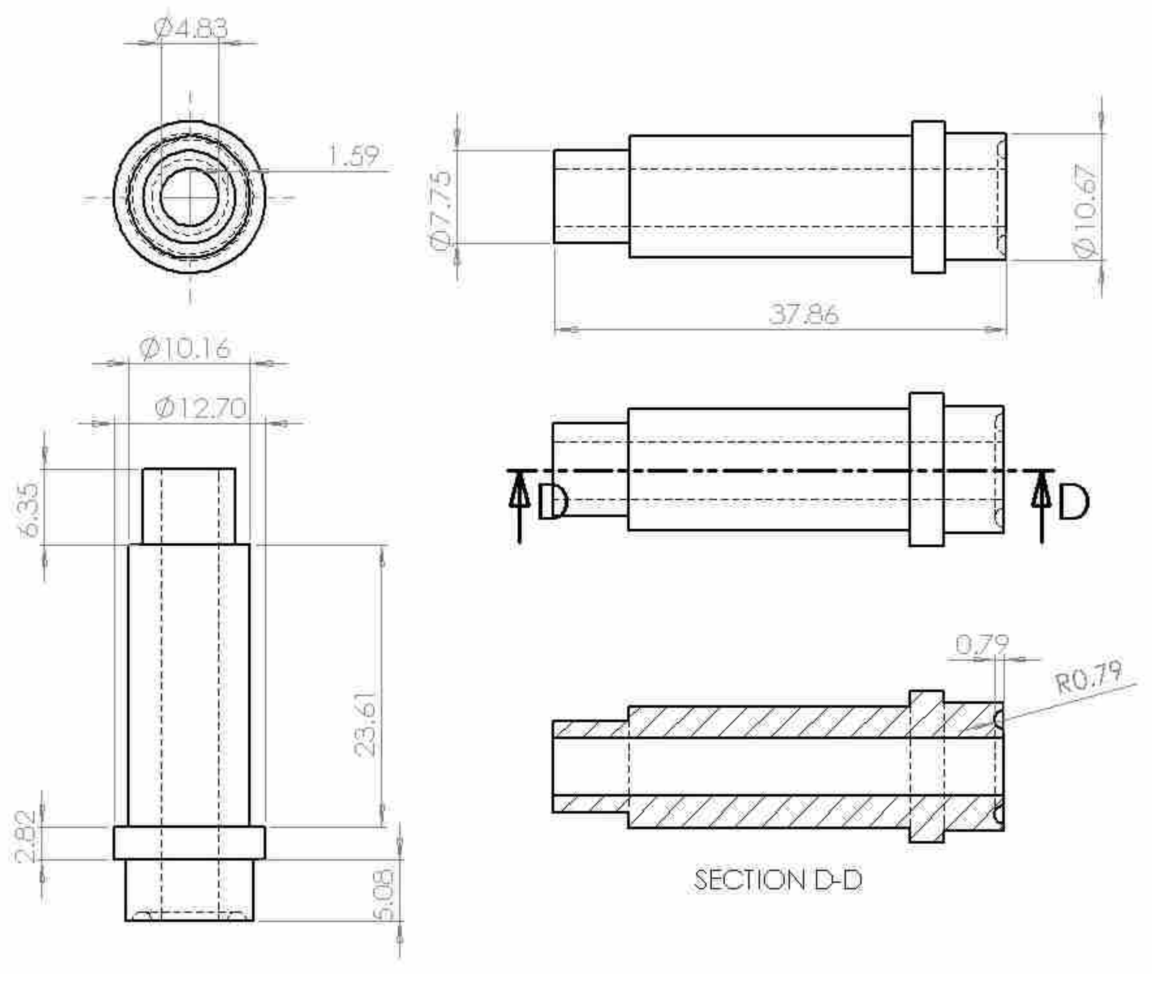

Figure A–6: Insert CAD drawing

A.7 BOLT DRAWING

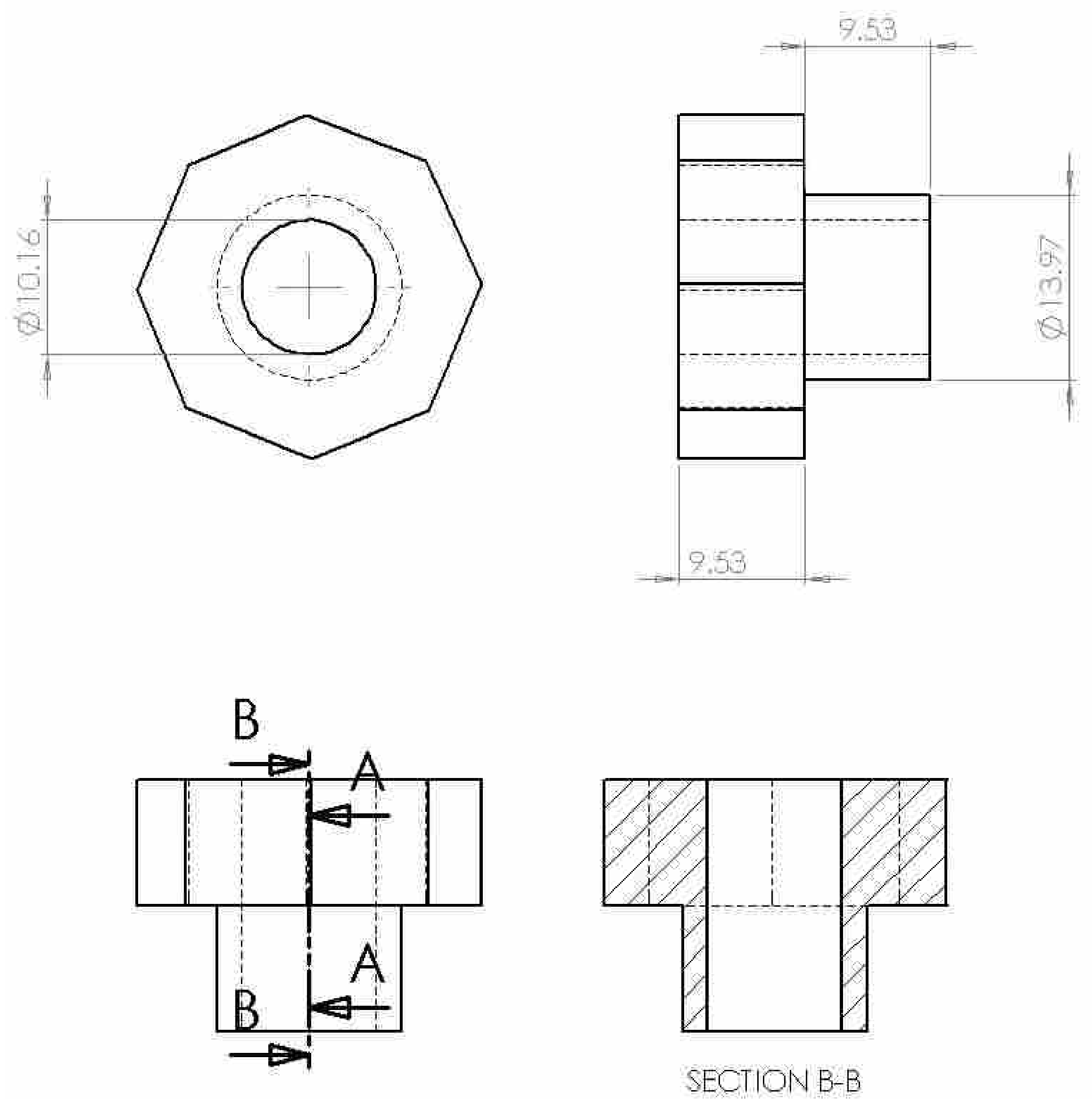

Figure A–7: Bolt CAD drawing

A.8 BOTTOM HALF OF CALIBRATOR CLAMP DRAWING

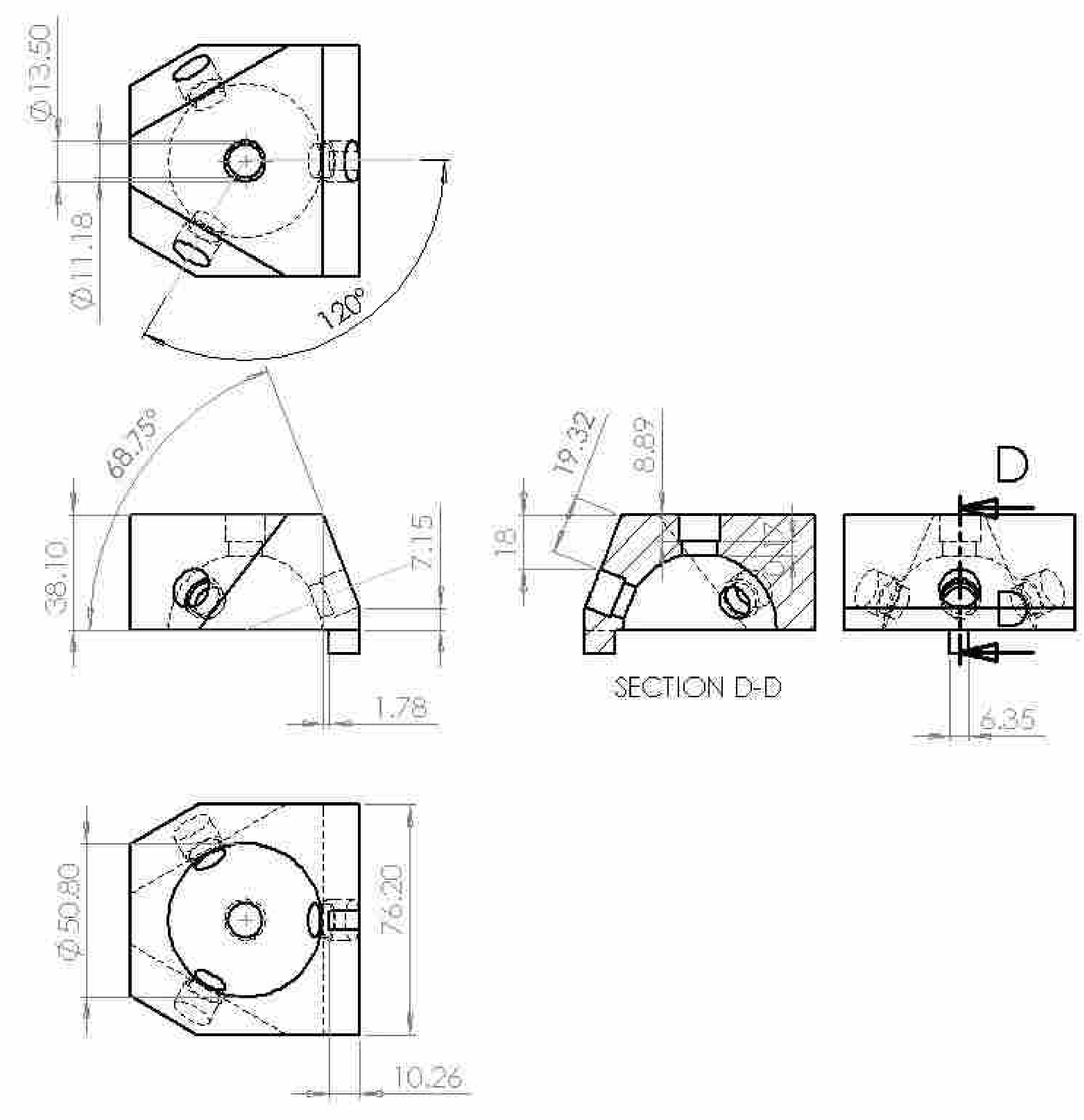

Figure A–8: Bottom half of calibrator clamp CAD drawing

A.9 TOP HALF OF CALIBRATOR CLAMP DRAWING

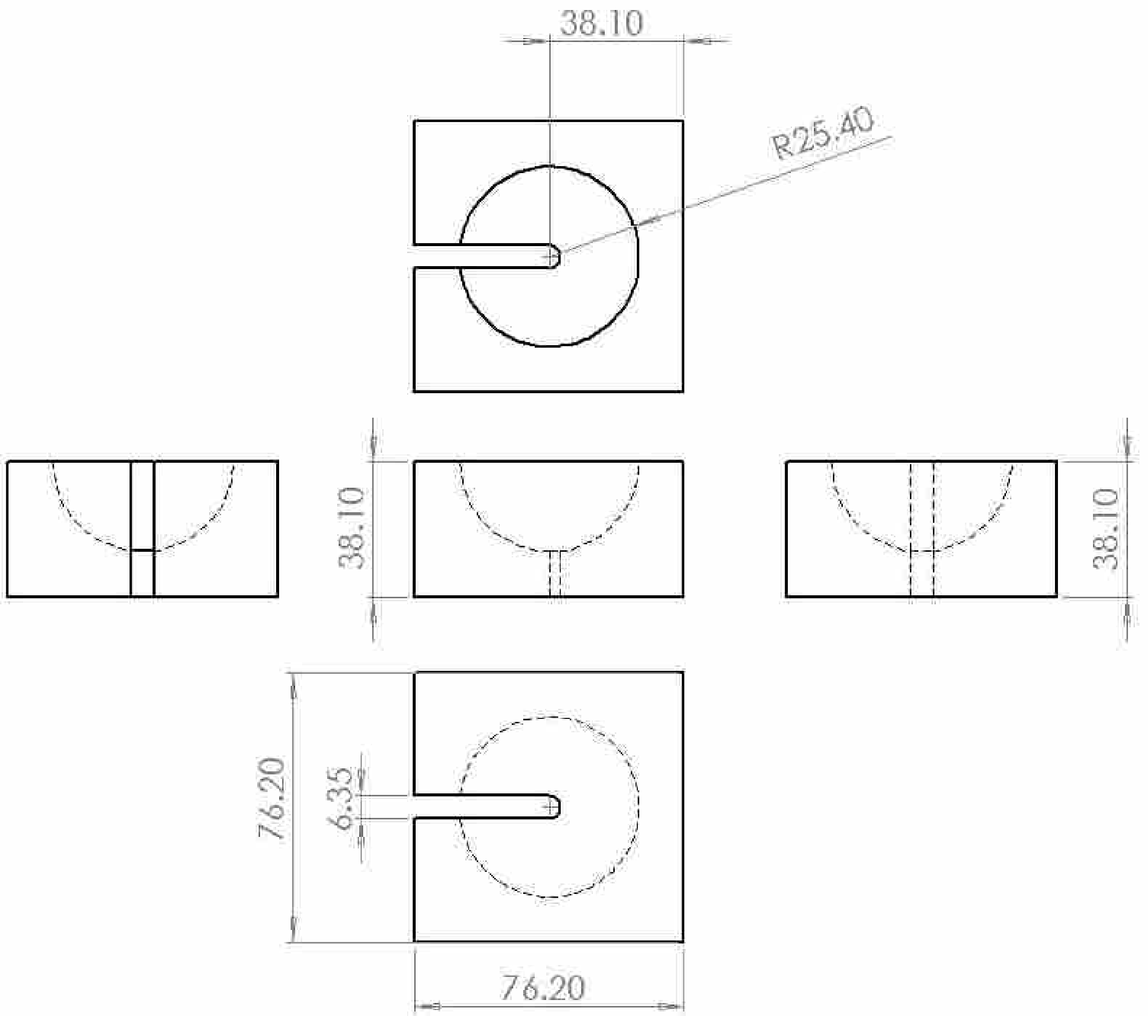

Figure A–9: Top half of calibrator clamp CAD drawing

A.10 CLAMP LATCH

The latches were ordered from McMaster Carr. The model number of the latch is 1889A34. The overall length is 0.048 m, the width is 0.036 m, and the height is 0.013 m.

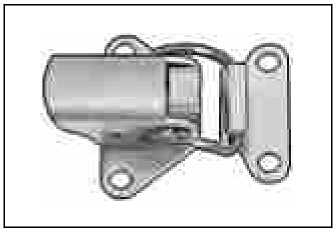

Figure A–10: Calibrator clamp latch

APPENDIX B: CALIBRATOR USE GUIDE

Insert the probe into the calibrator clamp as shown in Figure B–11.

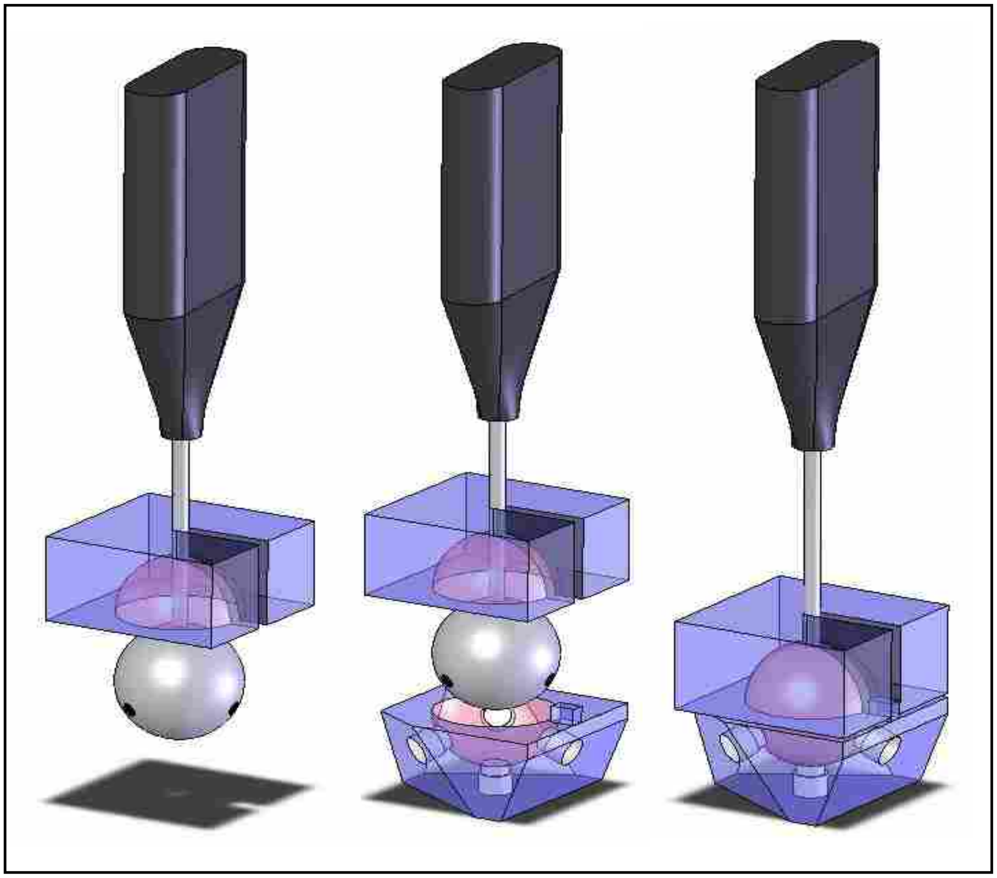

Figure B–11: Calibrator clamping process

Make sure the probe microphones are aligned with the microphone ports as shown in Figure B–12

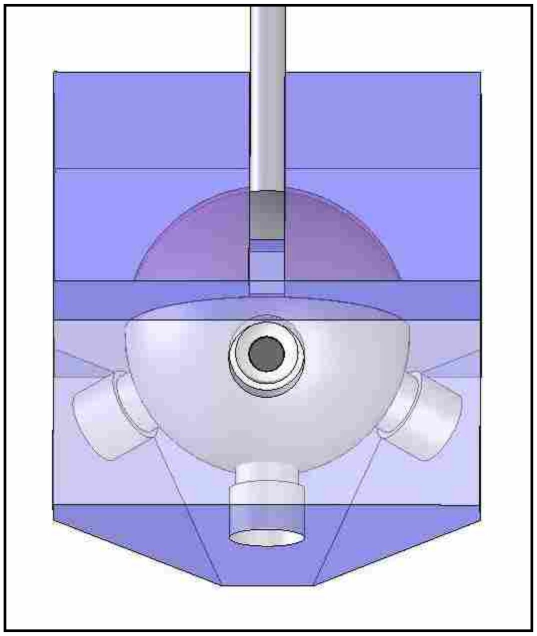

Figure B–12: Microphone alignment

After the microphones are aligned use the latches to hold the clamp halves together.

WARNING: If the microphones are not properly aligned the calibration will be inaccurate.

One method used to ensure a tight seal is to cut a hole just large enough to expose the microphone diaphragm in a piece of electrical tape. Place the tape over the microphone so the hole allows the microphone diaphragm to be exposed. Proceed with the calibration.

CAUTION: Be careful not to remove felt cover when removing tape.

Place the inset in to each port as shown in Figure B–13. Make sure the o-ring is present in the end of the insert. Constrain each insert with a bolt as shown in Figure B–14.

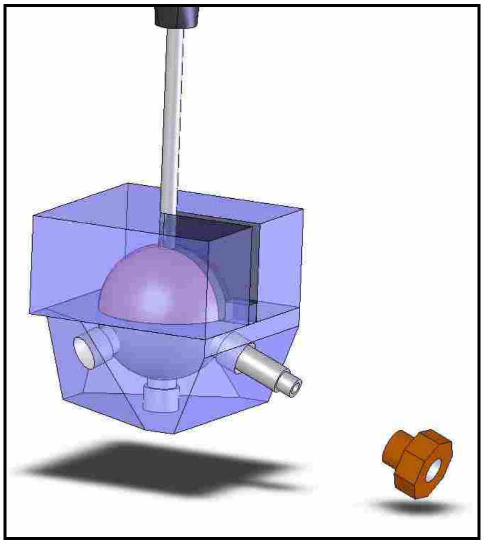

Figure B–13: Insert placement

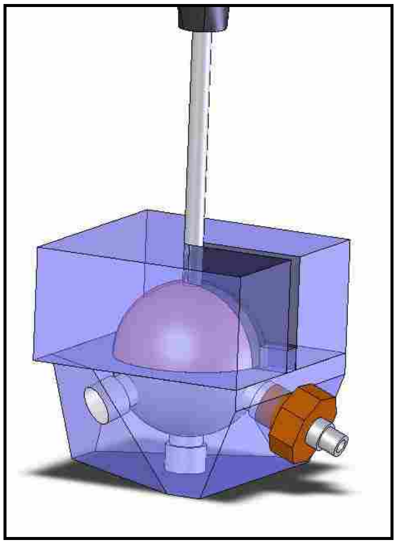

Figure B–14: Bolt placement

Once all the inserts are in place as shown in Figure B–15, evenly tighten each bolt.

CAUTION: DO NOT OVERTIGHTEN!

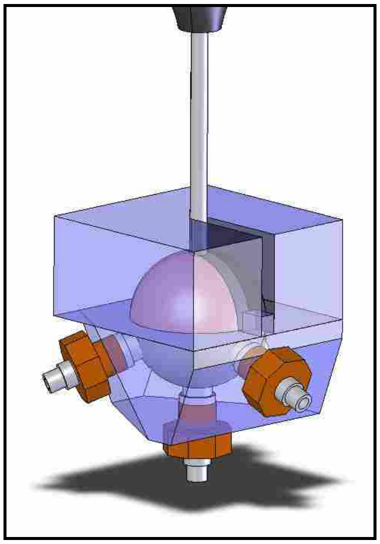

Figure B–15: All inserts and bolts in place

Obtain the sensitivity of the reference microphone. This is simply done using a commercially available calibrator (see Low Frequency technique described in Chapter 2).

Connect a receiver tube to each one of the inserts as shown in Figure B–16. Make sure the receiver tube is fully pushed onto the insert and the splitter ports. The reference microphone is connected to the fifth receiver tube as shown in Figure B–16. The reference microphone is connected to the insert by a short piece of tubing. This piece of tube is the same diameter as the receiver tubes. Make sure the reference microphone is inserted into the tube until the grid cap is touching the insert. The insert in the reference receiver tube does not have an o-ring, because the seal around the reference microphone is provided by the tube used to connect the microphone to the insert.

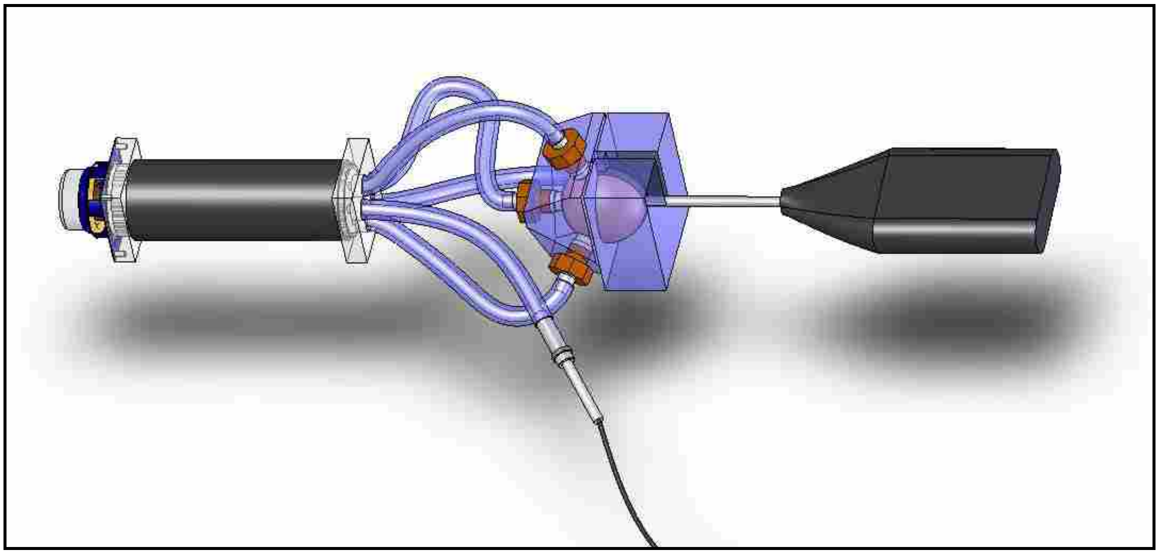

Figure B–16: Ready to calibrate

Obtain the sensitivity of each of the probe microphones relative to the reference microphone. This is done using the substitution technique outlined in Chapter 2.s

APPENDIX C: MATLAB CODE

C.1 CIRCUIT MODEL CODE

C.1.3 full_circuit_model.m

```
%%%%%%%%%%%%%%%%%%%%%%%%%%%%%%%%%%%%%%%%%%%%%%%%%%%%%%%%%%%%%
% This file numerically evaluates a circuit model of the    %
% entire calibration. In the model the waveguides are       %
% included along with the actual driver.                    %
%                                                           %
%                                                           %
% This model is referred to as the Entire calibrator        %
% circuit model, it includes the actual driver in the       %
% model.                                                    %
%%%%%%%%%%%%%%%%%%%%%%%%%%%%%%%%%%%%%%%%%%%%%%%%%%%%%%%%%%%%%


clear all;
clc;
warning off MATLAB:divideByZero

% Properties of air -----------------------------
rho = 1.21; %kg/m^3    Density
c = 340; %m/s          Wave speed
gamma = 1.402;      %  Ratio of Specific Heats
eta = 1.82e-5; %Pa s   Coefficient of Shear Viscosity
Cp = 1.01e3; %J/kg K   Specific Heat
K = 0.0263; %W/m K     Thermal Conductivity
Pr = 0.710; %          Prandtl Number

% Frequency and Wavenumber---------------
f = 0:6400; %Hz
w = 2*pi*f; %rad/s
k = w/c;

% Driver Plane Wave Tube Parameters-------
ab = 0.02; %m
Sb = pi*ab^2 ; %m^2
Lb = 0.145; %m
```

```
% Splitter Hole Parameters------------------
ap = 0.00238; %m
Sp = pi*ap^2; %m^2
Lp = 0.00940+8*ap/(3*pi)*(.83+.1); %m

% Receiver Tube Parameters--------------
ac = 0.003175; %m
Sc = pi*ac^2 ; %m^2
Lc = 0.188+8*ac/(3*pi)*.8; %m

%Insert Parameters------------------
ai = 0.00242; %m
Si = pi*ai^2; %m^2
Li = 0.03786+8*ai/(3*pi)*.15+2*ai; %m


% Classical Absorption Coefficient-------
alpha_c = w.^2./(2.*rho.*c^3).*(4/3.*eta+(gamma-1).*K/Cp);

% Wall Losses Absorption Coefficient-----
alpha_wb = 1./(ab.*c).*sqrt(eta.*w./(2.*rho)).*(1+(gamma-1)/sqrt(Pr));
alpha_wp = 1./(ap.*c).*sqrt(eta.*w./(2.*rho)).*(1+(gamma-1)/sqrt(Pr));
alpha_wc = 1./(ac.*c).*sqrt(eta.*w./(2.*rho)).*(1+(gamma-1)/sqrt(Pr));
alpha_wi = 1./(ai.*c).*sqrt(eta.*w./(2.*rho)).*(1+(gamma-1)/sqrt(Pr));

% Total Thermoviscous Absorption Coefficient
alpha_tb = alpha_c+alpha_wb;
alpha_tp = alpha_c+alpha_wp;
alpha_tc = alpha_c+alpha_wc;
alpha_ti = alpha_c+alpha_wi;

% Tube Acoustic Wave numbers------------
kb = k-j.*alpha_tb;
kp = k-j.*alpha_tp;
kc = k-j.*alpha_tc;
ki = k-j.*alpha_ti;

kb = kb +.01-j.*.4;
kc = kc +.05-j.*.05;
ki = ki +.005-j.*.05;
kp = kp +.5-j.*.5;

% Actual Driver Parameters Measured with MLSSA
Sd = .0013; %m2
a = sqrt(Sd./pi); %radius of diaphragm (m)
Fs = 268.03; %free-air resonance (from MLSSA)
Qms = 6.5686; %(from MLSSA)
Mms = 0.0021454; %kg (from MLSSA)
Cms = 0.0001645; %m/N (from MLSSA)
Bl = 2.7247; %Tm (from MLSSA)

eg = 2.83; %input voltage at terminals
Re = 6.2489; %ohms (from MLSSA)
L1 = 0.0000892; %H (from MLSSA)
L2 = 0.00013; %H (from MLSSA)
R2 = 7.4425; %ohms (from MLSSA)
```

```
% % Published Parameters Hi-vi website
% Fs = 153; %free-air resonance
% Qms = 7.33;
% Mms = 0.0015;
% Cms = 0.000707; %m/N
% Bl = 2.5; %Tm
% Re = 6.5; %ohms

Mmd = Mms-8/3.*rho.*a^3;
Rms = 1/(2.*pi.*Fs.*Cms.*Qms);
Ze = Re + j.*w.*L1 + j.*w.*L2.*R2./(R2+j.*w.*L2);
Zad = Bl^2./(Ze.*Sd^2)+Rms./Sd^2+1./(j.*w.*Cms.*Sd^2)+j.*w.*Mmd./Sd^2;
% Zad =
eg*Bl^2./(Ze.*Sd^2)+Rms./Sd^2+1./(j.*w.*Cms.*Sd^2)+j.*w.*Mmd./Sd^2;

% Back side of Driver Approximated as a Baffled Piston
ka = k.*a;
eta2 = 2.*ka;
H1_eta = 2/pi-besselj(0,eta2) + (16/pi-5).*sin(eta2)./eta2 + (12-
36/pi).*(1-cos(eta2))./eta2.^2;
R1 = 1-2.*besselj(1,eta2)./eta2;
X1 = 2.*H1_eta./eta2;
Zap = rho.*c./Sd.*(R1 + j.*X1);


% Driver Tube or Primary Plane Wave Tube Impedance --------
B1 = j.*rho.*w./(kb*Sb).*tan(kb.*Lb/2);
B2 = -j.*rho.*w./(kb*Sb).*csc(kb.*Lb);

% Splitter Impedance----------------------
% Hole 1
P11 = j.*rho.*w./(kp*Sp).*tan(kp.*Lp/2);
P12 = -j.*rho.*w./(kp*Sp).*csc(kp.*Lp);

% Hole 2
P21 = j.*rho.*w./(kp*Sp).*tan(kp.*Lp/2);
P22 = -j.*rho.*w./(kp*Sp).*csc(kp.*Lp);

% Hole 3
P31 = j.*rho.*w./(kp*Sp).*tan(kp.*Lp/2);
P32 = -j.*rho.*w./(kp*Sp).*csc(kp.*Lp);

% Hole 4
P41 = j.*rho.*w./(kp*Sp).*tan(kp.*Lp/2);
P42 = -j.*rho.*w./(kp*Sp).*csc(kp.*Lp);

% Hole 5
P51 = j.*rho.*w./(kp*Sp).*tan(kp.*Lp/2);
P52 = -j.*rho.*w./(kp*Sp).*csc(kp.*Lp);

% Receiver Tube Impedance----------------------
% Tube 1
C11 = j.*rho.*w./(kc*Sc).*tan(kc.*Lc/2);
C12 = -j.*rho.*w./(kc*Sc).*csc(kc.*Lc);

% Tube 2
C21 = j.*rho.*w./(kc*Sc).*tan(kc.*Lc/2);
```

```
C22 = -j.*rho.*w./(kc*Sc).*csc(kc.*Lc);

% Tube 3
C31 = j.*rho.*w./(kc*Sc).*tan(kc.*Lc/2);
C32 = -j.*rho.*w./(kc*Sc).*csc(kc.*Lc);

% Tube 4
C41 = j.*rho.*w./(kc*Sc).*tan(kc.*Lc/2);
C42 = -j.*rho.*w./(kc*Sc).*csc(kc.*Lc);

% Tube 5
C51 = j.*rho.*w./(kc*Sc).*tan(kc.*Lc/2);
C52 = -j.*rho.*w./(kc*Sc).*csc(kc.*Lc);

% Inserts Impedance-------------------------
% Insert 1
I11 = j.*rho.*w./(ki*Si).*tan(ki.*Li/2);
I12 = -j.*rho.*w./(ki*Si).*csc(ki.*Li);

% Insert 2
I21 = j.*rho.*w./(ki*Si).*tan(ki.*Li/2);
I22 = -j.*rho.*w./(ki*Si).*csc(ki.*Li);

% Insert 3
I31 = j.*rho.*w./(ki*Si).*tan(ki.*Li/2);
I32 = -j.*rho.*w./(ki*Si).*csc(ki.*Li);

% Insert 4
I41 = j.*rho.*w./(ki*Si).*tan(ki.*Li/2);
I42 = -j.*rho.*w./(ki*Si).*csc(ki.*Li);

% Insert 5
I51 = j.*rho.*w./(ki*Si).*tan(ki.*Li/2);
I52 = -j.*rho.*w./(ki*Si).*csc(ki.*Li);

% Path Impedance-------------------------
%Path 1
Z11 = C11+I11+I12;
Z12 = P11+C11;
Z13 = Z11.*C12./(Z11+C12);
Z14 = Z12+Z13;
Z15 = Z14.*P12./(Z14+P12);
Z1  = Z15+P11;

%Path 2
Z21 = C21+I21+I22;
Z22 = P21+C21;
Z23 = Z21.*C22./(Z21+C22);
Z24 = Z22+Z23;
Z25 = Z24.*P22./(Z24+P22);
Z2  = Z25+P21;

%Path 3
Z31 = C31+I31+I32;
Z32 = P31+C31;
Z33 = Z31.*C32./(Z31+C32);
Z34 = Z32+Z33;
```

```
Z35 = Z34.*P32./(Z34+P32);
Z3  = Z35+P31;

%Path 4
Z41 = C41+I41+I42;
Z42 = P41+C41;
Z43 = Z41.*C42./(Z41+C42);
Z44 = Z42+Z43;
Z45 = Z44.*P42./(Z44+P42);
Z4  = Z45+P41;

%Path 5
Z51 = C51+I51+I52;
Z52 = P51+C51;
Z53 = Z51.*C52./(Z51+C52);
Z54 = Z52+Z53;
Z55 = Z54.*P52./(Z54+P52);
Z5  = Z55+P51;

% Impedance of all Five Paths
Zt =
Z1.*Z2.*Z3.*Z4.*Z5./(Z2.*Z3.*Z4.*Z5+Z1.*Z3.*Z4.*Z5+Z1.*Z2.*Z4.*Z5+Z1.*Z
2.*Z3.*Z5+Z1.*Z2.*Z3.*Z4);

% Total impedance from all tubes-----
Ztubes = (B1+B2).*(B1+Zt)./(B1+B2+B1+Zt);

% U1 = -Bl./(Ze.*Sd.*(Zap-Ztubes-Zad));
U1 = -eg.*Bl./(Ze.*Sd.*(Zap-Ztubes-Zad));

% Pressure at the Source-------------
ps = (U1.*Ztubes);

U2 = B2.*U1./(B1+Zt+B2);

U41 =
1/5.*C12.*P12.*U2./(C11.^2+2.*C11.*C12+C11.*P11+C11.*P12+I11.*C11+I11.*
C12+I11.*P11+I11.*P12+I12.*C11+I12.*C12+I12.*P11+I12.*P12+C12.*P11+C12.
*P12);

% Pressure at the termination of Tube 1------
pt1 = U41.*I12;
pt1 = pt1./eg;
pt1 = 20*log10(pt1);

% Measured FRF DATA
[F,A] = textread('..\FRF\frf\frf.txt','%f %f','headerlines',5);
load('pt')
% pt1(1000:1250)=pt1100-23.9052;
pt1 = pt1+25; %gain

%Plotting Routine
figure(1)
clf;
set(gcf,'DefaultAxesFontName','arial');
set(gcf,'DefaultAxesFontSize',12);
set(gcf,'DefaultAxesFontWeight','bold')
```

```
set(gcf,'DefaultAxesLineWidth',1.5);
set(gcf,'DefaultAxesGridLineStyle','--');
set(gcf,'DefaultLineLineWidth',2.125);
set(gcf,'DefaultLineMarkerSize',8);

plot(f,pt1,':',F,A)
% title('Measured Driver Parameters included in Model','Fontsize',18)
xlabel('Frequency (Hz)','Fontsize',16)
ylabel('Pressure (dB)','Fontsize',16)
legend('Modeled','Measured')
axis([0 5000 28 90])
```

C.2 VERIFICATION CODE

C.2.1 broadband_verification.m

```
%%%%%%%%%%%%%%%%%%%%%%%%%%%%%%%%%%%%%%%%%%%%%%%%%%%%%%%%%%%%%%%%%%
% This file was used to produce the broadband verification       %
% results in Chapter 6                                           %
%                                                                %
%                                                                %
%%%%%%%%%%%%%%%%%%%%%%%%%%%%%%%%%%%%%%%%%%%%%%%%%%%%%%%%%%%%%%%%%%


clc
clear all

% Import DATA
% Tube 1
[F,tu11] = textread('t11.txt','%f %f','headerlines',5);
[F,tu12] = textread('t12.txt','%f %f','headerlines',5);
[F,tu13] = textread('t13.txt','%f %f','headerlines',5);
[F,tu14] = textread('t14.txt','%f %f','headerlines',5);
[F,tu15] = textread('t15.txt','%f %f','headerlines',5);

% Tube 2
[F,tu21] = textread('tu21.txt','%f %f','headerlines',5);
[F,tu22] = textread('tu22.txt','%f %f','headerlines',5);
[F,tu23] = textread('tu23.txt','%f %f','headerlines',5);
[F,tu24] = textread('tu24.txt','%f %f','headerlines',5);
[F,tu25] = textread('tu25.txt','%f %f','headerlines',5);

% Tube 3
[F,tu31] = textread('t31.txt','%f %f','headerlines',5);
[F,tu32] = textread('t32.txt','%f %f','headerlines',5);
[F,tu33] = textread('t33.txt','%f %f','headerlines',5);
[F,tu34] = textread('t34.txt','%f %f','headerlines',5);
[F,tu35] = textread('t35.txt','%f %f','headerlines',5);
```

```
% Tube 4
[F,tu41] = textread('t41.txt','%f %f','headerlines',5);
[F,tu42] = textread('t42.txt','%f %f','headerlines',5);
[F,tu43] = textread('t43.txt','%f %f','headerlines',5);
[F,tu44] = textread('t44.txt','%f %f','headerlines',5);
[F,tu45] = textread('t45.txt','%f %f','headerlines',5);

% Tube 5
[F,tu51] = textread('t51.txt','%f %f','headerlines',5);
[F,tu52] = textread('t52.txt','%f %f','headerlines',5);
[F,tu53] = textread('t53.txt','%f %f','headerlines',5);
[F,tu54] = textread('t54.txt','%f %f','headerlines',5);
[F,tu55] = textread('t55.txt','%f %f','headerlines',5);


tu1 = [tu11 tu12 tu13 tu14 tu15];
tu2 = [tu21 tu22 tu23 tu24 tu25];
tu3 = [tu31 tu32 tu33 tu34 tu35];
tu4 = [tu41 tu42 tu43 tu44 tu45];
tu5 = [tu51 tu52 tu53 tu54 tu55];

tubes = [tu1 tu2 tu3 tu4 tu5];

tube1 = tu1;
tube2 = tu2;
tube3 = tu3;
tube4 = tu4;
tube5 = tu5;

% Overall mean
gm = mean(tubes')';

% Error
% Tube 1
d11 = (tube1(:,1)-gm);
d12 = (tube1(:,2)-gm);
d13 = (tube1(:,3)-gm);
d14 = (tube1(:,4)-gm);
d15 = (tube1(:,5)-gm);

% Tube 2
d21 = tube2(:,1)-gm;
d22 = tube2(:,2)-gm;
d23 = tube2(:,3)-gm;
d24 = tube2(:,4)-gm;
d25 = tube2(:,5)-gm;

% Tube 3
d31 = tube3(:,1)-gm;
d32 = tube3(:,2)-gm;
d33 = tube3(:,3)-gm;
d34 = tube3(:,4)-gm;
d35 = tube3(:,5)-gm;

% Tube 4
d41 = tube4(:,1)-gm;
d42 = tube4(:,2)-gm;
```

```
d43 = tube4(:,3)-gm;
d44 = tube4(:,4)-gm;
d45 = tube4(:,5)-gm;

% Tube 5
d51 = tube5(:,1)-gm;
d52 = tube5(:,2)-gm;
d53 = tube5(:,3)-gm;
d54 = tube5(:,4)-gm;
d55 = tube5(:,5)-gm;

e1 = [d11 d12 d13 d14 d15];
e2 = [d21 d22 d23 d24 d25];
e3 = [d31 d32 d33 d34 d35];
e4 = [d41 d42 d43 d44 d45];
e5 = [d51 d52 d53 d54 d55];

% Mean of the Errors
mu1 = mean(e1')';
mu2 = mean(e2')';
mu3 = mean(e3')';
mu4 = mean(e4')';
mu5 = mean(e5')';

% Standard Deviation of the Errors
sigma1 = std(e1')';
sigma2 = std(e2')';
sigma3 = std(e3')';
sigma4 = std(e4')';
sigma5 = std(e5')';

conf = 2;

% Upper Confidence Limit
Ui1 = (mu1+conf*sigma1);
Ui2 = (mu2+conf*sigma2);
Ui3 = (mu3+conf*sigma3);
Ui4 = (mu4+conf*sigma4);
Ui5 = (mu5+conf*sigma5);

% Lower Confidence Limit
Li1 = (mu1-conf*sigma1);
Li2 = (mu2-conf*sigma2);
Li3 = (mu3-conf*sigma3);
Li4 = (mu4-conf*sigma4);
Li5 = (mu5-conf*sigma5);

lf = 2201;
uf = 4900;
res = 200;

x = 1:res:uf;
bw = 1:res:lf;

Uin1(1:length(bw)+1) = max(Ui1(20:lf));
Uin1(length(bw)+1:length(x)) = max(Ui1(lf:uf));
```

```
Uin2(1:length(bw)+1) = max(Ui2(20:lf));
Uin2(length(bw)+1:length(x)) = max(Ui2(lf:uf));

Uin3(1:length(bw)+1) = max(Ui3(20:lf));
Uin3(length(bw)+1:length(x)) = max(Ui3(lf:uf));

Uin4(1:length(bw)+1) = max(Ui4(20:lf));
Uin4(length(bw)+1:length(x)) = max(Ui4(lf:uf));

Uin5(1:length(bw)+1) = max(Ui5(20:lf));
Uin5(length(bw)+1:length(x)) = max(Ui5(lf:uf));


Lin1(1:length(bw)+1) = min(Li1(20:lf));
Lin1(length(bw)+1:length(x)) = min(Li1(lf:uf));

Lin2(1:length(bw)+1) = min(Li2(20:lf));
Lin2(length(bw)+1:length(x)) = min(Li2(lf:uf));

Lin3(1:length(bw)+1) = min(Li3(20:lf));
Lin3(length(bw)+1:length(x)) = min(Li3(lf:uf));

Lin4(1:length(bw)+1) = min(Li4(20:lf));
Lin4(length(bw)+1:length(x)) = min(Li4(lf:uf));

Lin5(1:length(bw)+1) = min(Li5(20:lf));
Lin5(length(bw)+1:length(x)) = min(Li5(lf:uf));


% Class 1 probe limits
class1up(1:length(F)) = 0.5;
class1d(1:length(F)) = -0.5;

% Class 2 probe limits
class2up(1:length(F)) = 1;
class2d(1:length(F)) = -1;

% Plotting Routine
% Includes:
% All Five Tubes

figure(1)
clf;
set(gcf,'DefaultAxesFontName','arial');
set(gcf,'DefaultAxesFontSize',12);
set(gcf,'DefaultAxesFontWeight','bold')
set(gcf,'DefaultAxesLineWidth',2);
set(gcf,'DefaultLineLineWidth',1.5);
set(gcf,'DefaultLineMarkerSize',8);

plot(F,mu1,x,Uin1,'v',x,Lin1,'^',F,class1up,'--k',F,class1d,'--
k',F,class2up,':k',F,class2d,':k')
% title('Tube 1 Error')
xlabel('Frequency (Hz)','Fontsize',16)
ylabel('Error (dB)','Fontsize',16)
axis([0 6400 -1.5 1.5])
```

```
figure(2)
clf;
set(gcf,'DefaultAxesFontName','arial');
set(gcf,'DefaultAxesFontSize',12);
set(gcf,'DefaultAxesFontWeight','bold')
set(gcf,'DefaultAxesLineWidth',2);
set(gcf,'DefaultLineLineWidth',1.5);
set(gcf,'DefaultLineMarkerSize',8);

plot(F,mu2,x,Uin2,'v',x,Lin2,'^',F,class1up,'--k',F,class1d,'--
k',F,class2up,':k',F,class2d,':k')
% title('Tube 2 Error')
xlabel('Frequency (Hz)','Fontsize',16)
ylabel('Error (dB)','Fontsize',16)
axis([0 6400 -1.5 1.5])


figure(3)
clf;
set(gcf,'DefaultAxesFontName','arial');
set(gcf,'DefaultAxesFontSize',12);
set(gcf,'DefaultAxesFontWeight','bold')
set(gcf,'DefaultAxesLineWidth',2);
set(gcf,'DefaultLineLineWidth',1.5);
set(gcf,'DefaultLineMarkerSize',8);

plot(F,mu3,x,Uin3,'v',x,Lin3,'^',F,class1up,'--k',F,class1d,'--
k',F,class2up,':k',F,class2d,':k')
% title('Tube 3 Error')
xlabel('Frequency (Hz)','Fontsize',16)
ylabel('Error (dB)','Fontsize',16)
axis([0 6400 -1.5 1.5])


figure(4)
clf;
set(gcf,'DefaultAxesFontName','arial');
set(gcf,'DefaultAxesFontSize',12);
set(gcf,'DefaultAxesFontWeight','bold')
set(gcf,'DefaultAxesLineWidth',2);
set(gcf,'DefaultLineLineWidth',1.5);
set(gcf,'DefaultLineMarkerSize',8);

plot(F,mu4,x,Uin4,'v',x,Lin4,'^',F,class1up,'--k',F,class1d,'--
k',F,class2up,':k',F,class2d,':k')
% title('Tube 4 Error')
xlabel('Frequency (Hz)','Fontsize',16)
ylabel('Error (dB)','Fontsize',16)
axis([0 6400 -1.5 1.5])


figure(5)
clf;
set(gcf,'DefaultAxesFontName','arial');
set(gcf,'DefaultAxesFontSize',12);
set(gcf,'DefaultAxesFontWeight','bold')
set(gcf,'DefaultAxesLineWidth',2);
```

```
set(gcf,'DefaultLineLineWidth',1.5);
set(gcf,'DefaultLineMarkerSize',8);

plot(F,mu5,x,Uin5,'v',x,Lin5,'^',F,class1up,'--k',F,class1d,'--
k',F,class2up,':k',F,class2d,':k')
% title('Tube 5 Error')
xlabel('Frequency (Hz)','Fontsize',16)
ylabel('Error (dB)','Fontsize',16)
axis([0 6400 -1.5 1.5])

figure(6)
clf;
set(gcf,'DefaultAxesFontName','arial');
set(gcf,'DefaultAxesFontSize',12);
set(gcf,'DefaultAxesFontWeight','bold')
set(gcf,'DefaultAxesLineWidth',2);
set(gcf,'DefaultLineLineWidth',1.5);
set(gcf,'DefaultLineMarkerSize',8);

plot(F,tubes)
xlabel('Frequency (Hz)','Fontsize',16)
ylabel('Mag. (dB) [0dB = 1V/V]','Fontsize',16)
axis([0 4500 -62 -8])
grid
```

C.2.2 discrete_verification.m

```
%%%%%%%%%%%%%%%%%%%%%%%%%%%%%%%%%%%%%%%%%%%%%%%%%%%%%%%%%%%%%%%%%%%
% This file Calculates the discrete frequency verification        %
% results % presented in Chapter 6.                               %
%                                                                 %
%                                                                 %
%%%%%%%%%%%%%%%%%%%%%%%%%%%%%%%%%%%%%%%%%%%%%%%%%%%%%%%%%%%%%%%%%%%


clc; clear all;clf

%load data
%mic 1
%20-1
    ch20_1 = textread('20-1.txt','%f','headerlines',27);
%20-2
    ch20_2 = textread('20-2.txt','%f','headerlines',27);
%20-3
    ch20_3 = textread('20-3.txt','%f','headerlines',27);

%mic 2
%21-1
    ch21_1 = textread('21-1.txt','%f','headerlines',27);
%21-2
    ch21_2 = textread('21-2.txt','%f','headerlines',27);
%21-3
    ch21_3 = textread('21-3.txt','%f','headerlines',27);
```

```
%mic 3
%22-1
    ch22_1 = textread('22-1.txt','%f','headerlines',27);
%22-2
    ch22_2 = textread('22-2.txt','%f','headerlines',27);
%22-3
    ch22_3 = textread('22-3.txt','%f','headerlines',27);

%mic 4
%23-1
    ch23_1 = textread('23-1.txt','%f','headerlines',27);
%23-2
    ch23_2 = textread('23-2.txt','%f','headerlines',27);
%23-3
    ch23_3 = textread('23-3.txt','%f','headerlines',27);

% Reference Mic
%25-1
    ch25_1 = textread('25-1.txt','%f','headerlines',31);
%25-2
    ch25_2 = textread('25-2.txt','%f','headerlines',31);
%25-3
    ch25_3 = textread('25-3.txt','%f','headerlines',31);

%%%%%%%% Reference  %%%%%%%%%%%%%
%%%%%%%%  1  %%%%%%%%%%%%%

p1 = fft(ch25_1)/length(ch25_1);
p1 = p1(1:length(p1)/2);
p1(2:length(p1)) = 2*p1(2:length(p1));
p1 = abs(p1);

%Peak find
[a,b] = max(p1);
dBr1 = 20*log10(abs((a-a)/a)+1);

%%%%%%%%  2  %%%%%%%%%%%%%

p2 = fft(ch25_2)/length(ch25_2);
p2 = p2(1:length(p2)/2);
p2(2:length(p2)) = 2*p2(2:length(p2));
p2 = abs(p2);

%Peak find
[c,d] = max(p2);

%Calculate % difference
dBr2 = 20*log10(abs((a-c)/a)+1);

%%%%%%%%  3 %%%%%%%%%%%%%

p3 = fft(ch25_3)/length(ch25_3);
p3 = p3(1:length(p3)/2);
p3(2:length(p3)) = 2*p3(2:length(p3));
p3 = abs(p3);

%Peak find
```

```
[e,f] = max(p3);

%Calculate % error & dB error
dBr3 = 20*log10(abs((a-e)/a)+1);



%%%%%%%% 20-1  %%%%%%%%%%%%%

p1 = fft(ch20_1)/length(ch20_1);
p1 = p1(1:length(p1)/2);
p1(2:length(p1)) = 2*p1(2:length(p1));
p1 = abs(p1);

%Peak find
[a,b] = max(p1);
dBa = 20*log10(abs((a-a)/a)+1);

%%%%%%%% 20-2  %%%%%%%%%%%%%

p2 = fft(ch20_2)/length(ch20_2);
p2 = p2(1:length(p2)/2);
p2(2:length(p2)) = 2*p2(2:length(p2));
p2 = abs(p2);

%Peak find
[c,d] = max(p2);

%Calculate % difference
dBc = 20*log10(abs((a-c)/a)+1);

%%%%%%%% 20-3 %%%%%%%%%%%%%

p3 = fft(ch20_3)/length(ch20_3);
p3 = p3(1:length(p3)/2);
p3(2:length(p3)) = 2*p3(2:length(p3));
p3 = abs(p3);

%Peak find
[e,f] = max(p3);

%Calculate % error & dB error
dBe = 20*log10(abs((a-e)/a)+1);

%%%%%%%% 21-1 %%%%%%%%%%%%%

p4 = fft(ch21_1)/length(ch21_1);
p4 = p4(1:length(p4)/2);
p4(2:length(p4)) = 2*p4(2:length(p4));
p4 = abs(p4);

%Peak find
[g,h] = max(p4);

%Calculate % error & dB error
dBg = 20*log10(abs((g-g)/g)+1);
```

```
%%%%%%%% 21-2 %%%%%%%%%%%%%

p5 = fft(ch21_2)/length(ch21_2);
p5 = p5(1:length(p5)/2);
p5(2:length(p5)) = 2*p5(2:length(p5));
p5 = abs(p5);

%Peak find
[j,k] = max(p5);

%Calculate % error & dB error
dBj = 20*log10(abs((g-j)/g)+1);

%%%%%%%% 21-3 %%%%%%%%%%%%%

p6 = fft(ch21_3)/length(ch21_3);
p6 = p6(1:length(p6)/2);
p6(2:length(p6)) = 2*p6(2:length(p6));
p6 = abs(p6);

%Peak find
[l,m] = max(p6);

%Calculate % difference
dBl = 20*log10(abs((g-l)/g)+1);


%%%%%%%% 22-1 %%%%%%%%%%%%%

p7 = fft(ch22_1)/length(ch22_1);
p7 = p7(1:length(p7)/2);
p7(2:length(p7)) = 2*p7(2:length(p7));
p7 = abs(p7);

%Peak find
[n,o] = max(p7);

%Calculate % difference
dBn = 20*log10(abs((n-n)/n)+1);

%%%%%%%% 22-2 %%%%%%%%%%%%%

p8 = fft(ch22_2)/length(ch22_2);
p8 = p8(1:length(p8)/2);
p8(2:length(p8)) = 2*p8(2:length(p8));
p8 = abs(p8);

%Peak find
[c1,d1] = max(p8);

%Calculate % difference
dBc1 = 20*log10(abs((n-c1)/n)+1);

%%%%%%%% 22-3 %%%%%%%%%%%%%

p9 = fft(ch22_3)/length(ch22_3);
p9 = p9(1:length(p9)/2);
```

```
p9(2:length(p9)) = 2*p9(2:length(p9));
p9 = abs(p9);

%Peak find
[e1,f1] = max(p9);

%Calculate % error & dB error
dBe1 = 20*log10(abs((n-e1)/n)+1);

%%%%%%%% 23-1 %%%%%%%%%%%%%

p10 = fft(ch23_1)/length(ch23_1);
p10 = p10(1:length(p10)/2);
p10(2:length(p10)) = 2*p10(2:length(p10));
p10 = abs(p10);

%Peak find
[p,q] = max(p10);

%Calculate % difference
dBp = 20*log10(abs((p-p)/p)+1);

%%%%%%%% 23-2 %%%%%%%%%%%%%

p11 = fft(ch23_2)/length(ch23_2);
p11 = p11(1:length(p11)/2);
p11(2:length(p11)) = 2*p11(2:length(p11));
p11 = abs(p11);

%Peak find
[r,s] = max(p11);

%Calculate % difference
dBr = 20*log10(abs((p-r)/p)+1);

%%%%%%%% 23-3 %%%%%%%%%%%%%

p12 = fft(ch23_3)/length(ch23_3);
p12 = p12(1:length(p12)/2);
p12(2:length(p12)) = 2*p12(2:length(p12));
p12 = abs(p12);

%Peak find
[t,u] = max(p12);

%Calculate % error & dB error
dBt = 20*log10(abs((p-t)/p)+1);


%%%%%%%%%%%%%% Plotting Routine %%%%%%%%%%%%
pos= [1:1:3];
disp('dB')
er20 = [dBa dBc dBe]
er21 = [dBg dBj dBl]
er22 = [dBn dBc1 dBe1]
er23 = [dBp dBr dBt]
erRef = [dBr1 dBr2 dBr3]
```

```
figure(1)
set(gcf,'DefaultAxesFontName','arial');
set(gcf,'DefaultAxesFontSize',13);
set(gcf,'DefaultAxesFontWeight','bold')
set(gcf,'DefaultAxesLineWidth',2);
set(gcf,'DefaultLineLineWidth',2);
set(gcf,'DefaultLineMarkersize',11);
plot(pos,er20,'d',pos,er21,'s',pos,er22,'x',pos,er23,'o',pos,erRef,'p')
grid;
title(['Calibration Error at ',num2str(f-1),' Hz and 114
dB'],'Fontsize',16);
xlabel('Probe Position');
ylabel('Pressure Variation (dB)');
axis([1 3 -.5 .5]);
legend('Mic 1','Mic 2','Mic 3','Mic 4 (Pole Mic)','Reference Mic',0)
set(gca,'XTick',[1 2 3])
set(gca,'XTickLabel','1st|2nd|3rd|')
```

C.3 DIRECTIVITY CODE

C.3.1 ed_orthogonal.m

```
%%%%%%%%%%%%%%%%%%%%%%%%%%%%%%%%%%%%%%%%%%%%%%%%%%%%%%%%%%%%%%%%%%%
%                                                                 %
% This file reads in the pressure from the orthogonal probe and   %
% outputs the total energy density as a function of frequency.    %
% This file includes the correction function described in         %
% Chapter 7                                                       %
%                                                                 %
%%%%%%%%%%%%%%%%%%%%%%%%%%%%%%%%%%%%%%%%%%%%%%%%%%%%%%%%%%%%%%%%%%%


function [ED,T,U] = ED(p1,p2,p4,p3,N)
warning off MATLAB:divideByZero

%Length of Sample
t = 20;

f = (1:2000/N)*N;

rho = 1.21; % Density of air
c = 343; % Speed of sound
radius = .0254;%m
k = 2*pi*f/c;
k = k';
omega = k*c;

fc=70;
```

```
p1(1:fix(fc/N)) = zeros;
p2(1:fix(fc/N)) = zeros;
p3(1:fix(fc/N)) = zeros;
p4(1:fix(fc/N)) = zeros;

p1 = p1(1:length(f));
p2 = p2(1:length(f));
p3 = p3(1:length(f));
p4 = p4(1:length(f));

% Mic Position Vectors
r1=[+radius/sqrt(3);-radius/sqrt(3);-radius/sqrt(3)];
r2=[-radius/sqrt(3);+radius/sqrt(3);-radius/sqrt(3)];
r3=[-radius/sqrt(3);-radius/sqrt(3);-radius/sqrt(3)];
r4=[-radius/sqrt(3);-radius/sqrt(3);+radius/sqrt(3)];

% On Axis Velocity Values
Ux13=(p1-p3)./(j*rho.*omega*(r1(1)-r3(1)));     % This vector points in
the - x direction
Uy23=(p2-p3)./(j*rho.*omega*(r2(2)-r3(2)));     % This vector points in
the - y direction
Uz43=(p4-p3)./(j*rho.*omega*(r4(3)-r3(3)));     % This vector points in
the - z direction
Ux31=-Ux13;                                     % This vector points in
the + x direction
Uy32=-Uy23;                                     % This vector points in
the + y direction
Uz34=-Uz43;                                     % This vector points in
the + z direction

% Determine the phase angle of the on axis velocities
Ux31pha=angle(Ux31);
Uy32pha=angle(Uy32);
Uz34pha=angle(Uz34);

% In the XY plane
phadiffxy=180/pi*(Ux31pha-Uy32pha);             % Difference in phase
of Ux and Uy
theta=atan2(abs(Uy32),abs(Ux31));

for index=1:length(phadiffxy)
    if (abs(phadiffxy(index)) > 85 & abs(phadiffxy(index)) < 275)
        theta(index)=-theta(index);
    end
end

% This vector points in the + y - x direction
U12=(p1-p2)./(j*rho.*omega*sqrt((r2(1)-r1(1) )^2 + (r2(2)-r1(2))^2));

%------------------------------------------------------
thetaa=(3*pi/4-theta);
for k = 1:length(f)
    if thetaa(k) > (87*pi/180) & thetaa(k) < (93*pi/180)
        U12p(k) = 0;
    else
        U12p(k)=U12(k)/cos(thetaa(k));
    end
```

```
end
U12p = U12p';
% U12p=U12./cos(thetaa);

Uy12=U12p.*sin(theta);
Ux12=U12p.*cos(theta);

% In the XZ Plane
% This vector points in the - z + x direction
U41=(p4-p1)./(j*rho.*omega*sqrt((r4(1)-r1(1) )^2 + (r4(3)-r1(3))^2));
U14=-U41;

% Difference in phase of Ux and Uz
phadiffxz=180/pi*(Ux31pha-Uz34pha);
betaxz=atan2(abs(Uz34),abs(Ux31));

if (abs(phadiffxz) > 85 & abs(phadiffxz) < 275)
    betaxz=-betaxz;
end

% ================================================================
betaa=(3*pi/4-betaxz);
for h = 1:length(f)
    if betaa(h) > (87*pi/180) & betaa(h) < (93*pi/180)
        U14p(h) = 0;
    else
        U14p(h)=U14(h)/cos(betaa(h));
    end
end

U14p = U14p';
% U14p=U14./cos(betaa);
Ux14=U14p.*cos(betaxz);
Uz14=U14p.*sin(betaxz);

% In the YZ Plane
% This vector points in the - y + z direction
U24=(p2-p4)./(j*rho.*omega*sqrt((r2(2)-r4(2) )^2 + (r2(3)-r4(3))^2));

% Difference in phase of Uy and Uz
phadiffyz=180/pi*(Uy32pha-Uz34pha);
alphayz=atan2(abs(Uz34),abs(Uy32));

if (abs(phadiffyz) > 85 & abs(phadiffyz) < 275)
    alphayz=-alphayz%;
end


%++++++++++++++++++++++++++++++++++++++++++++++++
alphaa=(3*pi/4+alphayz);
for s = 1:length(f)
    if alphaa(s) > (87*pi/180) & alphaa(s) < (93*pi/180)
        U24p(s) = 0;
    else
        U24p(s)=U24(s)/cos(alphaa(s));
    end
end
```

```
U24p = U24p';
% U24p=U24./cos(alphaa);
Uz24=U24p.*sin(alphayz);
Uy24=U24p.*cos(alphayz);

% % Taylor Series expansion
Ux = (Ux12-Ux31+Ux14)/1.5;
Uy = (Uy12-Uy32+Uy24)/1.5;
Uz = (Uz14-Uz34+Uz24)/1.5;

p=mean(p1+p2+p3+p4,2);                               % Mean pressure
U=p.*conj(p)/(2*rho*c^2);                           % Potential energy

Tx=rho*(Ux.*conj(Ux))/2;
Ty=rho*(Uy.*conj(Uy))/2;
Tz=rho*(Uz.*conj(Uz))/2;
T=Tx+Ty+Tz;                                         % Kinetic energy

ED = T+U;                                         % Total energy
density
```

C.3.2 directivity_l_axis.m

```
%%%%%%%%%%%%%%%%%%%%%%%%%%%%%%%%%%%%%%%%%%%%%%%%%%%%%%%%%%%%%
%                                                           %
% This file imports the pressure data used to calculate the %
% energy density for the rotation test described in         %
% Chapter 7. This file is for the l-axis rotation test      %
%                                                           %
%%%%%%%%%%%%%%%%%%%%%%%%%%%%%%%%%%%%%%%%%%%%%%%%%%%%%%%%%%%%%


warning off MATLAB:divideByZero
clc; clear all;

%Length of Sample
t = 20;
N = 1;

rho = 1.21; % Density of air
c = 343; % Speed of sound
radius = .0254;%m

f = (1:6000/N)*N;
k = 2*pi*f/c;
k = k';
omega = k*c;

%Load Calibration Constants
% load('..\CC')

%Load Pressure Data
load('data_x');
```

```
% For Loop to Average the 20 sec of Data ===================
for m = 1:t*N
    if m == 1
        ch20_0(:,m) = x0c20(m:m*12800/N);
        ch20_15(:,m) = x15c20(m:m*12800/N);
        ch20_30(:,m) = x30c20(m:m*12800/N);
        ch20_45(:,m) = x45c20(m:m*12800/N);
        ch20_60(:,m) = x60c20(m:m*12800/N);
        ch20_75(:,m) = x75c20(m:m*12800/N);
        ch20_90(:,m) = x90c20(m:m*12800/N);
        ch20_105(:,m) = x105c20(m:m*12800/N);
        ch20_120(:,m) = x120c20(m:m*12800/N);
        ch20_135(:,m) = x135c20(m:m*12800/N);
        ch20_150(:,m) = x150c20(m:m*12800/N);
        ch20_165(:,m) = x165c20(m:m*12800/N);
        ch20_180(:,m) = x180c20(m:m*12800/N);

        ch21_0(:,m) = x0c21(m:m*12800/N);
        ch21_15(:,m) = x15c21(m:m*12800/N);
        ch21_30(:,m) = x30c21(m:m*12800/N);
        ch21_45(:,m) = x45c21(m:m*12800/N);
        ch21_60(:,m) = x60c21(m:m*12800/N);
        ch21_75(:,m) = x75c21(m:m*12800/N);
        ch21_90(:,m) = x90c21(m:m*12800/N);
        ch21_105(:,m) = x105c21(m:m*12800/N);
        ch21_120(:,m) = x120c21(m:m*12800/N);
        ch21_135(:,m) = x135c21(m:m*12800/N);
        ch21_150(:,m) = x150c21(m:m*12800/N);
        ch21_165(:,m) = x165c21(m:m*12800/N);
        ch21_180(:,m) = x180c21(m:m*12800/N);

        ch22_0(:,m) = x0c22(m:m*12800/N);
        ch22_15(:,m) = x15c22(m:m*12800/N);
        ch22_30(:,m) = x30c22(m:m*12800/N);
        ch22_45(:,m) = x45c22(m:m*12800/N);
        ch22_60(:,m) = x60c22(m:m*12800/N);
        ch22_75(:,m) = x75c22(m:m*12800/N);
        ch22_90(:,m) = x90c22(m:m*12800/N);
        ch22_105(:,m) = x105c22(m:m*12800/N);
        ch22_120(:,m) = x120c22(m:m*12800/N);
        ch22_135(:,m) = x135c22(m:m*12800/N);
        ch22_150(:,m) = x150c22(m:m*12800/N);
        ch22_165(:,m) = x165c22(m:m*12800/N);
        ch22_180(:,m) = x180c22(m:m*12800/N);

        ch23_0(:,m) = x0c23(m:m*12800/N);
        ch23_15(:,m) = x15c23(m:m*12800/N);
        ch23_30(:,m) = x30c23(m:m*12800/N);
        ch23_45(:,m) = x45c23(m:m*12800/N);
        ch23_60(:,m) = x60c23(m:m*12800/N);
        ch23_75(:,m) = x75c23(m:m*12800/N);
        ch23_90(:,m) = x90c23(m:m*12800/N);
        ch23_105(:,m) = x105c23(m:m*12800/N);
        ch23_120(:,m) = x120c23(m:m*12800/N);
        ch23_135(:,m) = x135c23(m:m*12800/N);
        ch23_150(:,m) = x150c23(m:m*12800/N);
        ch23_165(:,m) = x165c23(m:m*12800/N);
```

```
    ch23_180(:,m) = x180c23(m:m*12800/N);

else
    ch20_0(:,m) = x0c20((m-1)*12800/N+1:m*12800/N);
    ch20_15(:,m) = x15c20((m-1)*12800/N+1:m*12800/N);
    ch20_30(:,m) = x30c20((m-1)*12800/N+1:m*12800/N);
    ch20_45(:,m) = x45c20((m-1)*12800/N+1:m*12800/N);
    ch20_60(:,m) = x60c20((m-1)*12800/N+1:m*12800/N);
    ch20_75(:,m) = x75c20((m-1)*12800/N+1:m*12800/N);
    ch20_90(:,m) = x90c20((m-1)*12800/N+1:m*12800/N);
    ch20_105(:,m) = x105c20((m-1)*12800/N+1:m*12800/N);
    ch20_120(:,m) = x120c20((m-1)*12800/N+1:m*12800/N);
    ch20_135(:,m) = x135c20((m-1)*12800/N+1:m*12800/N);
    ch20_150(:,m) = x150c20((m-1)*12800/N+1:m*12800/N);
    ch20_165(:,m) = x165c20((m-1)*12800/N+1:m*12800/N);
    ch20_180(:,m) = x180c20((m-1)*12800/N+1:m*12800/N);

    ch21_0(:,m) = x0c21((m-1)*12800/N+1:m*12800/N);
    ch21_15(:,m) = x15c21((m-1)*12800/N+1:m*12800/N);
    ch21_30(:,m) = x30c21((m-1)*12800/N+1:m*12800/N);
    ch21_45(:,m) = x45c21((m-1)*12800/N+1:m*12800/N);
    ch21_60(:,m) = x60c21((m-1)*12800/N+1:m*12800/N);
    ch21_75(:,m) = x75c21((m-1)*12800/N+1:m*12800/N);
    ch21_90(:,m) = x90c21((m-1)*12800/N+1:m*12800/N);
    ch21_105(:,m) = x105c21((m-1)*12800/N+1:m*12800/N);
    ch21_120(:,m) = x120c21((m-1)*12800/N+1:m*12800/N);
    ch21_135(:,m) = x135c21((m-1)*12800/N+1:m*12800/N);
    ch21_150(:,m) = x150c21((m-1)*12800/N+1:m*12800/N);
    ch21_165(:,m) = x165c21((m-1)*12800/N+1:m*12800/N);
    ch21_180(:,m) = x180c21((m-1)*12800/N+1:m*12800/N);

    ch22_0(:,m) = x0c22((m-1)*12800/N+1:m*12800/N);
    ch22_15(:,m) = x15c22((m-1)*12800/N+1:m*12800/N);
    ch22_30(:,m) = x30c22((m-1)*12800/N+1:m*12800/N);
    ch22_45(:,m) = x45c22((m-1)*12800/N+1:m*12800/N);
    ch22_60(:,m) = x60c22((m-1)*12800/N+1:m*12800/N);
    ch22_75(:,m) = x75c22((m-1)*12800/N+1:m*12800/N);
    ch22_90(:,m) = x90c22((m-1)*12800/N+1:m*12800/N);
    ch22_105(:,m) = x105c22((m-1)*12800/N+1:m*12800/N);
    ch22_120(:,m) = x120c22((m-1)*12800/N+1:m*12800/N);
    ch22_135(:,m) = x135c22((m-1)*12800/N+1:m*12800/N);
    ch22_150(:,m) = x150c22((m-1)*12800/N+1:m*12800/N);
    ch22_165(:,m) = x165c22((m-1)*12800/N+1:m*12800/N);
    ch22_180(:,m) = x180c22((m-1)*12800/N+1:m*12800/N);

    ch23_0(:,m) = x0c23((m-1)*12800/N+1:m*12800/N);
    ch23_15(:,m) = x15c23((m-1)*12800/N+1:m*12800/N);
    ch23_30(:,m) = x30c23((m-1)*12800/N+1:m*12800/N);
    ch23_45(:,m) = x45c23((m-1)*12800/N+1:m*12800/N);
    ch23_60(:,m) = x60c23((m-1)*12800/N+1:m*12800/N);
    ch23_75(:,m) = x75c23((m-1)*12800/N+1:m*12800/N);
    ch23_90(:,m) = x90c23((m-1)*12800/N+1:m*12800/N);
    ch23_105(:,m) = x105c23((m-1)*12800/N+1:m*12800/N);
    ch23_120(:,m) = x120c23((m-1)*12800/N+1:m*12800/N);
    ch23_135(:,m) = x135c23((m-1)*12800/N+1:m*12800/N);
    ch23_150(:,m) = x150c23((m-1)*12800/N+1:m*12800/N);
    ch23_165(:,m) = x165c23((m-1)*12800/N+1:m*12800/N);
```

```
        ch23_180(:,m) = x180c23((m-1)*12800/N+1:m*12800/N);
    end

% Windowing-----------------------
    H = hanning(12800);
ch20_0(:,m) = H.*ch20_0(:,m);
ch20_15(:,m) = H.*ch20_15(:,m);
ch20_30(:,m) = H.*ch20_30(:,m);
ch20_45(:,m) = H.*ch20_45(:,m);
ch20_60(:,m) = H.*ch20_60(:,m);
ch20_75(:,m) = H.*ch20_75(:,m);
ch20_90(:,m) = H.*ch20_90(:,m);
ch20_105(:,m) = H.*ch20_105(:,m);
ch20_120(:,m) = H.*ch20_120(:,m);
ch20_135(:,m) = H.*ch20_135(:,m);
ch20_150(:,m) = H.*ch20_150(:,m);
ch20_165(:,m) = H.*ch20_165(:,m);
ch20_180(:,m) = H.*ch20_180(:,m);

ch21_0(:,m) = H.*ch21_0(:,m);
ch21_15(:,m) = H.*ch21_15(:,m);
ch21_30(:,m) = H.*ch21_30(:,m);
ch21_45(:,m) = H.*ch21_45(:,m);
ch21_60(:,m) = H.*ch21_60(:,m);
ch21_75(:,m) = H.*ch21_75(:,m);
ch21_90(:,m) = H.*ch21_90(:,m);
ch21_105(:,m) = H.*ch21_105(:,m);
ch21_120(:,m) = H.*ch21_120(:,m);
ch21_135(:,m) = H.*ch21_135(:,m);
ch21_150(:,m) = H.*ch21_150(:,m);
ch21_165(:,m) = H.*ch21_165(:,m);
ch21_180(:,m) = H.*ch21_180(:,m);

ch22_0(:,m) = H.*ch22_0(:,m);
ch22_15(:,m) = H.*ch22_15(:,m);
ch22_30(:,m) = H.*ch22_30(:,m);
ch22_45(:,m) = H.*ch22_45(:,m);
ch22_60(:,m) = H.*ch22_60(:,m);
ch22_75(:,m) = H.*ch22_75(:,m);
ch22_90(:,m) = H.*ch22_90(:,m);
ch22_105(:,m) = H.*ch22_105(:,m);
ch22_120(:,m) = H.*ch22_120(:,m);
ch22_135(:,m) = H.*ch22_135(:,m);
ch22_150(:,m) = H.*ch22_150(:,m);
ch22_165(:,m) = H.*ch22_165(:,m);
ch22_180(:,m) = H.*ch22_180(:,m);

ch23_0(:,m) = H.*ch23_0(:,m);
ch23_15(:,m) = H.*ch23_15(:,m);
ch23_30(:,m) = H.*ch23_30(:,m);
ch23_45(:,m) = H.*ch23_45(:,m);
ch23_60(:,m) = H.*ch23_60(:,m);
ch23_75(:,m) = H.*ch23_75(:,m);
ch23_90(:,m) = H.*ch23_90(:,m);
ch23_105(:,m) = H.*ch23_105(:,m);
ch23_120(:,m) = H.*ch23_120(:,m);
ch23_135(:,m) = H.*ch23_135(:,m);
```

```
ch23_150(:,m) = H.*ch23_150(:,m);
ch23_165(:,m) = H.*ch23_165(:,m);
ch23_180(:,m) = H.*ch23_180(:,m);


% Channel 20 FFT (every 15 degrees) ===================
    p20aa_0(:,m) = fft(ch20_0(:,m))/length(ch20_0(:,m));
    p20_0(:,m) = p20aa_0(1:length(p20aa_0(:,m))/2,m);
    p20_0(2:length(p20_0(:,m)),m) = 2*p20_0(2:length(p20_0(:,m)),m);
    p20_0(:,m) = abs(p20_0(:,m));

    p20aa_15(:,m) = fft(ch20_15(:,m))/length(ch20_15(:,m));
    p20_15(:,m) = p20aa_15(1:length(p20aa_15(:,m))/2,m);
    p20_15(2:length(p20_15(:,m)),m) =
2*p20_15(2:length(p20_15(:,m)),m);
    p20_15(:,m) = abs(p20_15(:,m));

    p20aa_30(:,m) = fft(ch20_30(:,m))/length(ch20_30(:,m));
    p20_30(:,m) = p20aa_30(1:length(p20aa_30(:,m))/2,m);
    p20_30(2:length(p20_30(:,m)),m) =
2*p20_30(2:length(p20_30(:,m)),m);
    p20_30(:,m) = abs(p20_30(:,m));

    p20aa_45(:,m) = fft(ch20_45(:,m))/length(ch20_45(:,m));
    p20_45(:,m) = p20aa_45(1:length(p20aa_45(:,m))/2,m);
    p20_45(2:length(p20_45(:,m)),m) =
2*p20_45(2:length(p20_45(:,m)),m);
    p20_45(:,m) = abs(p20_45(:,m));

    p20aa_60(:,m) = fft(ch20_60(:,m))/length(ch20_60(:,m));
    p20_60(:,m) = p20aa_60(1:length(p20aa_60(:,m))/2,m);
    p20_60(2:length(p20_60(:,m)),m) =
2*p20_60(2:length(p20_60(:,m)),m);
    p20_60(:,m) = abs(p20_60(:,m));

    p20aa_75(:,m) = fft(ch20_75(:,m))/length(ch20_75(:,m));
    p20_75(:,m) = p20aa_75(1:length(p20aa_75(:,m))/2,m);
    p20_75(2:length(p20_75(:,m)),m) =
2*p20_75(2:length(p20_75(:,m)),m);
    p20_75(:,m) = abs(p20_75(:,m));

    p20aa_90(:,m) = fft(ch20_90(:,m))/length(ch20_90(:,m));
    p20_90(:,m) = p20aa_90(1:length(p20aa_90(:,m))/2,m);
    p20_90(2:length(p20_90(:,m)),m) =
2*p20_90(2:length(p20_90(:,m)),m);
    p20_90(:,m) = abs(p20_90(:,m));

    p20aa_105(:,m) = fft(ch20_105(:,m))/length(ch20_105(:,m));
    p20_105(:,m) = p20aa_105(1:length(p20aa_105(:,m))/2,m);
    p20_105(2:length(p20_105(:,m)),m) =
2*p20_105(2:length(p20_105(:,m)),m);
    p20_105(:,m) = abs(p20_105(:,m));

    p20aa_120(:,m) = fft(ch20_120(:,m))/length(ch20_120(:,m));
    p20_120(:,m) = p20aa_120(1:length(p20aa_120(:,m))/2,m);
    p20_120(2:length(p20_120(:,m)),m) =
2*p20_120(2:length(p20_120(:,m)),m);
```

```
    p20_120(:,m) = abs(p20_120(:,m));

    p20aa_135(:,m) = fft(ch20_135(:,m))/length(ch20_135(:,m));
    p20_135(:,m) = p20aa_135(1:length(p20aa_135(:,m))/2,m);
    p20_135(2:length(p20_135(:,m)),m) =
2*p20_135(2:length(p20_135(:,m)),m);
    p20_135(:,m) = abs(p20_135(:,m));

    p20aa_150(:,m) = fft(ch20_150(:,m))/length(ch20_150(:,m));
    p20_150(:,m) = p20aa_150(1:length(p20aa_150(:,m))/2,m);
    p20_150(2:length(p20_150(:,m)),m) =
2*p20_150(2:length(p20_150(:,m)),m);
    p20_150(:,m) = abs(p20_150(:,m));

    p20aa_165(:,m) = fft(ch20_165(:,m))/length(ch20_165(:,m));
    p20_165(:,m) = p20aa_165(1:length(p20aa_165(:,m))/2,m);
    p20_165(2:length(p20_165(:,m)),m) =
2*p20_165(2:length(p20_165(:,m)),m);
    p20_165(:,m) = abs(p20_165(:,m));

    p20aa_180(:,m) = fft(ch20_180(:,m))/length(ch20_180(:,m));
    p20_180(:,m) = p20aa_180(1:length(p20aa_180(:,m))/2,m);
    p20_180(2:length(p20_180(:,m)),m) =
2*p20_180(2:length(p20_180(:,m)),m);
    p20_180(:,m) = abs(p20_180(:,m));

% Channel 21 FFT (every 15 degrees) ===================
    p21aa_0(:,m) = fft(ch21_0(:,m))/length(ch21_0(:,m));
    p21_0(:,m) = p21aa_0(1:length(p21aa_0(:,m))/2,m);
    p21_0(2:length(p21_0(:,m)),m) = 2*p21_0(2:length(p21_0(:,m)),m);
    p21_0(:,m) = abs(p21_0(:,m));

    p21aa_15(:,m) = fft(ch21_15(:,m))/length(ch21_15(:,m));
    p21_15(:,m) = p21aa_15(1:length(p21aa_15(:,m))/2,m);
    p21_15(2:length(p21_15(:,m)),m) =
2*p21_15(2:length(p21_15(:,m)),m);
    p21_15(:,m) = abs(p21_15(:,m));

    p21aa_30(:,m) = fft(ch21_30(:,m))/length(ch21_30(:,m));
    p21_30(:,m) = p21aa_30(1:length(p21aa_30(:,m))/2,m);
    p21_30(2:length(p21_30(:,m)),m) =
2*p21_30(2:length(p21_30(:,m)),m);
    p21_30(:,m) = abs(p21_30(:,m));

    p21aa_45(:,m) = fft(ch21_45(:,m))/length(ch21_45(:,m));
    p21_45(:,m) = p21aa_45(1:length(p21aa_45(:,m))/2,m);
    p21_45(2:length(p21_45(:,m)),m) =
2*p21_45(2:length(p21_45(:,m)),m);
    p21_45(:,m) = abs(p21_45(:,m));

    p21aa_60(:,m) = fft(ch21_60(:,m))/length(ch21_60(:,m));
    p21_60(:,m) = p21aa_60(1:length(p21aa_60(:,m))/2,m);
    p21_60(2:length(p21_60(:,m)),m) =
2*p21_60(2:length(p21_60(:,m)),m);
    p21_60(:,m) = abs(p21_60(:,m));

    p21aa_75(:,m) = fft(ch21_75(:,m))/length(ch21_75(:,m));
```

```
    p21_75(:,m) = p21aa_75(1:length(p21aa_75(:,m))/2,m);
    p21_75(2:length(p21_75(:,m)),m) =
2*p21_75(2:length(p21_75(:,m)),m);
    p21_75(:,m) = abs(p21_75(:,m));

    p21aa_90(:,m) = fft(ch21_90(:,m))/length(ch21_90(:,m));
    p21_90(:,m) = p21aa_90(1:length(p21aa_90(:,m))/2,m);
    p21_90(2:length(p21_90(:,m)),m) =
2*p21_90(2:length(p21_90(:,m)),m);
    p21_90(:,m) = abs(p21_90(:,m));

    p21aa_105(:,m) = fft(ch21_105(:,m))/length(ch21_105(:,m));
    p21_105(:,m) = p21aa_105(1:length(p21aa_105(:,m))/2,m);
    p21_105(2:length(p21_105(:,m)),m) =
2*p21_105(2:length(p21_105(:,m)),m);
    p21_105(:,m) = abs(p21_105(:,m));

    p21aa_120(:,m) = fft(ch21_120(:,m))/length(ch21_120(:,m));
    p21_120(:,m) = p21aa_120(1:length(p21aa_120(:,m))/2,m);
    p21_120(2:length(p21_120(:,m)),m) =
2*p21_120(2:length(p21_120(:,m)),m);
    p21_120(:,m) = abs(p21_120(:,m));

    p21aa_135(:,m) = fft(ch21_135(:,m))/length(ch21_135(:,m));
    p21_135(:,m) = p21aa_135(1:length(p21aa_135(:,m))/2,m);
    p21_135(2:length(p21_135(:,m)),m) =
2*p21_135(2:length(p21_135(:,m)),m);
    p21_135(:,m) = abs(p21_135(:,m));

    p21aa_150(:,m) = fft(ch21_150(:,m))/length(ch21_150(:,m));
    p21_150(:,m) = p21aa_150(1:length(p21aa_150(:,m))/2,m);
    p21_150(2:length(p21_150(:,m)),m) =
2*p21_150(2:length(p21_150(:,m)),m);
    p21_150(:,m) = abs(p21_150(:,m));

    p21aa_165(:,m) = fft(ch21_165(:,m))/length(ch21_165(:,m));
    p21_165(:,m) = p21aa_165(1:length(p21aa_165(:,m))/2,m);
    p21_165(2:length(p21_165(:,m)),m) =
2*p21_165(2:length(p21_165(:,m)),m);
    p21_165(:,m) = abs(p21_165(:,m));

    p21aa_180(:,m) = fft(ch21_180(:,m))/length(ch21_180(:,m));
    p21_180(:,m) = p21aa_180(1:length(p21aa_180(:,m))/2,m);
    p21_180(2:length(p21_180(:,m)),m) =
2*p21_180(2:length(p21_180(:,m)),m);
    p21_180(:,m) = abs(p21_180(:,m));

% Channel 22 FFT (every 15 degrees) ===================
    p22aa_0(:,m) = fft(ch22_0(:,m))/length(ch22_0(:,m));
    p22_0(:,m) = p22aa_0(1:length(p22aa_0(:,m))/2,m);
    p22_0(2:length(p22_0(:,m)),m) = 2*p22_0(2:length(p22_0(:,m)),m);
    p22_0(:,m) = abs(p22_0(:,m));

    p22aa_15(:,m) = fft(ch22_15(:,m))/length(ch22_15(:,m));
    p22_15(:,m) = p22aa_15(1:length(p22aa_15(:,m))/2,m);
    p22_15(2:length(p22_15(:,m)),m) =
2*p22_15(2:length(p22_15(:,m)),m);
```

```
    p22_15(:,m) = abs(p22_15(:,m));

    p22aa_30(:,m) = fft(ch22_30(:,m))/length(ch22_30(:,m));
    p22_30(:,m) = p22aa_30(1:length(p22aa_30(:,m))/2,m);
    p22_30(2:length(p22_30(:,m)),m) =
2*p22_30(2:length(p22_30(:,m)),m);
    p22_30(:,m) = abs(p22_30(:,m));

    p22aa_45(:,m) = fft(ch22_45(:,m))/length(ch22_45(:,m));
    p22_45(:,m) = p22aa_45(1:length(p22aa_45(:,m))/2,m);
    p22_45(2:length(p22_45(:,m)),m) =
2*p22_45(2:length(p22_45(:,m)),m);
    p22_45(:,m) = abs(p22_45(:,m));

    p22aa_60(:,m) = fft(ch22_60(:,m))/length(ch22_60(:,m));
    p22_60(:,m) = p22aa_60(1:length(p22aa_60(:,m))/2,m);
    p22_60(2:length(p22_60(:,m)),m) =
2*p22_60(2:length(p22_60(:,m)),m);
    p22_60(:,m) = abs(p22_60(:,m));

    p22aa_75(:,m) = fft(ch22_75(:,m))/length(ch22_75(:,m));
    p22_75(:,m) = p22aa_75(1:length(p22aa_75(:,m))/2,m);
    p22_75(2:length(p22_75(:,m)),m) =
2*p22_75(2:length(p22_75(:,m)),m);
    p22_75(:,m) = abs(p22_75(:,m));

    p22aa_90(:,m) = fft(ch22_90(:,m))/length(ch22_90(:,m));
    p22_90(:,m) = p22aa_90(1:length(p22aa_90(:,m))/2,m);
    p22_90(2:length(p22_90(:,m)),m) =
2*p22_90(2:length(p22_90(:,m)),m);
    p22_90(:,m) = abs(p22_90(:,m));

    p22aa_105(:,m) = fft(ch22_105(:,m))/length(ch22_105(:,m));
    p22_105(:,m) = p22aa_105(1:length(p22aa_105(:,m))/2,m);
    p22_105(2:length(p22_105(:,m)),m) =
2*p22_105(2:length(p22_105(:,m)),m);
    p22_105(:,m) = abs(p22_105(:,m));

    p22aa_120(:,m) = fft(ch22_120(:,m))/length(ch22_120(:,m));
    p22_120(:,m) = p22aa_120(1:length(p22aa_120(:,m))/2,m);
    p22_120(2:length(p22_120(:,m)),m) =
2*p22_120(2:length(p22_120(:,m)),m);
    p22_120(:,m) = abs(p22_120(:,m));

    p22aa_135(:,m) = fft(ch22_135(:,m))/length(ch22_135(:,m));
    p22_135(:,m) = p22aa_135(1:length(p22aa_135(:,m))/2,m);
    p22_135(2:length(p22_135(:,m)),m) =
2*p22_135(2:length(p22_135(:,m)),m);
    p22_135(:,m) = abs(p22_135(:,m));

    p22aa_150(:,m) = fft(ch22_150(:,m))/length(ch22_150(:,m));
    p22_150(:,m) = p22aa_150(1:length(p22aa_150(:,m))/2,m);
    p22_150(2:length(p22_150(:,m)),m) =
2*p22_150(2:length(p22_150(:,m)),m);
    p22_150(:,m) = abs(p22_150(:,m));

    p22aa_165(:,m) = fft(ch22_165(:,m))/length(ch22_165(:,m));
```

```
    p22_165(:,m) = p22aa_165(1:length(p22aa_165(:,m))/2,m);
    p22_165(2:length(p22_165(:,m)),m) =
2*p22_165(2:length(p22_165(:,m)),m);
    p22_165(:,m) = abs(p22_165(:,m));

    p22aa_180(:,m) = fft(ch22_180(:,m))/length(ch22_180(:,m));
    p22_180(:,m) = p22aa_180(1:length(p22aa_180(:,m))/2,m);
    p22_180(2:length(p22_180(:,m)),m) =
2*p22_180(2:length(p22_180(:,m)),m);
    p22_180(:,m) = abs(p22_180(:,m));

% Channel 23 FFT (every 15 degrees) ===================
    p23aa_0(:,m) = fft(ch23_0(:,m))/length(ch23_0(:,m));
    p23_0(:,m) = p23aa_0(1:length(p23aa_0(:,m))/2,m);
    p23_0(2:length(p23_0(:,m)),m) = 2*p23_0(2:length(p23_0(:,m)),m);
    p23_0(:,m) = abs(p23_0(:,m));

    p23aa_15(:,m) = fft(ch23_15(:,m))/length(ch23_15(:,m));
    p23_15(:,m) = p23aa_15(1:length(p23aa_15(:,m))/2,m);
    p23_15(2:length(p23_15(:,m)),m) =
2*p23_15(2:length(p23_15(:,m)),m);
    p23_15(:,m) = abs(p23_15(:,m));

    p23aa_30(:,m) = fft(ch23_30(:,m))/length(ch23_30(:,m));
    p23_30(:,m) = p23aa_30(1:length(p23aa_30(:,m))/2,m);
    p23_30(2:length(p23_30(:,m)),m) =
2*p23_30(2:length(p23_30(:,m)),m);
    p23_30(:,m) = abs(p23_30(:,m));

    p23aa_45(:,m) = fft(ch23_45(:,m))/length(ch23_45(:,m));
    p23_45(:,m) = p23aa_45(1:length(p23aa_45(:,m))/2,m);
    p23_45(2:length(p23_45(:,m)),m) =
2*p23_45(2:length(p23_45(:,m)),m);
    p23_45(:,m) = abs(p23_45(:,m));

    p23aa_60(:,m) = fft(ch23_60(:,m))/length(ch23_60(:,m));
    p23_60(:,m) = p23aa_60(1:length(p23aa_60(:,m))/2,m);
    p23_60(2:length(p23_60(:,m)),m) =
2*p23_60(2:length(p23_60(:,m)),m);
    p23_60(:,m) = abs(p23_60(:,m));

    p23aa_75(:,m) = fft(ch23_75(:,m))/length(ch23_75(:,m));
    p23_75(:,m) = p23aa_75(1:length(p23aa_75(:,m))/2,m);
    p23_75(2:length(p23_75(:,m)),m) =
2*p23_75(2:length(p23_75(:,m)),m);
    p23_75(:,m) = abs(p23_75(:,m));

    p23aa_90(:,m) = fft(ch23_90(:,m))/length(ch23_90(:,m));
    p23_90(:,m) = p23aa_90(1:length(p23aa_90(:,m))/2,m);
    p23_90(2:length(p23_90(:,m)),m) =
2*p23_90(2:length(p23_90(:,m)),m);
    p23_90(:,m) = abs(p23_90(:,m));

    p23aa_105(:,m) = fft(ch23_105(:,m))/length(ch23_105(:,m));
    p23_105(:,m) = p23aa_105(1:length(p23aa_105(:,m))/2,m);
    p23_105(2:length(p23_105(:,m)),m) =
2*p23_105(2:length(p23_105(:,m)),m);
```

```
    p23_105(:,m) = abs(p23_105(:,m));

    p23aa_120(:,m) = fft(ch23_120(:,m))/length(ch23_120(:,m));
    p23_120(:,m) = p23aa_120(1:length(p23aa_120(:,m))/2,m);
    p23_120(2:length(p23_120(:,m)),m) =
2*p23_120(2:length(p23_120(:,m)),m);
    p23_120(:,m) = abs(p23_120(:,m));

    p23aa_135(:,m) = fft(ch23_135(:,m))/length(ch23_135(:,m));
    p23_135(:,m) = p23aa_135(1:length(p23aa_135(:,m))/2,m);
    p23_135(2:length(p23_135(:,m)),m) =
2*p23_135(2:length(p23_135(:,m)),m);
    p23_135(:,m) = abs(p23_135(:,m));

    p23aa_150(:,m) = fft(ch23_150(:,m))/length(ch23_150(:,m));
    p23_150(:,m) = p23aa_150(1:length(p23aa_150(:,m))/2,m);
    p23_150(2:length(p23_150(:,m)),m) =
2*p23_150(2:length(p23_150(:,m)),m);
    p23_150(:,m) = abs(p23_150(:,m));

    p23aa_165(:,m) = fft(ch23_165(:,m))/length(ch23_165(:,m));
    p23_165(:,m) = p23aa_165(1:length(p23aa_165(:,m))/2,m);
    p23_165(2:length(p23_165(:,m)),m) =
2*p23_165(2:length(p23_165(:,m)),m);
    p23_165(:,m) = abs(p23_165(:,m));

    p23aa_180(:,m) = fft(ch23_180(:,m))/length(ch23_180(:,m));
    p23_180(:,m) = p23aa_180(1:length(p23aa_180(:,m))/2,m);
    p23_180(2:length(p23_180(:,m)),m) =
2*p23_180(2:length(p23_180(:,m)),m);
    p23_180(:,m) = abs(p23_180(:,m));

end


% Channel 20 Average and Calibration (every 15 degrees)
===================
p20_0 = sum(p20_0')';
p20_0 = p20_0/m;
p20_0 = p20_0(1:length(f));
p20_0 = p20_0./CC20;

p20_15 = sum(p20_15')';
p20_15 = p20_15/m;
p20_15 = p20_15(1:length(f));
p20_15 = p20_15./CC20;

p20_30 = sum(p20_30')';
p20_30 = p20_30/m;
p20_30 = p20_30(1:length(f));
p20_30 = p20_30./CC20;

p20_45 = sum(p20_45')';
p20_45 = p20_45/m;
p20_45 = p20_45(1:length(f));
p20_45 = p20_45./CC20;
```

```
p20_60 = sum(p20_60')';
p20_60 = p20_60/m;
p20_60 = p20_60(1:length(f));
p20_60 = p20_60./CC20;

p20_75 = sum(p20_75')';
p20_75 = p20_75/m;
p20_75 = p20_75(1:length(f));
p20_75 = p20_75./CC20;

p20_90 = sum(p20_90')';
p20_90 = p20_90/m;
p20_90 = p20_90(1:length(f));
p20_90 = p20_90./CC20;

p20_105 = sum(p20_105')';
p20_105 = p20_105/m;
p20_105 = p20_105(1:length(f));
p20_105 = p20_105./CC20;

p20_120 = sum(p20_120')';
p20_120 = p20_120/m;
p20_120 = p20_120(1:length(f));
p20_120 = p20_120./CC20;

p20_135 = sum(p20_135')';
p20_135 = p20_135/m;
p20_135 = p20_135(1:length(f));
p20_135 = p20_135./CC20;

p20_150 = sum(p20_150')';
p20_150 = p20_150/m;
p20_150 = p20_150(1:length(f));
p20_150 = p20_150./CC20;

p20_165 = sum(p20_165')';
p20_165 = p20_165/m;
p20_165 = p20_165(1:length(f));
p20_165 = p20_165./CC20;

p20_180 = sum(p20_180')';
p20_180 = p20_180/m;
p20_180 = p20_180(1:length(f));
p20_180 = p20_180./CC20;


% Channel 21 Average and Calibration (every 15 degrees)
===================
p21_0 = sum(p21_0')';
p21_0 = p21_0/m;
p21_0 = p21_0(1:length(f));
p21_0 = p21_0./CC20;

p21_15 = sum(p21_15')';
p21_15 = p21_15/m;
p21_15 = p21_15(1:length(f));
p21_15 = p21_15./CC20;
```

```
p21_30 = sum(p21_30')';
p21_30 = p21_30/m;
p21_30 = p21_30(1:length(f));
p21_30 = p21_30./CC20;

p21_45 = sum(p21_45')';
p21_45 = p21_45/m;
p21_45 = p21_45(1:length(f));
p21_45 = p21_45./CC20;

p21_60 = sum(p21_60')';
p21_60 = p21_60/m;
p21_60 = p21_60(1:length(f));
p21_60 = p21_60./CC20;

p21_75 = sum(p21_75')';
p21_75 = p21_75/m;
p21_75 = p21_75(1:length(f));
p21_75 = p21_75./CC20;

p21_90 = sum(p21_90')';
p21_90 = p21_90/m;
p21_90 = p21_90(1:length(f));
p21_90 = p21_90./CC20;

p21_105 = sum(p21_105')';
p21_105 = p21_105/m;
p21_105 = p21_105(1:length(f));
p21_105 = p21_105./CC20;

p21_120 = sum(p21_120')';
p21_120 = p21_120/m;
p21_120 = p21_120(1:length(f));
p21_120 = p21_120./CC20;

p21_135 = sum(p21_135')';
p21_135 = p21_135/m;
p21_135 = p21_135(1:length(f));
p21_135 = p21_135./CC20;

p21_150 = sum(p21_150')';
p21_150 = p21_150/m;
p21_150 = p21_150(1:length(f));
p21_150 = p21_150./CC20;

p21_165 = sum(p21_165')';
p21_165 = p21_165/m;
p21_165 = p21_165(1:length(f));
p21_165 = p21_165./CC20;

p21_180 = sum(p21_180')';
p21_180 = p21_180/m;
p21_180 = p21_180(1:length(f));
p21_180 = p21_180./CC20;

% Channel 22 Average and Calibration (every 15 degrees)
===================
```

```
p22_0 = sum(p22_0')';
p22_0 = p22_0/m;
p22_0 = p22_0(1:length(f));
p22_0 = p22_0./CC20;

p22_15 = sum(p22_15')';
p22_15 = p22_15/m;
p22_15 = p22_15(1:length(f));
p22_15 = p22_15./CC20;

p22_30 = sum(p22_30')';
p22_30 = p22_30/m;
p22_30 = p22_30(1:length(f));
p22_30 = p22_30./CC20;

p22_45 = sum(p22_45')';
p22_45 = p22_45/m;
p22_45 = p22_45(1:length(f));
p22_45 = p22_45./CC20;

p22_60 = sum(p22_60')';
p22_60 = p22_60/m;
p22_60 = p22_60(1:length(f));
p22_60 = p22_60./CC20;

p22_75 = sum(p22_75')';
p22_75 = p22_75/m;
p22_75 = p22_75(1:length(f));
p22_75 = p22_75./CC20;

p22_90 = sum(p22_90')';
p22_90 = p22_90/m;
p22_90 = p22_90(1:length(f));
p22_90 = p22_90./CC20;

p22_105 = sum(p22_105')';
p22_105 = p22_105/m;
p22_105 = p22_105(1:length(f));
p22_105 = p22_105./CC20;

p22_120 = sum(p22_120')';
p22_120 = p22_120/m;
p22_120 = p22_120(1:length(f));
p22_120 = p22_120./CC20;

p22_135 = sum(p22_135')';
p22_135 = p22_135/m;
p22_135 = p22_135(1:length(f));
p22_135 = p22_135./CC20;

p22_150 = sum(p22_150')';
p22_150 = p22_150/m;
p22_150 = p22_150(1:length(f));
p22_150 = p22_150./CC20;

p22_165 = sum(p22_165')';
p22_165 = p22_165/m;
```

```
p22_165 = p22_165(1:length(f));
p22_165 = p22_165./CC20;

p22_180 = sum(p22_180')';
p22_180 = p22_180/m;
p22_180 = p22_180(1:length(f));
p22_180 = p22_180./CC20;

% Channel 23 Average and Calibration (every 15 degrees)
===================
p23_0 = sum(p23_0')';
p23_0 = p23_0/m;
p23_0 = p23_0(1:length(f));
p23_0 = p23_0./CC20;

p23_15 = sum(p23_15')';
p23_15 = p23_15/m;
p23_15 = p23_15(1:length(f));
p23_15 = p23_15./CC20;

p23_30 = sum(p23_30')';
p23_30 = p23_30/m;
p23_30 = p23_30(1:length(f));
p23_30 = p23_30./CC20;

p23_45 = sum(p23_45')';
p23_45 = p23_45/m;
p23_45 = p23_45(1:length(f));
p23_45 = p23_45./CC20;

p23_60 = sum(p23_60')';
p23_60 = p23_60/m;
p23_60 = p23_60(1:length(f));
p23_60 = p23_60./CC20;

p23_75 = sum(p23_75')';
p23_75 = p23_75/m;
p23_75 = p23_75(1:length(f));
p23_75 = p23_75./CC20;

p23_90 = sum(p23_90')';
p23_90 = p23_90/m;
p23_90 = p23_90(1:length(f));
p23_90 = p23_90./CC20;

p23_105 = sum(p23_105')';
p23_105 = p23_105/m;
p23_105 = p23_105(1:length(f));
p23_105 = p23_105./CC20;

p23_120 = sum(p23_120')';
p23_120 = p23_120/m;
p23_120 = p23_120(1:length(f));
p23_120 = p23_120./CC20;

p23_135 = sum(p23_135')';
p23_135 = p23_135/m;
```

```
p23_135 = p23_135(1:length(f));
p23_135 = p23_135./CC20;

p23_150 = sum(p23_150')';
p23_150 = p23_150/m;
p23_150 = p23_150(1:length(f));
p23_150 = p23_150./CC20;

p23_165 = sum(p23_165')';
p23_165 = p23_165/m;
p23_165 = p23_165(1:length(f));
p23_165 = p23_165./CC20;

p23_180 = sum(p23_180')';
p23_180 = p23_180/m;
p23_180 = p23_180(1:length(f));
p23_180 = p23_180./CC20;


%-------------------------------------------------
% Energy Density

% 0 degreees
[ED_0,T_0,U_0] = ED(p20_0,p21_0,p22_0,p23_0,N);


% 15 degreees
[ED_15,T_15,U_15] = ED(p20_15,p21_15,p22_15,p23_15,N);

% 30 degreees
[ED_30,T_30,U_30] = ED(p20_30,p21_30,p22_30,p23_30,N);

% 45 degreees
[ED_45,T_45,U_45] = ED(p20_45,p21_45,p22_45,p23_45,N);

% 60 degreees
[ED_60,T_60,U_60] = ED(p20_60,p21_60,p22_60,p23_60,N);

% 75 degreees
[ED_75,T_75,U_75] = ED(p20_75,p21_75,p22_75,p23_75,N);

% 90 degreees
[ED_90,T_90,U_90] = ED(p20_90,p21_90,p22_90,p23_90,N);

% 105 degreees
[ED_105,T_105,U_105] = ED(p20_105,p21_105,p22_105,p23_105,N);

% 120 degreees
[ED_120,T_120,U_120] = ED(p20_120,p21_120,p22_120,p23_120,N);

% 135 degreees
[ED_135,T_135,U_135] = ED(p20_135,p21_135,p22_135,p23_135,N);

% 150 degreees
[ED_150,T_150,U_150] = ED(p20_150,p21_150,p22_150,p23_150,N);

% 165 degreees
```

```
[ED_165,T_165,U_165] = ED(p20_165,p21_165,p22_165,p23_165,N);

% 180 degreees
[ED_180,T_180,U_180] = ED(p20_180,p21_180,p22_180,p23_180,N);


angle = [0;15;30;45;60;75;90;105;120;135;150;165;180];
freq = f;

EDx(:,1) = ED_0;
EDx(:,2) = ED_15;
EDx(:,3) = ED_30;
EDx(:,4) = ED_45;
EDx(:,5) = ED_60;
EDx(:,6) = ED_75;
EDx(:,7) = ED_90;
EDx(:,8) = ED_105;
EDx(:,9) = ED_120;
EDx(:,10) = ED_135;
EDx(:,11) = ED_150;
EDx(:,12) = ED_165;
EDx(:,13) = ED_180;

% Plotting Routine
figure(1)
clf;
set(gcf,'DefaultAxesFontName','arial');
set(gcf,'DefaultAxesFontSize',12);
set(gcf,'DefaultAxesFontWeight','bold')
set(gcf,'DefaultAxesLineWidth',1.5);
set(gcf,'DefaultAxesGridLineStyle','--');
set(gcf,'DefaultLineLineWidth',2.125);
set(gcf,'DefaultLineMarkerSize',8);

surf(angle,freq,10*log10(EDx/(1.5*10^-15)))
colorbar
shading interp
% title(['l-Rotation ',num2str(t*N),' Averages'],'FontSize',15)
zlabel('Total Energy Density','FontSize',16)
ylabel('Frequency (Hz)','FontSize',16)
xlabel('\theta (degrees)','FontSize',16)
```